System Design of the MeerKAT L - band 3D Radar for Monitoring Near Earth Objects

Doreen Agaba

Ph.D Thesis

Supervisor: Prof. M. R. Inggs
Department of Electrical Engineering

UNIVERSITY OF CAPE TOWN

3rd October 2017

"A radio telescope is half a radar (receive-only), on a stable ground-based platform, observing stationary targets"

Declaration

I declare that the work on which this thesis is based is my original work (except where acknowledgements indicate otherwise).

It is being submitted for the degree of Doctor of Philosophy in Engineering in the University of Cape Town. It has not been submitted before for any degree or examination in any other university.

I authorise the University to reproduce for the purpose of research either the whole or any portion of the contents in any manner whatsoever.

Author:

Doreen Agaba
Signature:

.....
Cape Town

3rd October 2017

Abstract

This thesis investigates the current knowledge of small space debris (diameter less than 10 cm) and potentially hazardous asteroids (PHA) by the use of radar systems. It clearly identifies the challenges involved in detecting and tracking of small space debris and PHAs. The most significant challenges include: difficulty in tracking small space debris due to orbital instability and reduced radar cross-section (RCS), errors in some existing data sets, the lack of dedicated or contributing instruments in the Southern Hemisphere, and the large cost involved in building a high performance radar for this purpose.

This thesis investigates the cooperative use of the KAT-7 (7 antennas) and MeerKAT (64 antennas) radio telescope receivers in a radar system to improve monitoring of small debris and PHAs was investigated using theory and simulations, as a cost effective solution. Parameters for a low cost and high performance radar were chosen, based on the receiver digital back-end. Data from such radars will be used to add to existing catalogues thereby creating a constantly updated database of near Earth objects and bridging the data gap that is currently being filled by mathematical models.

Based on literature and system requirements, quasi-monostatic, bistatic, multistatic, single input multiple output (SIMO) radar configurations were proposed for radio telescope arrays in detecting, tracking and imaging small space debris in the low Earth orbit (LEO) and PHAs. The maximum dwell time possible for the radar geometry was found to be 30 seconds, with coherent integration limitations of 2 ms and 121 ms for accelerating and non-accelerating targets, respectively.

The multistatic and SIMO radar configurations showed sufficient detection (SNR $\geq$13 dB) for small debris and quasi-monostatic configuration for PHAs. Radar detection, tracking and imaging (ISAR) simulations were compared to theory and ambiguities in range and Doppler were compensated for.

The main contribution made by this work is a system design for a high performance, cost effective 3D radar that uses the KAT-7 and MeerKAT radio telescope receivers in a commensal manner. Comparing theory and simulations, the SNR improvement, dwell time increase, tracking and imaging capabilities, for small debris and PHAs compared to existing assets, was illustrated. Since the MeerKAT radio telescope is a precursor for the SKA Africa, extrapolating the capabilities of the MeerKAT radar to the SKA radar implies that it would be the most sensitive and high performing contributor to space situational awareness, upon its completion.

From this feasibility study, the MeerKAT 3D distributed radar will be able to detect debris of diameter less than 10 cm at altitudes between 700 km to 900 km, and PHAs, with a range resolution of 15 m, a minimum SNR of 14 dB for 152 pulses for a coherent integration time of 2.02 ms. The target range (derived from the two way delay), velocity (from Doppler frequency) and direction will be measured within an accuracy of: 2.116 m, 15.519 m/s, 0.083^o(single antenna), respectively. The range, velocity accuracies and SNR affect orbit prediction accuracy by 0.021 minutes for orbit period and 0.0057^o for orbit inclination. The multistatic radar was found to be the most suitable and computationally efficient configuration compared to the bistatic and SIMO configurations, and beamforming should be implemented as required by specific target geometry.

Dedication

This work is dedicated to God who made it possible for me to start the journey that brought me from Uganda to the University of Cape Town in South Africa, to pursue my postgraduate studies (Honours, Masters and Ph.D) until completion. To God be the Glory and Praise. Amen

Acknowledgements

My gratitude goes to the following people and organisations:

My family members (my mother: Ms Kamusiime Justine, husband: Atuhaire Philip, brother: Ahumuza Dornam, sister: Akisiimire Hindrah, daughters: Lilly and Abigail) for the support and encouragement they gave me to pursue postgraduate studies in a country that is far from home. It's your faith in me that kept me going for all these years.

The Square Kilometre Array postgraduate bursary program and the University of Cape Town postgraduate funding for providing funds for fees, equipment, upkeep and travelling for an international conference. The funding offered made it possible for my studies to go on until completion.

Professor Michael R. Inggs, my supervisor who offered expert guidance and council in the radar field which was new to me. Without your patience, encouragement and persistent nudging, it would have been an extremely difficult journey. Your support went beyond academic needs and am truly grateful for the nurturing you gave me.

A/Professor Amit Kumar Mishra, A/Professor Daniel O'Hagan, Dr. Simon Winberg, Dr. Yunus Gaffar and Mr. Lerato Mohapi, thank you for your continued guidance in my academic work.

All the members of the Radar Remote Sensing Group, staff of the department of Electrical Engineering and of Student Housing and Residence Life at the University of Cape Town, thank you for your support and company during the

course of my study.

My friends in Cape Town, who held my hand through the ups and downs of this journey: Ms. Naluminsa Elizabeth, Mrs. Wegoye Florence, Dr. Wegoye Emmanuel and Mrs. Nicole Kalala, to mention but a few. Thank you for being our family away from home.

The various authors of all the material and algorithms that I made use of during the course of my research.

Contents

List of Figures

List of Tables

Nomenclature

SSA	Space Situational Awareness
NEOs	Near-Earth Objects
LEO	Low Earth Orbit
PHAs	Potentially Hazardous Asteroids
NEAs	Near Earth Asteroids
TLE	Two Line Elements
ECEF	Earth Centred Earth Fixed
ENU	East North Up
LNA	Low Noise Amplifier
ADC	Analog to Digital Converter
PFB	Polyphase Filter Bank
BPF	Band Pass Filter
LPF	Low Pass Filter
DBE	Digital Back End
LO	Local Oscillator
CPI	Coherent Processing Interval
CIT	Coherent Integration Time
PRF	Pulse Repetition Frequency
FFT	Fast Fourier Transform
DFT	Discrete Fourier Transform
RCS	Radar Cross Section
PSF	Point Spread Function
MIMO	Multiple In put Multiple Out put
SIMO	Single In put Multiple Out put

Chapter 1: Introduction

1.1 Space Situational Awareness

The Space Situational Awareness (SSA) programme was initiated in 2008 by the European Union [2] and the German armed forces [3], in an effort to support utilisation and access to space by use of accurate data on the space environment, particularly regarding potential damage to infrastructure in orbit and on the ground [2]. According to the space foundation in Washington, SSA is the ability to understand and predict the physical location of natural and manmade objects orbiting around the Earth, with the objective of avoiding collisions [4].

Generally, space hazards are from collisions between objects in orbit, harmful space weather and Earth impacts by asteroids [5]. Investing in the SSA programme has become critical because space-based systems are increasingly becoming indispensable to many developed economies and government functions, particularly in terms of security. Any shutdown or loss of services from these systems would affect an large range of commercial and civil activities such as: commercial land, air and sea travel, maritime navigation, telecommunications, information technology and networks, broadcasting, climate monitoring and weather forecasting.

Therefore, through detection and orbit estimation, SSA aims to predict and assess the risk to life and property due to space debris objects, re-entries, in-orbit explosions, in-orbit collisions and potential impacts of Near Earth Objects (NEOs). Through SSA, information regarding effects of space weather

phenomena on space and ground based infrastructure is obtained. This information is used to plan and execute evasive manoeuvres and de-orbiting of satellites [6]. Preventive measures can only be performed effectively with an accurate and constantly updated catalogue/data base.

In the past few decades, ground and space based radars have been viewed as potential sources of data on space objects, in addition to optical and laser instruments [5, 7]. In addition to the well known advantages of radars over optical and/or laser applications (able to operate at night and in difficult environmental conditions, cloud penetration, high detection probabilities at very large ranges, the use of Doppler frequency [8]), radar has the potential to tackle some of the challenges experienced by optical and laser methods in SSA [9]. Not only is radar data an important addition to the space objects catalogue, but it is also used to improve orbital element accuracy, orbit prediction and determination [6].

Most of the terrestrial radars that provide data on space debris, asteroids, operational and non-operational space craft, use radio telescopes receivers [9, 10, 11]. This is because most radio telescopes have large apertures (high gain) and low noise temperature, giving them the potential to be sensitive radar receivers. It is this idea that has captured the attention to which this research is focused.

This research investigates the possibility of utilising the Square Kilometre Array (SKA) Africa radio telescope precursor, as a receiver in a high power radar for detection of space debris in the Low Earth Orbit (LEO) and Potentially Hazardous Asteroids (PHAs). Even though the idea to use radar for SSA is not new, the capability of such a large instrument as a radar receiver has not been investigated. Such a radar would be capable of overcoming the challenges of: limited bandwidth and position estimates that are not accurate enough to reliably predict probabilities for collisions with space debris, low resolution for small space debris and multi-object tracking.

The ability of a radar to effectively detect and track an object depends on the waveform transmitted, the transmitter, target and receiver properties [12, 13]. In view of this, radar configurations and signal processing techniques are looked at to find out which would be most suitable for detection, tracking and imaging of

NEOs. We find that a radar which uses the MeerKAT radio telescope receivers (from here on referred to as the MeerKAT 3D radar due to its capability for vertical electronic beam steering) would need to use multiple waveforms, multiple pulse repetition frequencies (PRFs) and once the data is available, different signal processing techniques (Details in chapter 3).

One of the unique aspects of this work is the contribution the MeerKAT 3D radar would have to the existing space catalogues by using an instrument in the Southern hemisphere, an area that is in great need for data on space objects as shown in Figure 1.1 [14]. In addition, the MeerKAT radio telescope, upon completion will be the largest and most sensitive radio telescope in the Southern hemisphere. A complete hemispherical radar surveillance system is a prerequisite for SSA so as to cover all observation angles and minimise/eliminate "blind zones".

1.2 Risk assessment of small space debris

By using models, the European Space Agency (ESA) has estimated the number of debris objects orbiting around Earth to be 29,000 for sizes larger than 10 cm, 670,000 larger than 1 cm and more than 170 million larger than 1 mm [2, 1]. The NASA Orbital Debris Programme has developed the Orbital Debris Model ORDEM2010, Satellite Breakup Risk Assessment Model (SBRAM) and Long Term Evolution Model (EVOLVE), for evaluating debris flux, short term collision risk and long term environmental effect for the purpose of risk assessment and space craft design [16].

Currently, the SSN has capabilities for detecting objects of diameter between 5 and 10 cm in the LEO, using radar and optical sensors. Only objects with diameter $\geq$ 10 cm can be reliably tracked by terrestrial sensors. Objects which can be tracked and whose origin is known are catalogued, and the number of objects cataloged by SSN as of 2016 was over 21,000 [17]. In addition to the United States SSN, the space object catalogue of the Russian Federation and ESA, DISCOS (Database and Information System Characterising Objects

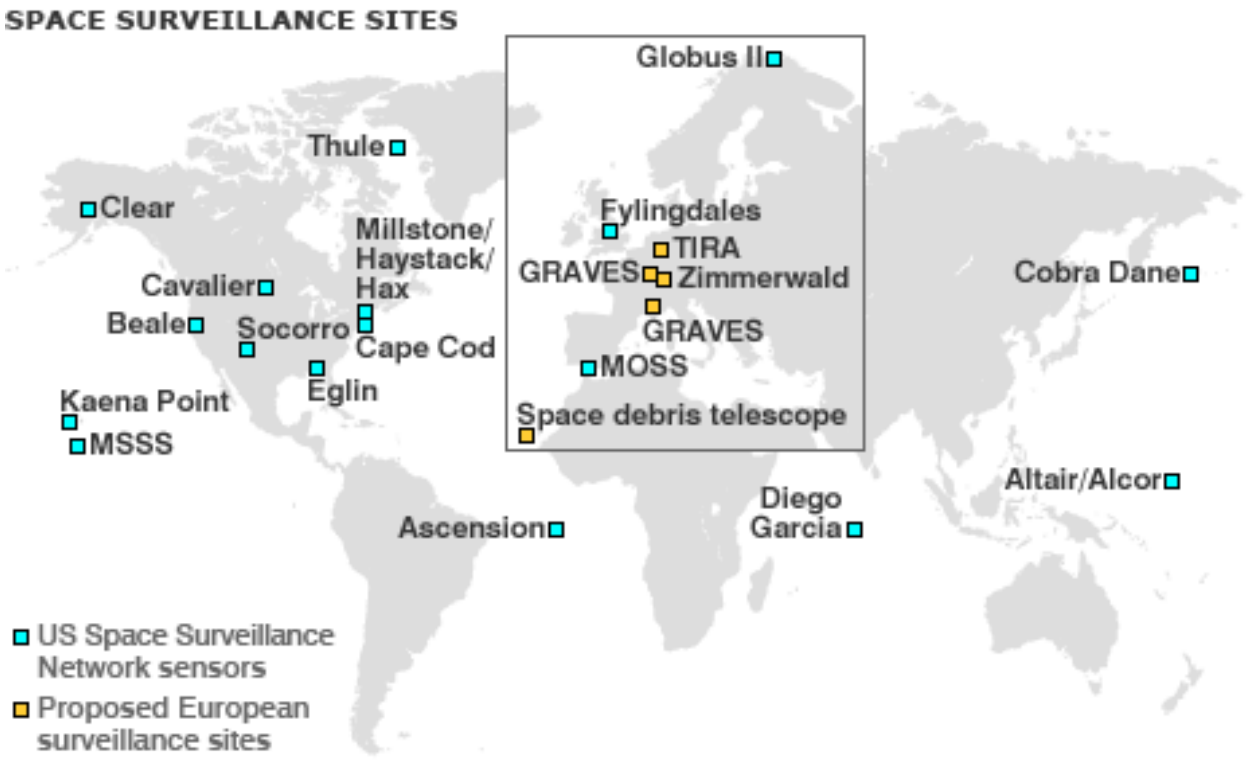

Figure 1.1: Space Surveillance Network (SSN), a world wide distribution of optical and radar dedicated, collateral and auxiliary sensors for monitoring space objects [15]. This illustrates the need for more sensors in the Southern Hemisphere.

in Space) is constantly updating their catalogues [18]. The National Space Development Agency (NASDA) of Japan is also studying a trajectory prediction analysis for re-entering objects and collision avoidance analysis for new launches [19].

Objects of size $\leq$ 10 cm are not constantly tracked and data available is fragmented and with large uncertainties, so space debris short and long term mathematical models are used [20]. Due to in-orbit collisions and explosions, it is feared that the density of small debris will eventually rise above a critical value, causing a run-away chain reaction, known as the Kessler syndrome [21].

For many missions, the risk of destruction through the impact of space debris is considered to be the third highest risk, after launch and deployment risks.

In order to avoid the consequences of space debris, we need to know where the debris objects are, which means developing surveillance technologies.

Therefore, an understanding of the debris environment of size $\leq$ 10 cm is necessary and paramount. This work focusses on radar detection and tracking of debris of diameter $\leq$ 10 cm . From this point, we refer to orbital debris of diameter $\leq$ 10 cm as small space debris. As illustrated in Figure 1.2, space debris models estimate a large flux of objects with diameter $\leq$ 10 m near the International Space Station (ISS) in the LEO.

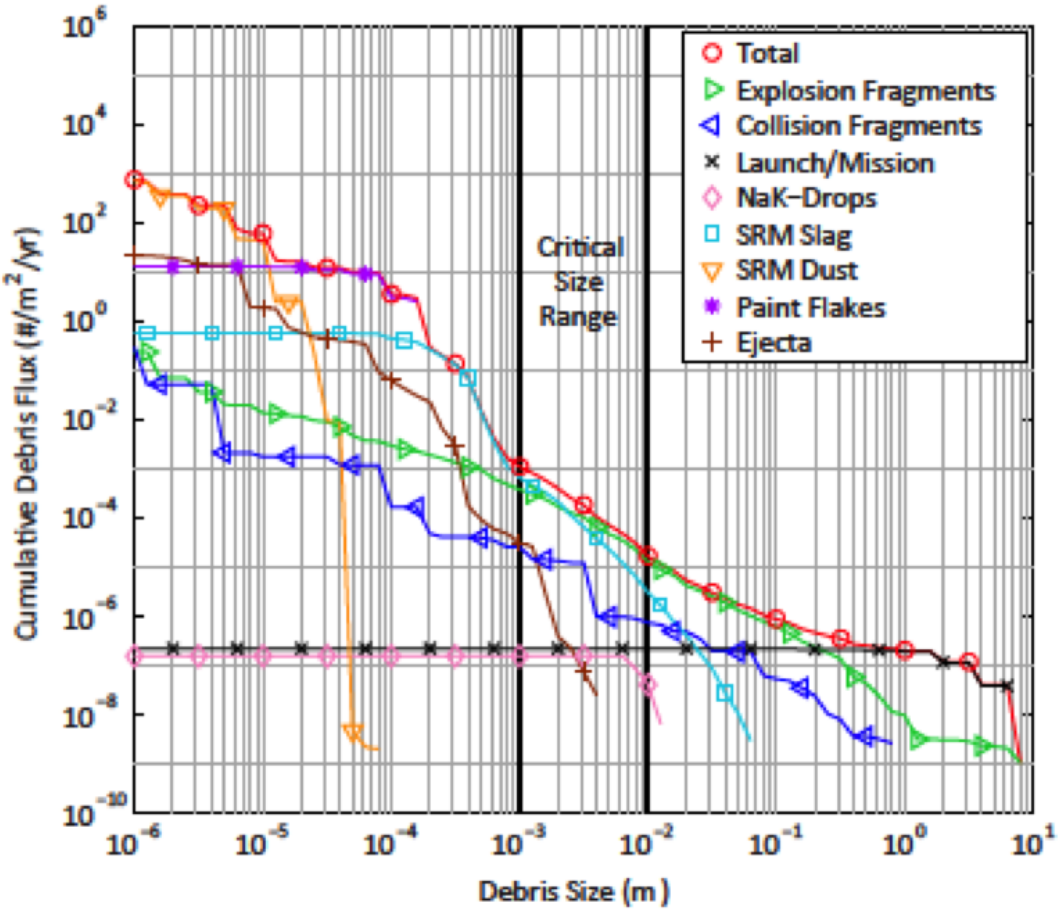

Figure 1.2: Estimated debris flux showing the critical size of 1 cm, 10 cm in the ISS orbit [22] as predicted by the MASTER-2009 orbital debris model was used [23].

Space debris of diameter ≤ 3 mm have been successfully shielded against, and space debris of size ≥ 10 cm are relatively well understood and tracked, enabling collision avoidance manoeuvres to be employed. Table 1.1 shows the recorded ISS collision avoidance manoeuvres performed in 2011-2012, and cases where the crew retreated to Soyuz due to insufficient time for manoeuvre [24].

Even though it may seem that objects of size ≤ 10 cm are "small", the speed at which they travel makes them a potential hazard to space operations. Risk assessment of these objects includes looking at probability of collision with operational spacecraft, as well as its subsequent consequences particularly in terms of cost. The principal risk factors are the spatial density and average relative collisional velocity along the orbit (altitude and inclination) of the space object.

Table 1.1: The ISS pre-determined avoidance manoeuvres (PDAM) and close approaches in 2011-2012 [24]. As of July 2015, the ISS had performed 25 PDAMs.

Date	**Object Avoided**	**Action Taken**
2-April-2011	Debris from Russian Cosmos 2251	Manoeuvre
28-June-2011	Debris from Proton ullage motor	Crew retreated to Soyuz
29-September-2011	Russian Tsyklon rocket body	Manoeuvre
13-January-2012	Debris from Iridium 33	Manoeuvre
28-January-2012	Debris from Fengyun-1C	Manoeuvre
24-March-2012	Debris from Russian Cosmos 2251	Crew retreated to Soyuz

The severity of the space debris situation in the future years depends on the scale of future space activities, degree to which debris generation is controlled and the effectiveness of debris mitigation measures. Figure 1.3 gives an estimated guide to penetration depth as a function of impactor size and speed. The vertical co-ordinate is an aluminium equivalent thickness in millimetres. This work focusses on understanding the small debris environment so as to better implement mitigation mechanisms.

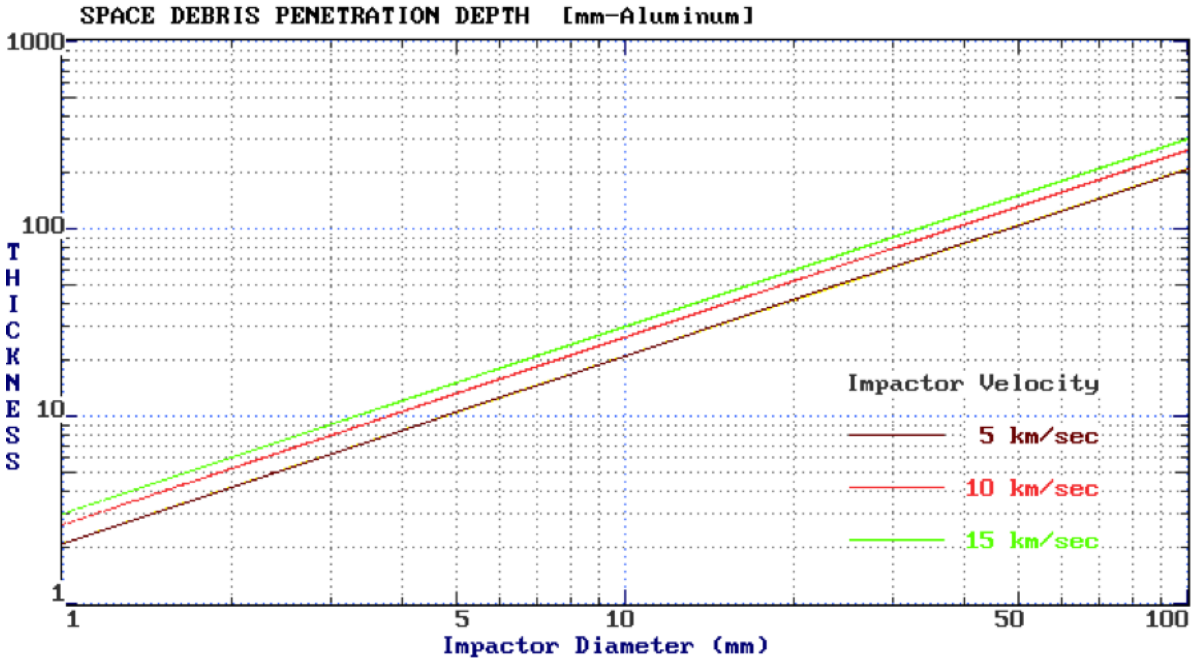

Figure 1.3: NASA's simulated penetration depth as a function of impactor size and speed on an aluminium equivalent thickness in millimetres [25]. Debris velocities of 5, 10 and 15 km/s are considered.

1.3 Potentially hazardous asteroids (PHAs)

Near Earth asteroids (NEAs) orbit within 0.3 Astronomical Units (AU) of the Earth's orbit. A NEA is said to be potentially hazardous when it orbits within 0.05 AU (7.5e6 km) of the Earth's orbit, and this distance is known as the Earth Minimum Orbit Intersection Distance (MOID). The MOID estimated absolute magnitude of 22 mag, corresponds to a diameter of 140 m. By 2015, the largest known PHA was 2015 HY116 with 17.5 mag and diameter $\approx$ 2.13 km [26].

A number of Earth based and space based radio astronomy telescopes and radar systems have done observations of PHAs. Currently, NASA approximates the number of NEAs to 15,000 and 1717 classified as PHAs, of which 157 have an absolute magnitude equal or greater than 17 which corresponds to a diameter of atleast 1 km [27]. PHAs are large enough to cause significant regional damage in the event of an Earth impact. Land and ocean impact of PHAs could lead

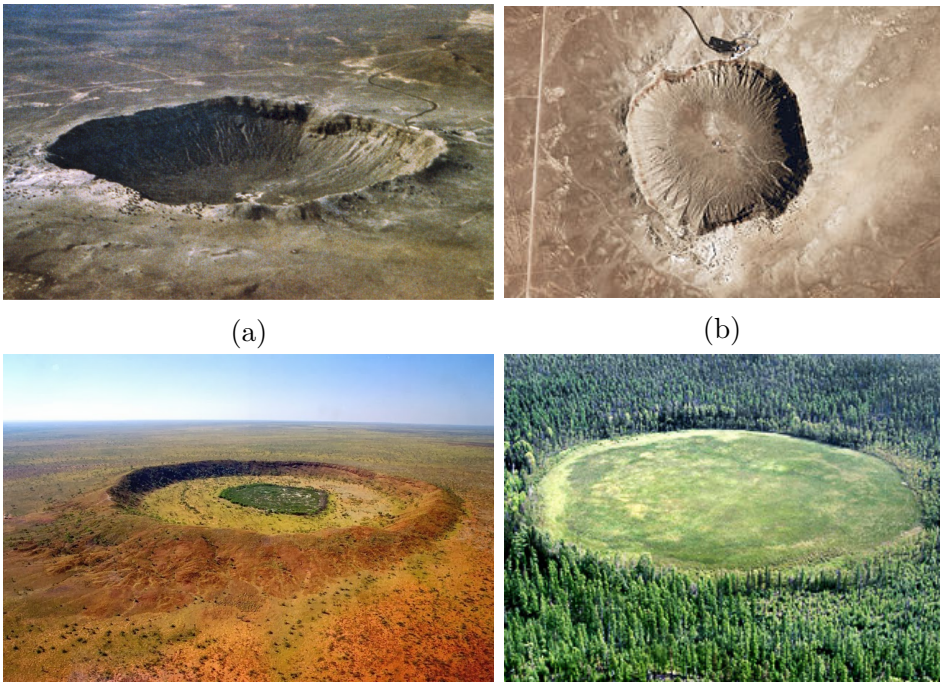

(a) (b)

(c) (d)

Figure 1.4: Some examples of Earth impacts by asteroids; Winslow Arizona [30] (a), Flagstaff, Arizona(b), Wolfe Creek Crater, Australia(c), Tunguska, Siberia(d) [31]

to regional devastation to human settlements or tsunamis, respectively [28]. Figure 1.4 shows some craters that were created by asteroids and Figure 1.5 shows the locations of impact craters on the world map [29].

1.4 Problem statement

Although space studies have been done for nearly the past century, a large portion of space objects is unknown to man. And since these objects travel at very high speeds (about 8 km/s for space debris and 11 km/s for asteroids), they have the potential to collide and penetrate operational spacecraft causing damage and degradation [25]. Performing collision avoidance manoeuvres adds the cost of fuel which may not have been budgeted for at the launch and this reduces

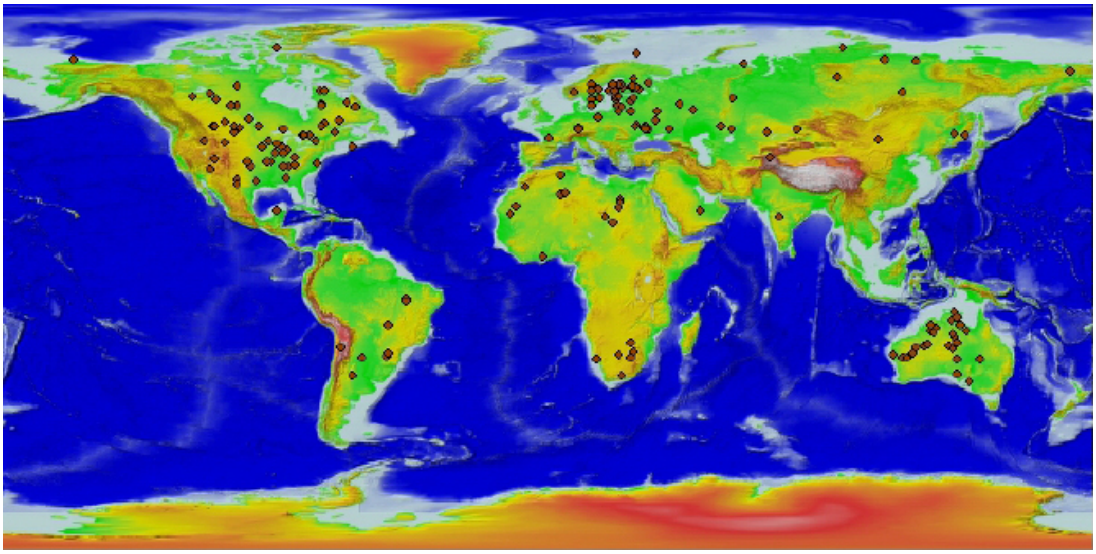

Figure 1.5: The world map showing 174 Earth impact craters as of 2016, image obtained from the Planetary Science Institute in [29].

mission life. In other instances, the use of a laser beam to generate a force on the hazardous object in an effort to change its trajectory (space ablation) has been proposed [32]. Other debris mitigation measures include; de-orbiting and robotic removal.

In order to implement mitigation techniques, a reliable, accurate and constantly updated catalogue of NEOs is a fundamental requirement. This is presently a challenge for the large number of small debris in the LEO since there are not many instruments dedicated to SSA. Further more, available instruments experience challenges of inaccurate orbit determination due to orbital instability and small RCS of small debris, low resolution and inability to track small objects.

Therefore, there is need for high resolution instruments to probe the small debris environment further. Radar has shown great capabilities in monitoring of space objects. To avoid the cost of a large radar, we propose the cooperative use of the MeerKAT radio telescope receiver. In future, combining the use of large radio telescope arrays across continents would create a very sensitive and powerful radar network that maps the "sky", providing data at all elevation and azimuth angles and to large altitudes. A constantly updated database, will

enable sustainable use of the space environment, while preventing damage and threats to both humans and space technology.

1.4.1 Hypothesis

It is possible to design a cost effective, high performance radar system using the MeerKAT radio telescope receiver to simultaneously detect, track and image multiple pieces of space objects. Data obtained from the radar can be used to determine object parameters such as size, velocity, altitude and orientation, which are used for classification.

1.4.2 Research Questions

The following research questions were looked at during this research:

Research question 1: *What would be the most cost effective and suitable transmitter for the MeerKAT 3D radar?*

Considering that there is no transmitter in the Southern hemisphere in the site of the available radio telescope receivers with a common view of the space objects, an overview of available commercial high power and cost effective transmitters was done. A region for the proposed location for the transmitter within the receiver line of sight was chosen while considering the radio frequency interference (RFI) levels for the SKA site as defined by the International Telecommunication Union (ITU).

Due to the site suitability and existing infrastructure, we proposed the installation of a high power amplifier on a 10 m parabolic antenna at the Denel Overberg test range in Bredasdorp, near Cape Town, South Africa. The transmit power levels considered were 10 kW, 2 MW.

Research question 2: *What is the detection and tracking sensitivity of the MeerKAT 3D radar?*

It is important to know the maximum and minimum RCS relative to range that the MeerKAT 3D radar can detect and with what accuracy. Once radar data has been obtained and used for orbital prediction, the two line elements (TLE) data obtained will have errors that propagate from the radar measurements (range, velocity and angle) and tracking filter used.

The predicted orbital elements should have inclination, longitude of ascending node, and orbital period errors that are within an acceptable value, lest the predicted orbit deviates significantly from the true orbit. In view of this, I performed a system detection and tracking sensitivity analysis, and then compared the MeerKAT 3D performance with some published detection and tracking results.

Research question 3: *What is the nearest to optimal radar configuration and signal processing technique suitable for the data obtained from the MeerKAT 3D radar?*

This question was answered by comparing the signal processing and computational requirements for the bistatic, multistatic and SIMO radar configurations and assessing which geometry requires minimal or no changes to the already existing MeerKAT radio telescope receiver hardware. After coherent and non-coherent signal processing, A comparison of all the geometries' performance in terms of increasing SNR, minimising tracking errors and implementing multibeam sensing to increase dwell time and track time, was done.

1.4.3 Objective of study

The main objective of this research was the system design of a radar that uses theKAT-7 and MeerKAT radio telescope receivers. This was achieved by investigating the most efficient and cost effective (in a sense that the

receiver is already built for Astronomical purposes) but high performance radar configuration and signal processing for monitoring small space debris and potentially hazardous asteroid.

Through simulations and theoretical analysis, the bistatic, multistatic and SIMO radar configurations were evaluated in order to determine the optimal mode of operation. Parameters investigated include: SNR, detection probability, false alarm rate, transmit power, transmit waveform, range/Doppler resolution and track time. Such a radar system, once implemented will provide data that can be used to classify NEOs and in the long run become a vital contributor to a constantly updated database.

1.5 Thesis contributions

The following are some of the main contributions from this work:

1. A radar system design that uses 64 interlinked antenna receivers in the multistatic and SIMO radar configurations (chapter 4). At the moment, there is no terrestrial space surveillance radar with comparable capabilities to what we expect from the MeerKAT L-band 3D radar in terms of sensitivity, accuracy and multiple beam coverage.

2. The MeerKAT 3D radar will provide data that will be a valuable contribution to the existing fragmented and largely statistical small space debris catalogs (details in Chapter 1). Once operational, such a high performance radar can be adjusted to include capabilities beyond the near Earth orbit (NEO), such as assisting in Mars expeditions.

3. The successful use of the MeerKAT radar will be a pathfinder for other large radio telescope arrays to consider cooperative use of their receivers for SSA, with minimal hard ware additions.

4. Small space debris and PHAs coverage in the Southern hemisphere, particularly in Africa is almost non-existent as of 2017. In the past,

proposed space object observations using a transmitter or receiver in the Southern Hemisphere were unsuccessful because of this. One such example is the proposed Arecibo-HartRAO (Hartebeesthoek Radio Astronomy Observatory) observation of the PHA 2011 UW158 that made a close pass to Earth in June 2015 that could not be done due to lack of coverage.

5. Once implemented, the proposed transmitter will be one of the first transmitters in Africa, and one of the few transmitters in the Southern hemisphere, dedicated to SSA.

1.6 Methodology and Thesis layout

This thesis starts with an overview of what small space debris and PHAs are and why we are interested in detecting and tracking, and eventually cataloging them. The hypothesis and research questions were clearly stated. In this section, a summary of the stages through which this radar system design and analysis was done, is given. A more detailed explanation for each implementation stage is given in chapter 3, where a "proof of concept" study was done based on theory and simulations. Below is a summary of the stages of implementation of this research:

- A background study was done on small space debris and PHAs indicating the threat they pose to space craft and humans in the event of an impact, the extra costs necessary to perform collision avoidance manoeuvres, and the need for reliable data on NEOs.
- Then a brief review was performed on the available technology to design a high power cost effective transmitter located far enough from the radio telescope not to cause interference, but within the radar's coverage.
- The radar receiver specifications were formalised based on the MeerKAT radio telescope receivers and I propose the points in the MeerKAT digital back end at which radar data cab be collected, giving their computational requirements.

- A description of the multistatic and SIMO radar signal processing methods showing how they can be implemented on the data to maximise performance was given.
- In order to see how the radar performs ideally, a theoretical analysis of the detection, tracking and imaging capabilities in terms of RCS, SNR, dwell time and track time, and calculate range, Doppler and angular measurement errors, was performed.
- Based on the transmitter and receiver specifications, radar simulations of the MeerKAT radar were done to obtain ideal data and process it using the bistatic, multistatic and SIMO configurations. Since space debris data is not readily available, the comparison of theory and simulations was considered as an acceptable means for validation.

1.7 Outline of Chapters

The thesis implementation stages described in the brief methodology and thesis layout, results, discussions and conclusion were put in chapters, as described in this section.

1.7.1 Chapter 2

This Chapter gives a summary of the results from terrestrial radars that are either dedicated or contributing to SSA in terms of detection and tracking of small space debris and PHAs. The most commonly used SSA assets are TIRA and EISCAT in Germany, GRAVES in France, HAX and Haystack in USA, Northern Cross and Medicina in Italy. Some of the results obtained from the SSA assets were found to have errors when compared to cataloged objects and Mathematical models. The limitations within the available SSA assets and the gaps that need to be filled are briefly stated. Figure 1.6 shows an example of debris measurements done in the USA by the Haystack radar.

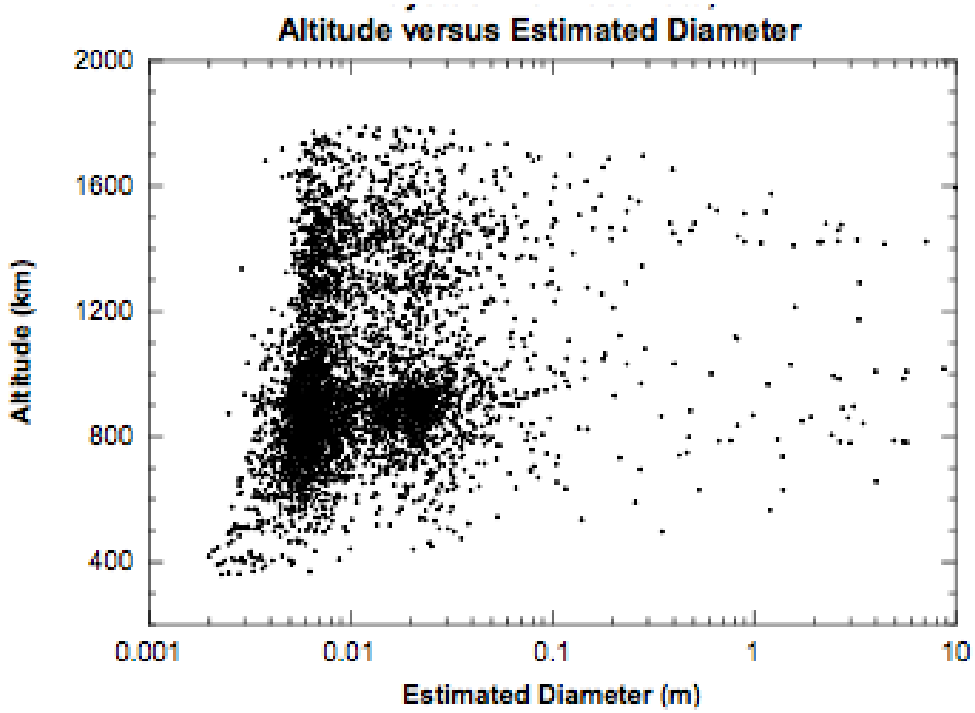

Figure 1.6: Debris result from data obtained using the Haystack radar at 75^o East in 2006.

An overview of commercially available transmitter types, their performance relative to cost and size is summarised. The high-Power Oscillator Transmitter (POT), which is a keyed-oscillator magnetron tube suitable for non-coherent or pseudo-coherent radars, and the high-Power Amplier Transmitter (PAT), which constitutes a waveform generator and an amplifier (Magnetron, Klystron, Gyrotron, Twystron, Traveling Wave Tube (TWT), Solid-State or Crossfeld Amplifier (CFA)), are compared. Table 1.2 shows a summary of the transmitter types considered.

Then a description of the MeerKAT radio telescope receiver in terms of location, antenna size and distribution are given. The receiver digital back end is described giving the steps taken through reception and the computational requirements for each step. The MeerKAT correlator which performs Fourier transform 'F' followed by Cross-correlation 'X' was described. The MeerKAT's data storage and sharing protocol, Streaming Protocol for Exchanging Astronomical Data

Table 1.2: Skolnik's comparison of High-Power Pulsed Amplifiers for the same frequency and peak and average power output [8]. * Clustered-cavity klystron can achieve 10 to 15% bandwidth at higher cost, ** In 1 MHz bandwidth

	Klystron	TWT	Conventional	High gain
Voltage	High (90 kV for 1 MW)	High	Low (40 kV for 1 MW)	Low
Gain	30-70 dB	30-70 dB	8-15 dB	15-30 dB
Bandwidth	1-8%*	10-15%	10-15%	10-15%
Efficiency	15-30%	15-30%	35-45%	35-45%
Weight/size	High/Large	High/large	Low/small	Low/small
Tube cost	Medium	High	Medium	Medium
Noise**	-90 dB	-90 dB	-55 dB	-70 dB
Usable dynamic range	40-80 dB	40-80 dB	afew dBs	afew dBs

(SPEAD), was given.

Finally, an overview of the MIMO radar technique is briefly explained, clearly stating the MIMO radar subsets (SIMO, SISO, S-MIMO, TR-MIMO, TB-MIMO, T-MIMO), their pros and cons, applications and suitability to the MeerKAT radar data. The advantages of the SIMO radar over MIMO radar in terms computational efficiency, overcoming the MIMO limitations, and suitability to radio telescope receivers were given.

1.7.2 Chapter 3

The transmitter location and specifications are given, along with an analysis of the RFI power as compared to the MeerKAT threshold levels. The bistatic radar configuration that uses one MeerKAT receiver, is used for proof of concept for the minimum capability of the MeerKAT 3D radar in monitoring small space debris and PHAs. The bistatic radar parameters are given, justifying each choice. The process of obtaining target TLE, deriving orbital elements that were used to calculate the ECEF and then ENU Cartesian coordinates, is explained. The debris and asteroid parameters are given.

A geometry analysis is performed where the transmitter and receiver beam intersection area is calculated from which the maximum possible dwell time is derived. Non-coherent SNR is calculated for maximum dwell times, for the

chosen targets. Using the coherent integration time limitations for accelerating and non-accelerating targets, coherently integrated bistatic SNR is calculated and compared to the non-coherent case. A threshold of single pulse SNR=13 dB is chosen for P_D of 88% and P_{fa} of 1e-6. All the coherent and most of the non-coherent SNR values fall below this threshold. This led to the proposal of using a high power gallium-nitride (GaN) high electron mobility transistors (HEMT) transmitter of 2 MW to improve detections seen in the improved SNR.

Due to the large range, the bistatic geometry approximates quasi-monostatic for PHAs, and large pulse lengths are required. Using the high power transmitter and phase codes (Barker codes) of length 13, coherent quasi-monostatic SNR was obtained for PHAs.

Range shifting and Keystone transform methods for range migration and Doppler ambiguity compensation are summarised and applied to fast-time slow-time data. When applied to a single target, range shifting was able to remove range migration and some of the results are shown in Figure 1.7. The Keystone transform was able to remove range migration and Doppler spreading for debris, but not for PHAs. The number of range bins traversed in PHA fast-time slow-time data decreased when the range bin size was increased, but even for the smallest, most suitable range bin size, range migration was not completely removed.

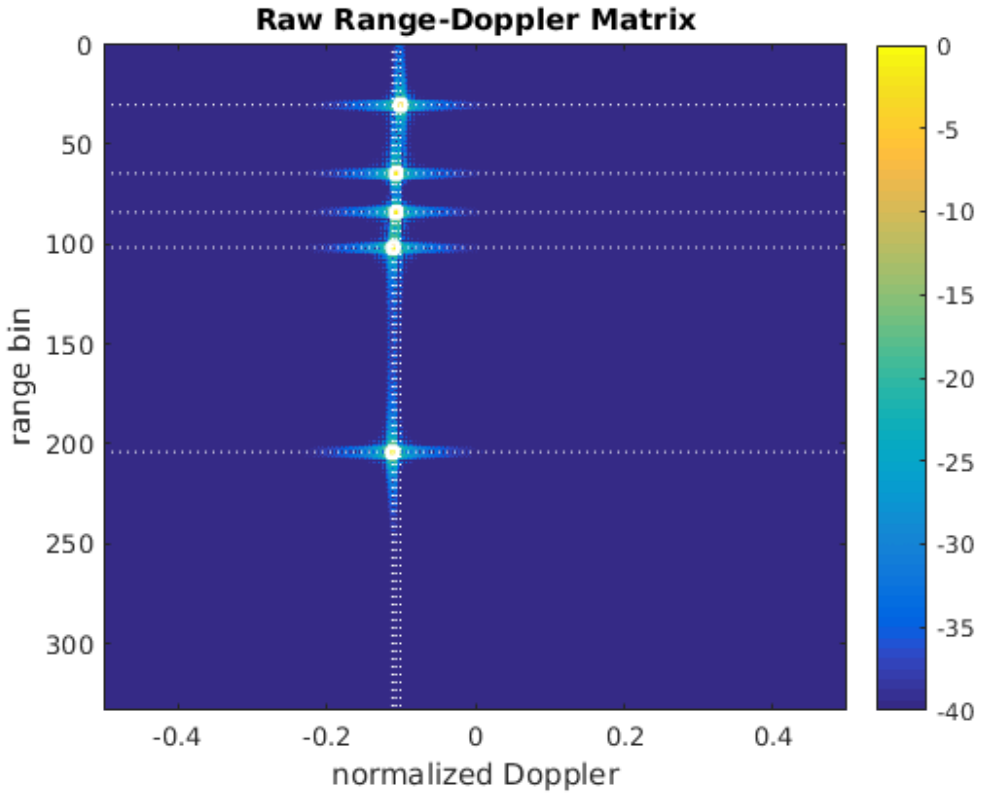

Figure 1.7: Debris: Fengyun-1C, Iridium 33, Cosmos 2251, Delta 1, and DMSP-F11 at wrapped normalised Doppler frequencies of: -0.11080 -0.10720 -0.10120 -0.11200 -0.10720 cycles/sample, respectively. The number of range bins migrated were: 2.6511, 2.6619, 2.6798, 2.6476, 2.6619, respectively and zero after the Keystone compensation.

Using the radar simulator FERS and the proposed bistatic radar parameters chosen, simulated data was obtained and processed to give amplitude-range-Doppler plots (Figure 1.8) for the chosen debris and PHAs. The results show bistatic delay and Doppler frequency to 0.1% and 0.9% of expected theoretical values, respectively. It is important to note that these errors/deviations are after 4 significant figures. The theoretical and simulated values are similar up to 4 significant figures. Since theory is supposed to match simulations, the source of these deviations was investigated and found to be as a result of the rounding off and calculations made in the post-processing.

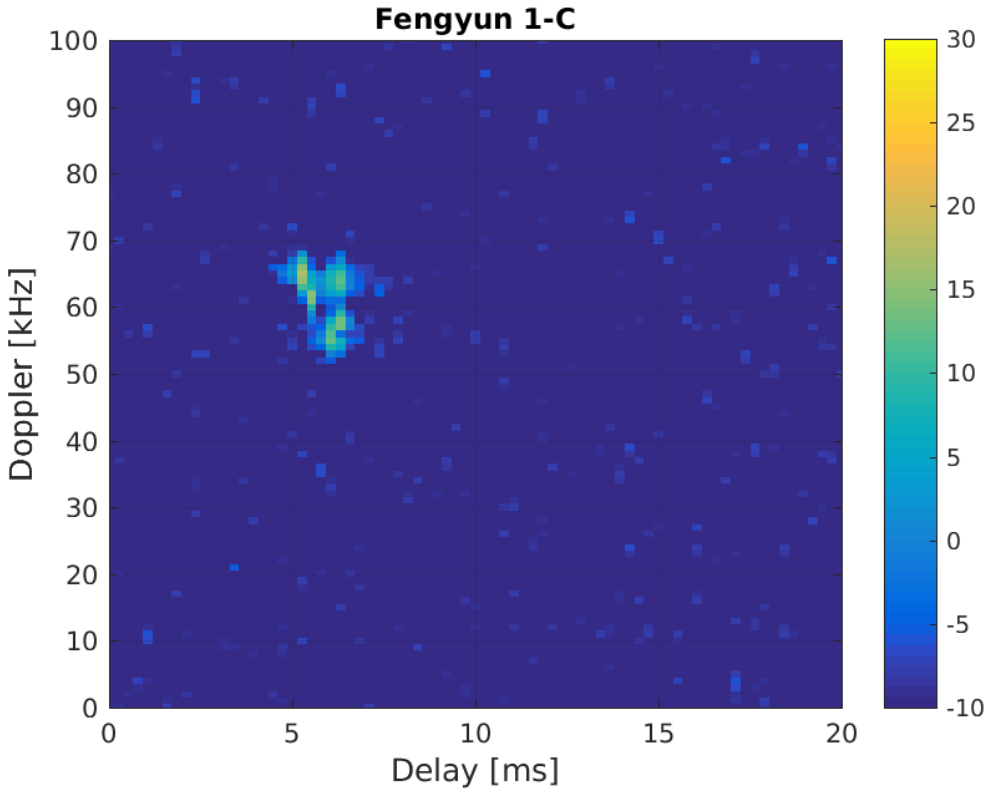

Figure 1.8: Simulated delay-Doppler map for all debris objects for the Meer—KAT radar bistatic geometry after coherent processing.

It was found that the maximum coherent SNR for the MeerKAT bistatic radar was higher than the non-coherent integration by 7 dB for the maximum number of pulses for the two geometries considered. Therefore, in simulations, only coherent integration is considered and the simulation duration is limited to the CIT limitation (2.02 ms) for non-accelerating targets. Using range shifting, range migration was compensated for in the FERS simulation of the Fengyun1-C debris. From geometry, accelerating targets have the largest CIT leading to better Doppler resolution compared to non-accelerating targets.

For asteroids, the quasi-monostatic set up, using phase codes, is not sufficient to detect objects with a positive SNR. More receivers need to be used in order to obtain meaningful NEA detections. The range walk is worse for asteroids due to their high speed, and both the range shifting and Keystone transform were

unable to completely remove the range migration. One of the solutions to this problem is severely under-sampling the asteroid data so as to increase the range bin size significantly.

1.7.3 Chapter 4

In chapter 4, the multistatic radar equation and geometry are discussed. Assuming that all the antennas are pointing in the maximum azimuth and elevation direction, the maximum dwell time for each receiver is calculated as shown in Figure 1.9. Coherent SNR is calculated and compared to the bistatic coherent SNR case, for accelerating debris and PHAs. It is seen that increasing the number of receivers to 64 improves detection significantly, as expected. The amplitude-range-Doppler plots using simulated multistatic radar data are obtained.

The SIMO radar signal model and signal processing is given, dividing the MeerKAT receiver into three concentric circular sub-arrays. The SIMO coherent SNR for debris and asteroid targets is calculated and compared to the multistatic coherent SNR. In order to improve detection further, beamforming is done for the sub-arrays for obtaining "pencil" beams. The beamformed beams are then simulated and ARD plots obtained for both debris and PHAs. Using the radar simulator, the "pencil" beams are placed close together to increase the CIT and perform multi-beam target tracking. Comparing a theoretical and simulated linear debris track showed the degree of accuracy of the tracking model increasing from the outer to the middle and then the inner array.

Debris imaging is simulated using inverse synthetic radar (ISAR) and LFM waveforms and making use of the high down range and cross range resolution that can be attained from stretch processing and DFT. By defining ISAR geometry for debris and adding rotation motion that was not considered before, an imaging algorithm is implemented using Octave. The small debris are modelled as a larger debris cluster/cloud of diameter 1 m with 5 evenly distributed 10 cm targets, from the origin. The ISAR CLEAN deconvolution algorithm is implemented to

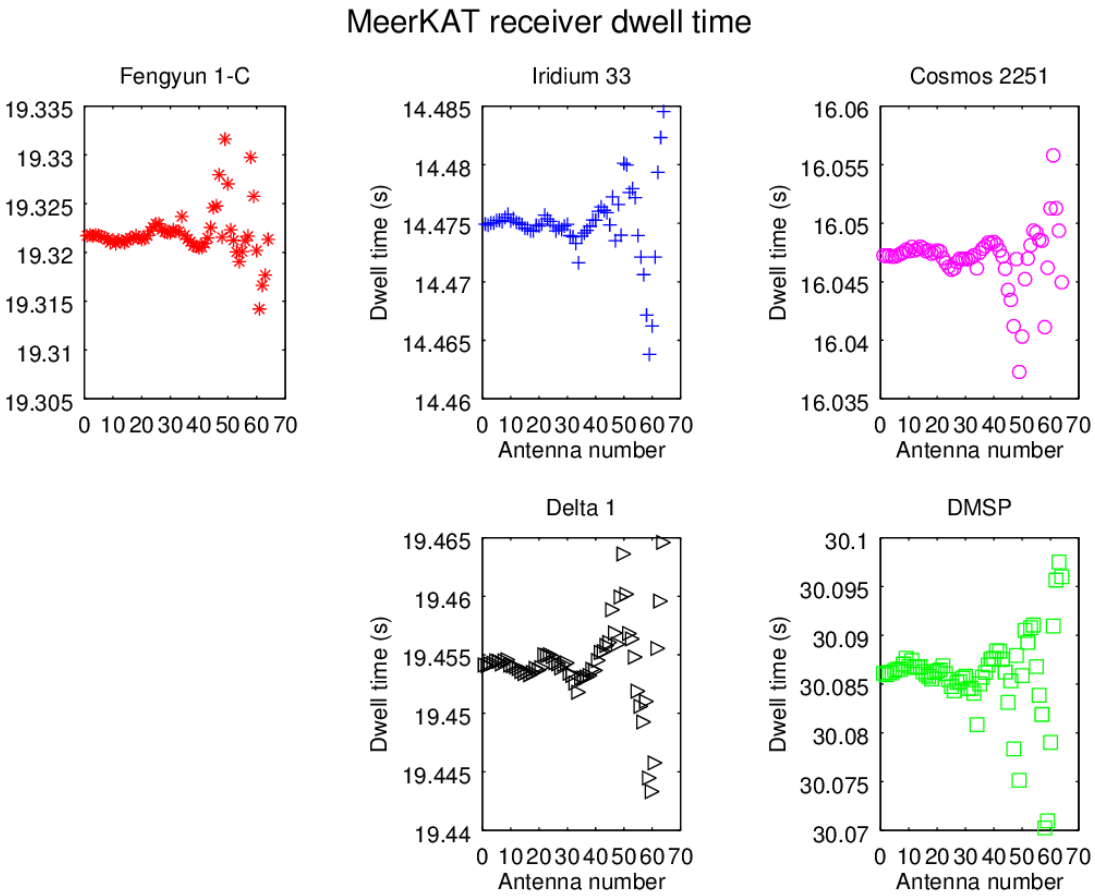

Figure 1.9: Geometric multistatic dwell time for each of the 5 representative orbital debris from 1 transmitter to the 64 MeerKAT receivers. Dwell time varies with target altitude, transmitter/receiver antenna azimuth and elevation.

improve the image resolution Radar measurement accuracies in range, velocity, and tracking errors were calculated and compared to what is currently acceptable in some SSA radio telescope assets (Table 1.3).

Table 1.3: Table of MeerKAT 3D radar, Haystack, Haystack Auxiliary (HAX) and FPS-85 radar measurement errors.

Radar	σ_R (m)	σ_v (m/s)	σ_A (Deg)	σ_T (Min)	σ_i (Deg)
MeerKAT	0.0075	10.55	0.028	0.021	0.0057
Haystack	0.0100	0.65	0.001	0.12	0.021
HAX	0.005	0.41	0.002	0.11	0.020
FPS-85	11.00		0.036	0.05	0.001

1.7.4 Chapter 5

This is the discussion of the results from the bistatic, multistatic and SIMO radar configurations, with sub-arrays. A conclusion is made on the capability that the MeerKAT 3D radar would have in monitoring space debris and PHAs in terms of minimum RCS, required SNR and acceptable measurement errors. A summary of the computational requirements for the bistatic, multistatic and SIMO radar configurations is given. Anticipated challenges that such a radar, once physically implemented would experience are summarised. Proposed future work to the research done in this work is given, including a possible experiment once the transmitter has been installed.

Chapter 2: Literature Review

This chapter gives a summary of a selection of results from terrestrial radars that are either dedicated or contributing to SSA in terms of detection and tracking of small space debris and PHAs. Only results from radars that use radio Astronomy assets are considered to be of interest to this work. Section 2.1 gives a description of terrestrial radar measurements of NEOs, indicating the radar requirements, challenges and selected results from sensors that have contributed largely to SSA in the past decade. An overview of commercially available transmitter types, their performance relative to cost and size is summarised. Parameters such as duty cycle and peak power, cost and availability were evaluated and compared for selected companies.

In section 2.3, then a description of the MeerKAT radio telescope receiver, its location and specifications of the antennas that it constitutes are given. A description of the data flow from the L-band receiver to the digitiser, correlator, beamformer up to storage, including the data types supported and storage space required. The overall hardware and computational requirements for the MeerKAT antennas to be used as a radar receiver are given.

Finally in , the MIMO radar approach is briefly explained, briefly looking at the history of the technique and clearly stating the MIMO radar subsets (SIMO, T-MIMO, TR-MIMO). The advantages and disadvantages of the MIMO approach compared to the conventional radar in terms of detection, tracking and accuracy are discussed. Then the suitability of the MIMO signal processing to the MeerKAT digital back end is looked at.

2.1 Terrestrial radar measurements of NEOs

The radar sensitivity and the range at which it can accurately detect space objects, depend on the sensor parameters, power budget and operating wavelength. Radar can detect/track only objects in its field of view if it has a mechanically controlled beam using parabolic reflectors, or can detect multiple targets simultaneously if it has an electronically controlled beam using phased array antennas.

NEO observations require high power and high sensitivity radars since the observation for a single debris piece is generally limited to less than 1 second, and due to the small radar cross section(RCS) for space debris and large range for asteroids, the returning radar signals have low signal to noise ratio (SNR).

The three main modes commonly used in radar measurements of NEOs are: tracking mode, beam-park (stare) mode and mixed mode (stare and chase), which is a combination of the beam-park and tracking mode. Some of the radar configurations that have been used for space debris detection include monostatic, bistatic, multistatic and phased array. With a certain degree of uncertainty, space debris measurements that can be derived from radar measurements include: orbital elements, altitude, size and shape of the object, orbital lifetime, ballistic coefficient (the rate at which the orbital semi-major axis decays), object mass, material properties [33].

At the moment, ground based radar measurements of small space debris in the LEO are mainly done by the USA using Haystack, Haystack Auxiliary (HAX) Arecibo and Goldstone radars (upto 0.2 cm size), and the Tracking and Imaging Radar (TIRA) in Effelsberg Germany. Another instrument is Japan's bistatic radar system of the Institute of Space and Astronautical Sciences (ISAS) which has the capability to detect objects as small as 2 cm at an altitude of 500 km [19].

The majority of NEA radar measurements have been done by the Arecibo S-band (2380 MHz, 12.5 cm) radar, the Goldstone X-band (8560 MHz, 3.5 cm) radar, and the Green Bank Telescope (GBT). Some of the Arecibo delay-Doppler asteroid

observations produced images with range resolutions as fine as 7.5 m. One such example is the PHA 2011 UW158, that was observed on 13-16 July 2015 as seen in Figure 2.1. From the images of 2011 UW158, it was possible to observe the asteroid surface features [34].

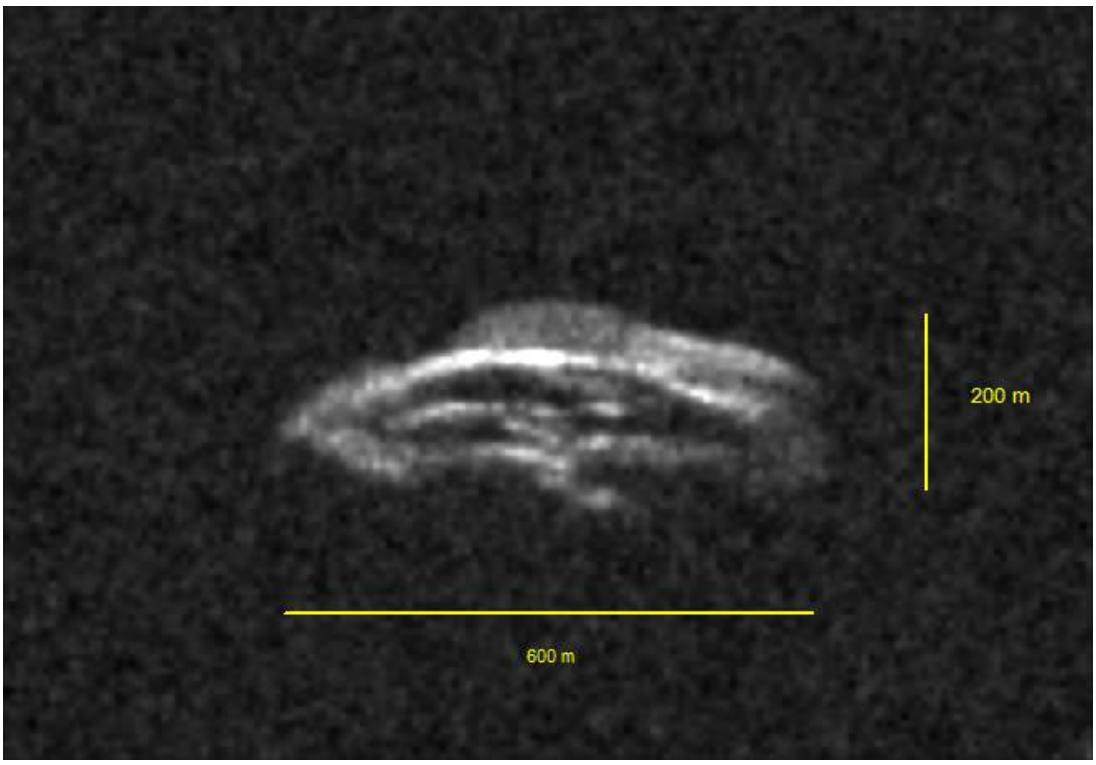

Figure 2.1: Delay-Doppler image of asteroid UW158 obtained from observations by the Arecibo S-band radar, the Goldstone X-band radar, and Green Bank Telescope, in July 2015 when it made a close pass to Earth at a distance of ≈ 2.4 million km [34].

2.1.1 Haystack and HAX radars

Haystack, which provides the majority of small debris data, consists of a 36.6 m parabolic main reflector and its operating efficiency at 10 GHz (3 cm wavelength) is 35 % corresponding to a gain of 67.23 dB with a 0.058 degree half-power beamwidth. The HAX radar is a scaled down version of the Haystack radar. It consists of a 12.2 m parabolic main reflector, and has an operating efficiency

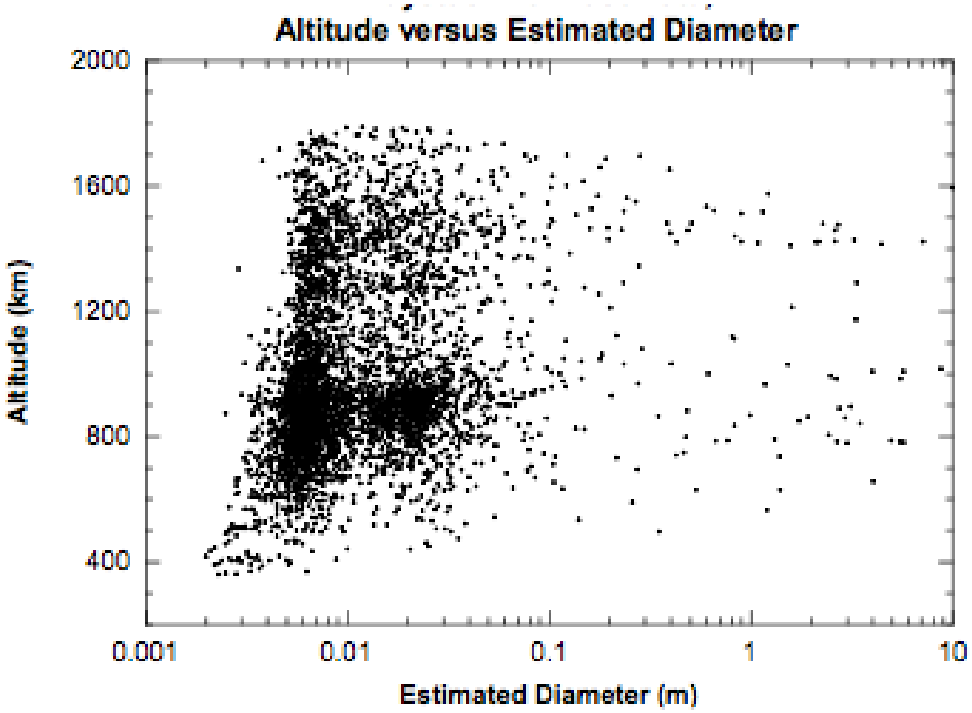

Figure 2.2: Haystack 75^o East debris result for 2006 data

at 16.7 GHz (1.8 cm wavelength) of 51 %, corresponding to a gain of 63.64 dB with a half-power beamwidth of 0.10 degrees [33, 35]. In the beam park mode, the Haystack and HAX radars use monopulse angle channels to determine the position of each pulse in the radar beam, from which orbital elements are deduced with moderate accuracy. Comparing results with SSN catalogued objects that pass through the HAX and Haystack field of view uncovered some errors in the FY2003 Haystack (Figure 2.2) and HAX (Figure 2.3) data. There was a large number of false alarms and this reduced the capability of the Haystack and HAX radars to detect debris smaller than 1 cm and 4 cm, respectively, for all data recorded in FY2003. Some of the data showed a +1.5 dB to +2.0 dB bias in the measured RCS as a result of the monopulse data from sidelobes which produces a very low estimate of the detected objects diameter. Proposed sources of errors include: radar calibration that leads to the beam shape correction procedure, uneven noise floor produced by the bandpass filter and cross-talk [33].

It is important to note that different space debris catalogues (including the NASA

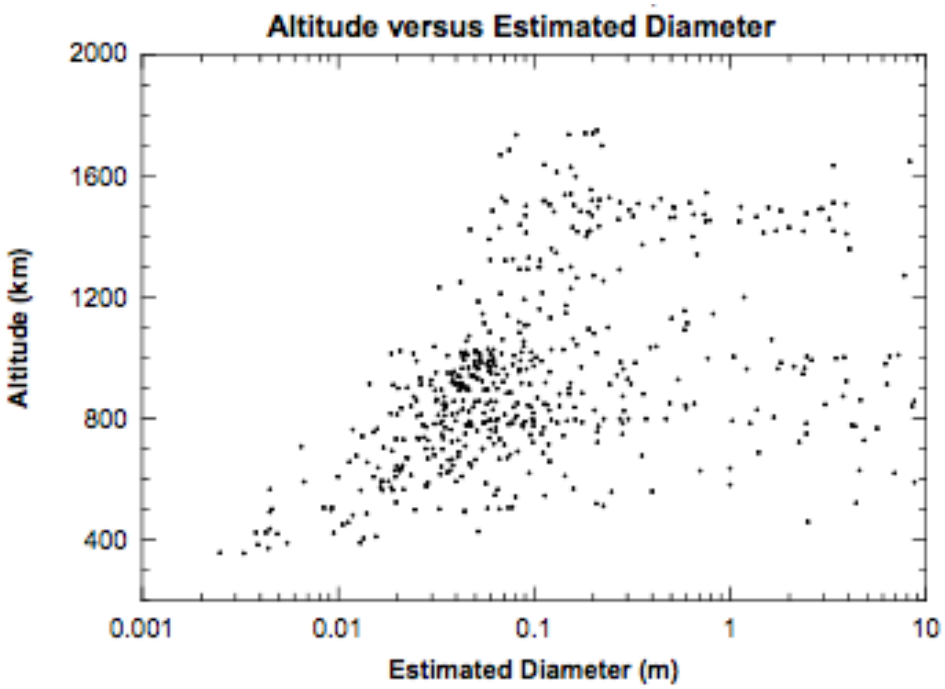

Figure 2.3: HAX 75^o East debris result for 2006 data

Space Science Data Coordinated Archive (NSSDCA), the United States Space Surveillance Network (USSN), North American Aerospace Defense Command (NORAD)) have been found to have varying estimated sizes of objects, and so more consistent results are obtained by averaging the sizes from different RCS catalogues. Other reasons for these errors could be that either the object was not the catalogued object it was thought to be, or the orientation of the objects during the short beam passage gave an anomalously low size. The challenge of false alarms or possible errors due to the short beam can be overcome by increasing dwell time using a larger beam or several simultaneous beams.

Figure 2.4 and 2.5 show a comparison of diameters for catalogued objects which appear in the Haystack and HAX 2006 data. USSN, Haystack and HAX sizes are estimated using the NASA Size Estimation Model (SEM). Objects denoted with (.) are identified as being detected in the main lobe of the antenna beam. The solid line represents an exact match in size. The sign (Δ) indicates an object that was identified a being detected in the sidelobe. The matched line (—) represents

a match in size for objects passing through one of the sidelobes but are identified as passing through the main lobe.

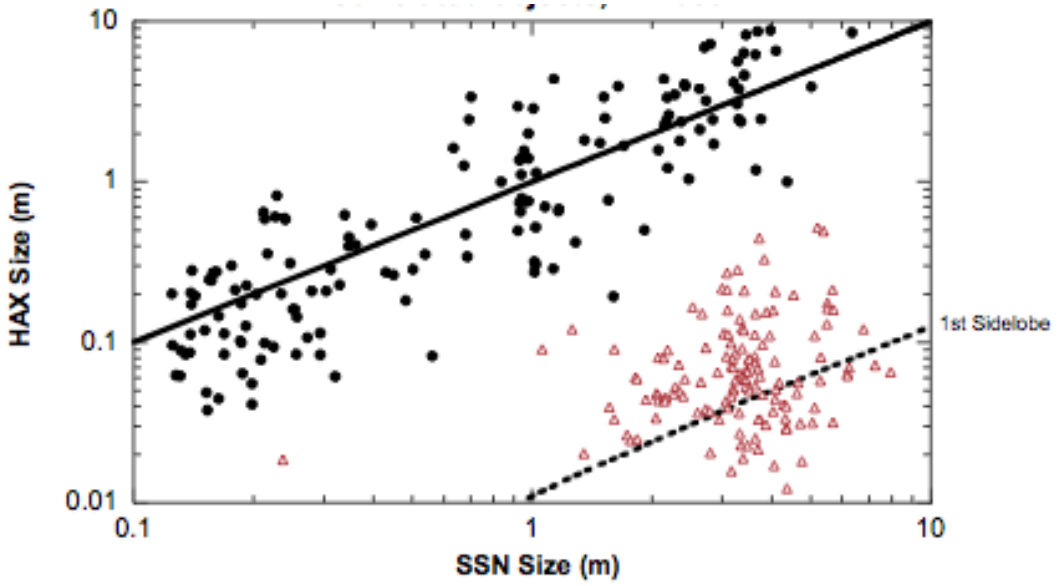

Figure 2.4: Comparison of the HAX sizes with USSN catalogued objects for radar observations carried out in 2006. The first sidelobe reduces the two-way RCS measurements by approximately -38 dB [33].

2.1.2 Tracking and Imaging Radar (TIRA)

German's Tracking and Imaging RAdar (TIRA) system is limited to the monostatic mode of operation using beam-park experiments with TIRA alone or in bistatic mode with TIRA and the Max-Planck Institute of radio Astronomy's 100 m telescope at Effelsberg (Figure 2.6). For these two operation modes, 24 hour duration snapshots can be taken to provide statistical information and rough orbital parameters for objects as small as 1 cm at altitudes up to 1000 km. During such experiments, uncatalogued small debris can be detected and possible sources identified. Examples are the droplets generated by ROSAT reactor cores and debris from a Pegasus Upper-Stage explosion [1].

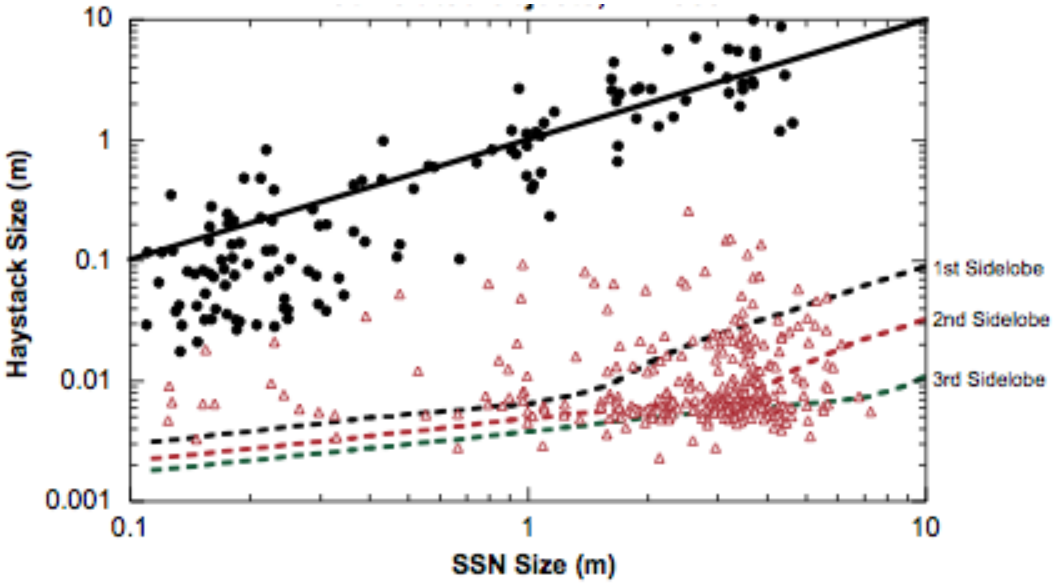

Figure 2.5: Comparison of the Haystack sizes with SSN catalogued objects. The first, second and third sidelobes reduce the two-way RCS measurements by approximately -41 dB, -49 dB and -55 dB respectively [33].

2.1.3 European Incoherent Scatter (EISCAT) Radar

In collaboration with TIRA is ESA's EISCAT radar located in Tromso, Norway. The primary mission of the EISCAT network is to perform ionospheric measurements. However, after the installation of a dedicated space-debris processing unit, it now performs statistical observations of LEO debris down to 2 cm alongside its main objectives. The EISCAT network operates a 930 MHz UHF radar (and a PRF of 200 kHz) and a 225 MHz VHF radar, with transmit peak power up to 1.5 MW through the main antenna. Furthermore, Norway owns a 500 MHz radar system consisting of a steerable 32 m dish and a fixed 42 m dish in Longyearbyen, Svalbard [36, 37].

The EISCAT radar allows continuous monitoring of the LEO debris population in a beam-park mode. For example, it was able to monitor and characterise China's Fengyun1-C debris cloud, generated at 800 km altitude in January 2007, following the worst single fragmentation event in space history [38]. Small space debris radar data obtained from EISCAT radar in collaboration with the Sodankyl'a

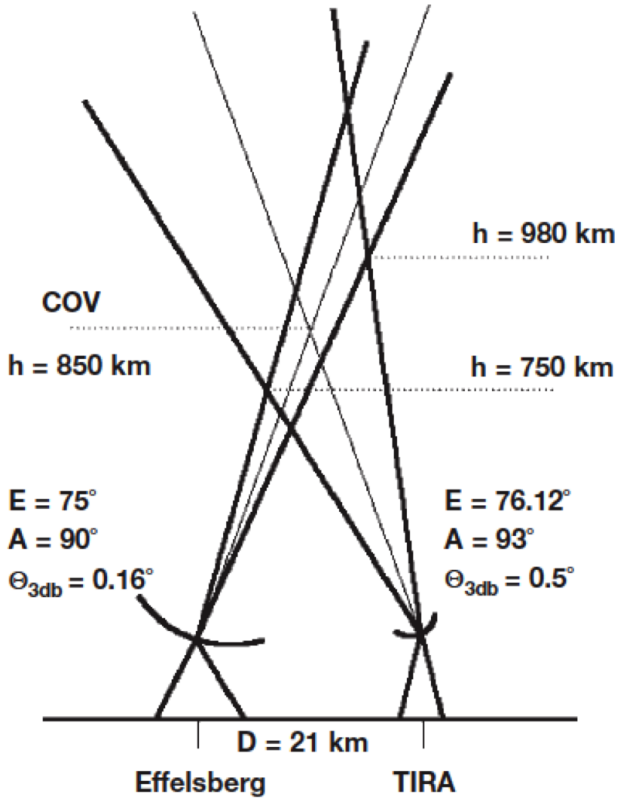

Figure 2.6: The TIRA beam-park geometry [1].

Geophysical Observatory (SGO), have shown that even though the determination of object size needs to be reviewed, the altitude distribution provides a good fit to ESA's MASTER model prediction [39]. The result shown in Figure 2.8 was obtained from 2 hours radar measurements using a 1 MW peak power, 35 m antenna, at 931 MHz, PRF of 200 kHz, pulse width of 0.5 ms, for debris at ranges of 400 km to 1400 km. The 0.27 s coherent data result is for a large catalogued debris from the Tsyklon upper stage known as 1994-11G according to the COSPAR designator. Debris 1994-11G has a diameter of 2.7 m, height of 2.2 m and a RCS of 8.3 m^2 [39].

The EISCAT radar SGO teams detected 56 objects with diameter above 1 cm from data generated over 3 hours. Comparing the size and altitude distribution of the detected small debris with the MASTER model predictions yielded the graph

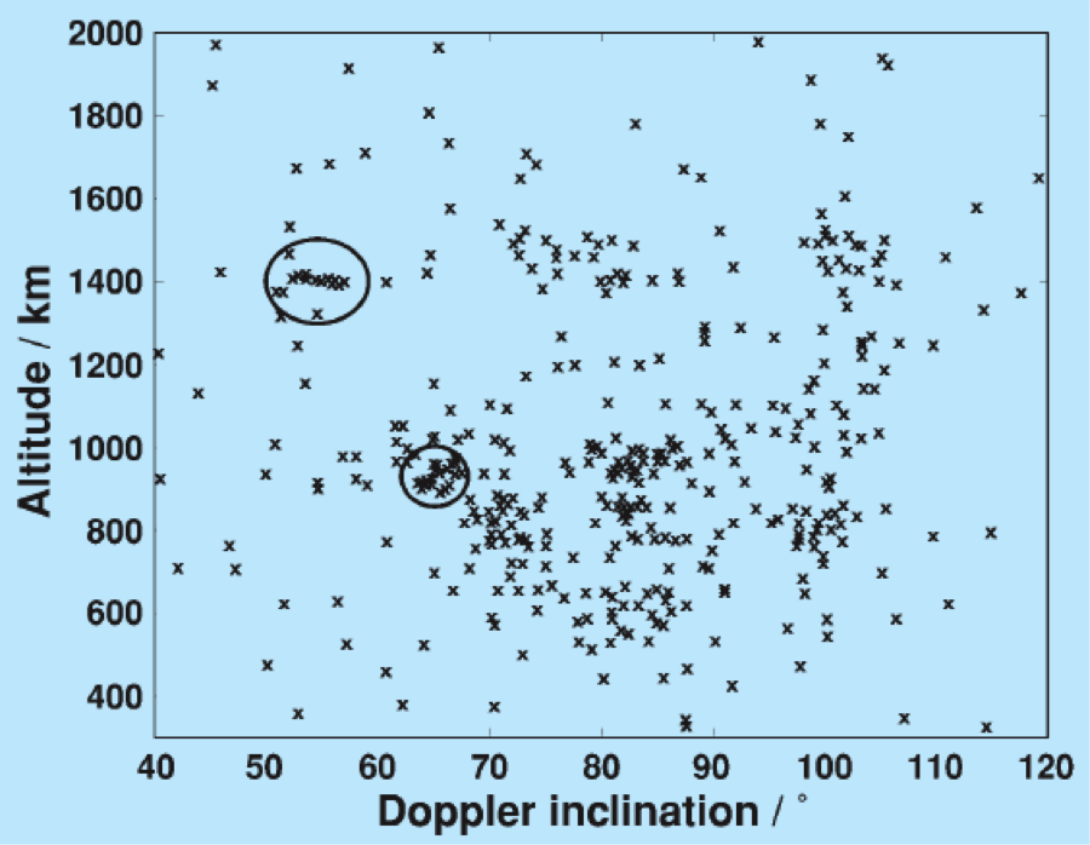

Figure 2.7: Altitude versus Doppler inclination for objects detected during the October 2000 beam-park experiment by TIRA and Effelsberg's 100 m telescope [1].

shown in Figure:2.9. Two of the main challenges the EISCAT radar experiences in detecting small space debris are: the failure to determine the debris temporal behaviour since only snap shots of the debris environment are taken, and the inability to determine orbital parameters from the radar measurements when the radar beam is pointing along the local geomagnetic field line [39].

2.1.4 Bi-static radar in Italy

The Italian bi-static C band radar that is being used for space surveillance of space debris in the LEO consists of a continuous wave transmitter located in

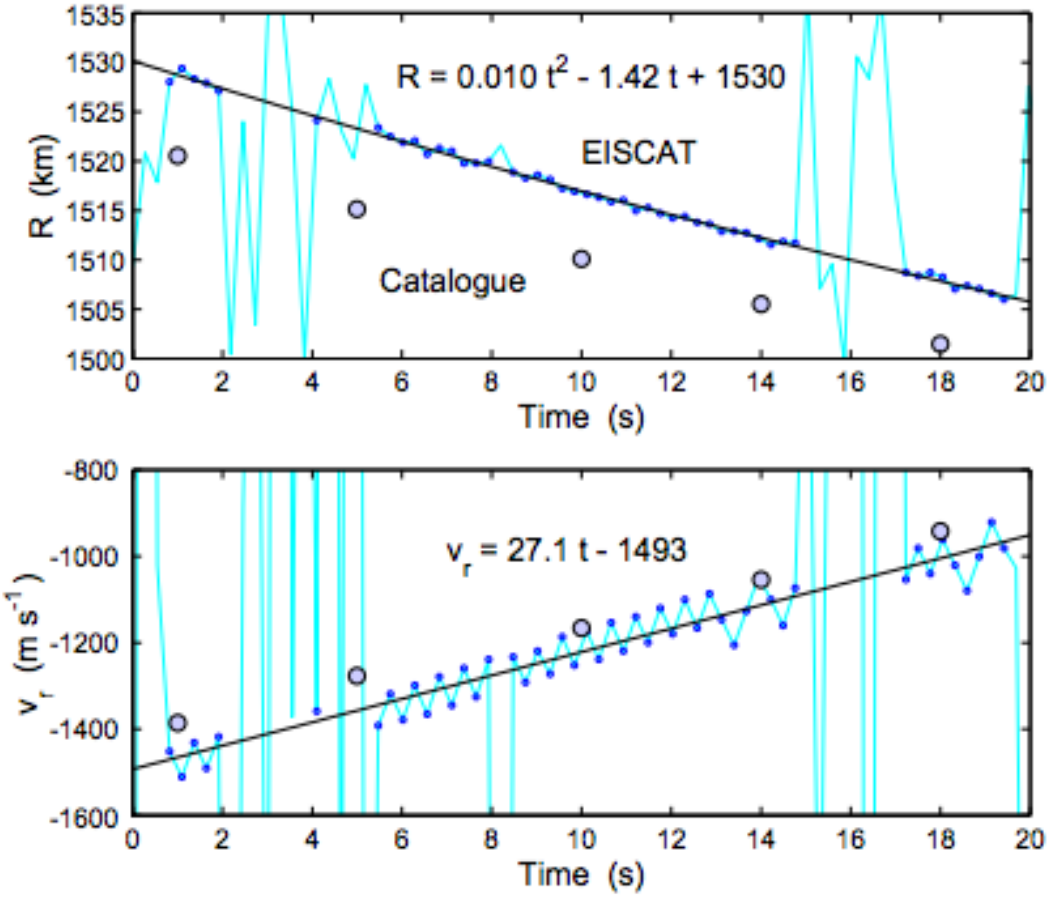

Figure 2.8: EISCAT radar first demonstration measurements on 20 February 2001, compared against the catalogue. The top panel shows the measured slant range (small circles), a parabolic fit, and the catalogue prediction (large circles). The bottom panel shows the measured Doppler velocity (small circles), a linear fit, and the catalogue prediction for the range rate (large circles) [39].

Noto and the Medicina radio telescope receiver located near Bologma. The main aim of this system is to protect COSMO-SkyMed satellites constellation. The transmitter and receiver are both parabolic antennae of diameter 32 m, separated by a baseline of about 916 km [40].

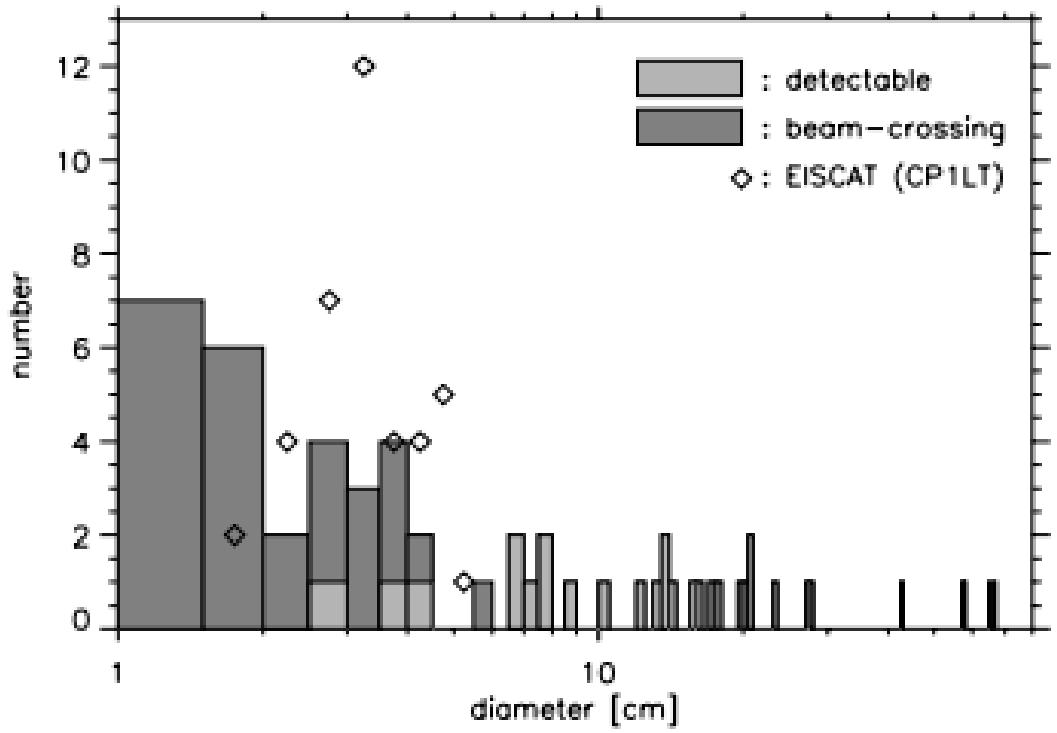

Figure 2.9: Comparison of EISCAT beam-crossing objects with the MASTER2009 model size and number predictions and cataloged objects at altitudes 400 Km to 1400 km for the 2001 measurements. The dark grey histogram shows the MASTER model, the light grey histogram shows the detectable objects, according to the model, and the distribution of sizes of actually detected objects is shown as the diamond symbols [39].

2.1.5 Medicina Northern cross

This radar uses the "Flight Termination System" (FTS) of Italian Joint Test Range of Salto di Quirra (PISQ) in Sardinia, as the transmitter, and the Northern Cross radio telescope at Medicina as the receiver. Operating in CW mode, the transmit average power is 4 kW in the bandwidth 400-455 MHz. The Northern Cross, is composed of two perpendicular arms: the East-West arm which is 564 m long and a single cylindrical antenna with a width of 35 m, the North-South arm is made of 64 parallel antennas with a length of 23.5 m and a width of 8 m each. The collecting area is 27,000 m^2 and the field of view can be populated with many independent beams [41].

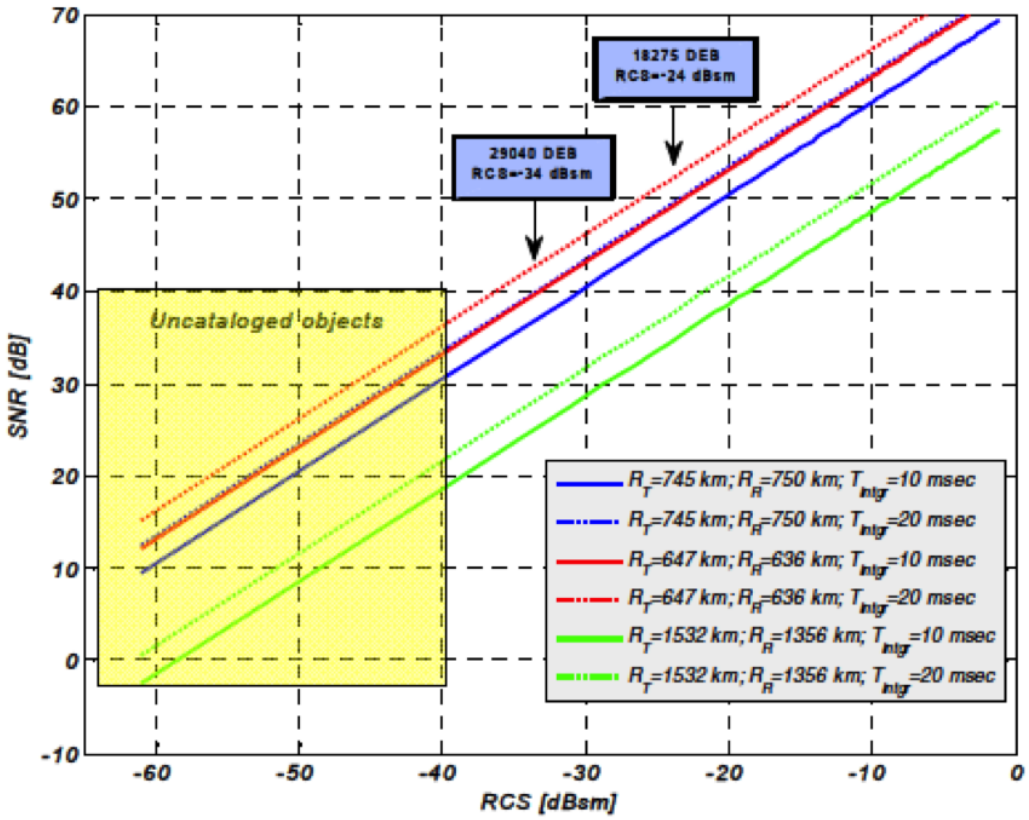

Figure 2.10: Bi-static SNR against RCS for debris at different transmitter and receiver distances of the Italian bistatic radar and for integration time intervals of 10 and 20 ms. Two NORAD catalogued objects (debris 29040 with RCS of 34 dBsm and debris 1827 with RCS of -24 dBsm) were detected at an altitude of 620 km [40].

2.1.6 GRAVES in France

The Grand Rseau Adapt la Veille Spatiale (GRAVES) bistatic radar, located in Dijon consists of a very high frequency (VHF) transmitter with planar phased array antenna of 15 m and 6 m each. It was commissioned in 2001 and is capable of detecting objects of size up to 1 m at an altitude of 1000 km and determining azimuth, elevation and Doppler rate for a large number of simultaneous targets [42]. Currently, the number of objects in its catalogue range from 2500 to 3000

[9].

2.2 Transmitter design overview

In 1970, T.Weil wrote: "The transmitter is typically one of the largest, heaviest, and most costly portions of a radar system" [43]. Modern technology has reversed this claim by enabling modification of the transmitter to make it cheaper, smaller, lighter and durable [44]. In this section, we look at available transmitter technologies and their suitability to the MeerKAT radar. Since small space debris have very small RCS, we require a high power, and yet cost effective transmitter.

A radar transmitter produces radio frequency (RF) pulses of energy, that are radiated into space by an antenna. The suitability of a particular radar transmitter depends on its ability to generate the desired peak power at a suitable RF bandwidth, duty cycle, gain and with RF stability that meets signal processing requirements. The transmitter needs also to be easily modulated to meet waveform design requirements, and it should be efficient, reliable and easy to maintain with an acceptable life expectancy and cost of the output device. The transmitter design largely depends on the selected output device [45].

The two main radar transmitter systems are: the high-Power Oscillator Transmitter (POT), which is a keyed-oscillator magnetron tube suitable for non-coherent or pseudo-coherent radars, and the high-Power Amplifier Transmitter (PAT), which constitutes a waveform generator and an amplifier (Magnetron, Klystron, Gyrotron, Twystron, Traveling Wave Tube (TWT), Solid-State or Cross-field Amplifier (CFA)), usually used in fully coherent radars. The power subsystems in a radar transmitter are the high-voltage power supply (HVPS) and the pulse modulator [46]. A special case of the PAT is the active antenna, where every antenna element or group is equipped with an amplifier.

The magnetron is an oscillator only amplifier, cross field, E and H polarisations at right angles. Even though it is relatively inexpensive, it is very noisy and can generate large spectral sidelobes. It is mainly used in non-Doppler radars.

The CFA is similar to magnetron but employs crossed electric and magnetic fields high coherent power, peak power levels of megawatts, average power in kilowatts, efficiency of greater than 50% and allows RF energy to pass through the tube unaffected when not pulsed [47]. It however requires added stages of amplification because of low gain (10 dB). The CFA has a relatively small size compared to klystron, wide bandwidths of 10 to 20%, but it is generally noisy and less stable. Klystron is a linear beam tube with efficiencies approaching 60%, relatively narrower bandwidths and in-band noise. The TWT has wide bandwidths, high gain (40 dB), low noise, lower efficiency (less or equal 25%) [48, 49]. Figure 2.11 shows a comparison of microwave tube technology in terms of average power and frequency.

Even though solid-state transmit/receive modules appear attractive for constructing phased array radar systems, microwave tube technology offers substantial advantages in power output and reliability over solid-state technology (Figure 2.12). Table 2.1 shows the comparison for linear beam tubes and cross field tubes, in terms of performance and cost [8]. Some of the companies that currently produce high power and cost effective radar transmitters include: the communications and power industries (CPI) in the USA famous for its GaN Power Amplifier [51], the H6 Systems [52], Radtech Engineering [53], Reutech radar systems in South Africa [54].

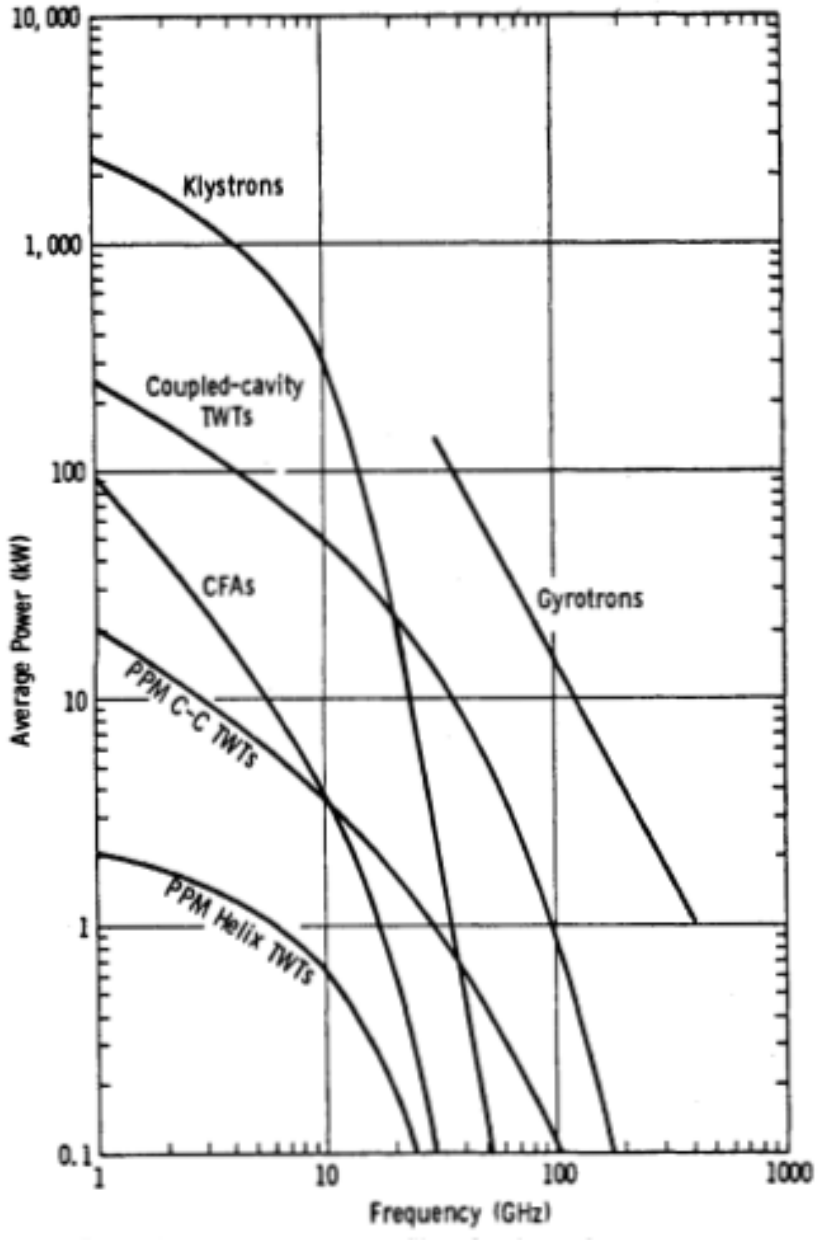

Figure 2.11: Average power capability of various microwave tubes given by Staprans in [50].

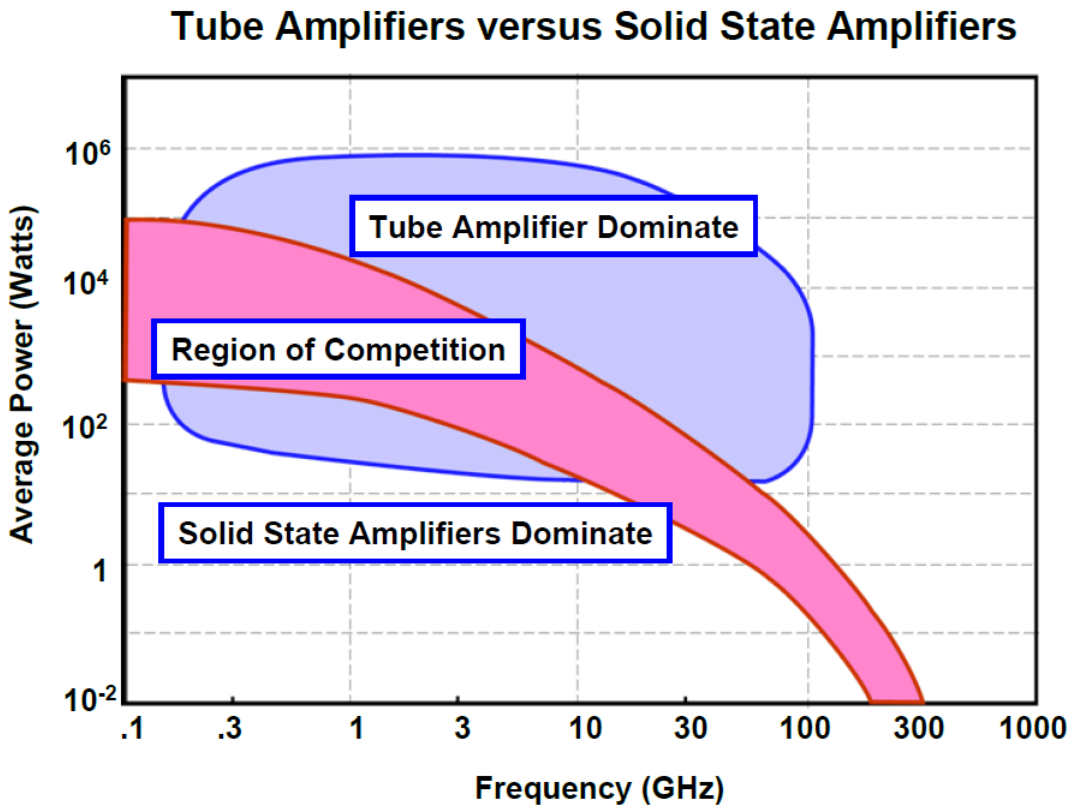

Figure 2.12: Average Power Output Versus Frequency for Tube Amplifiers versus Solid State Amplifiers[55].

Table 2.1: Skolnik's comparison of High-Power Pulsed Amplifiers for the same frequency and peak and average power output [8]. * Clustered-cavity klystron can achieve 10 to 15% bandwidth at higher cost, ** In 1 MHz bandwidth

	Klystron	**TWT**	**Conventional**	**High gain**
Voltage	High	High	Low	Low
Gain	30-70 dB	30-70 dB	8-15 dB	15-30 dB
Bandwidth	1-8%*	10-15%	10-15%	10-15%
Efficiency	15-30%	15-30%	35-45%	35-45%
Weight/size	High/Large	High/large	Low/small	Low/small
Tube cost	Medium	High	Medium	Medium
Noise**	-90 dB	-90 dB	-55 dB	-70 dB
Usable dynamic range	40-80 dB	40-80 dB	afew dBs	afew dBs

2.3 MeerKAT L-band receiver

The MeerKAT radio telescope is being constructed in the Northern Cape's Karoo desert region about 80 km north-west of Carnarvon in South Africa as a pathfinder for the Square Kilometre Array (SKA). This telescope will constitute 3% of the SKA and is funded by South Africa. The SKA, which will have up to 3000 receiver antennas covering an effective square kilometre, will be the largest radio telescope. Figure 2.13 an artist's impression of what the MeerKAT radio telescope will look like upon completion and Figure 2.14 shows the phase 1 antennas that have been completed as of 2016.

Once completed, MeerKAT will consist of 64 off-set Gregorian antennas, each fitted with an interlinked receptor that accommodates up to 4 receivers and digitisers. Of the 64 receptors, 48 are concentrated in the core area which is approximately 1 km in diameter. The maximum baseline of the telescope is 8 km. Each MeerKAT receptor consists of: a steerable dish made up of the 13.5 m main reflector, and a 3.8 m diameter sub-reflector, a set of radio receivers (L, UHF and X bands and in future S-band) and associated digitisers. The MeerKAT radio telescope will be the first telescope to demonstrate true multicasting and co-current operation of multiple instruments that are hosted on different processing boards [56].

Upon reception, the electromagnetic wave is converted into voltage, amplified using cryogenic low noise amplifiers (LNA), digitised using analog to digital converters (ADC), sampled and the data is then transferred via buried fibre optic cables to the correlator, which is situated inside the Karoo Array Processor Building (KAPB) at the Losberg site complex. The fibre cables run inside conduits buried 1 m below the ground for thermal stability. At the KAPB, the signals undergo digital processing, such as correlation, beamforming, pulsar search and pulsar timing [56].

The process of correlation combines all the signals from all (or selected) receptors to form an image of the area of the sky to which the antennas are pointing. Beamforming coherently adds the signals from all the receptors to form a

number of narrow, high sensitivity beams. Time and frequency reference signals are distributed, via buried optical fibres, to every digitiser on every receptor, so that they are all synchronised to the same clock.

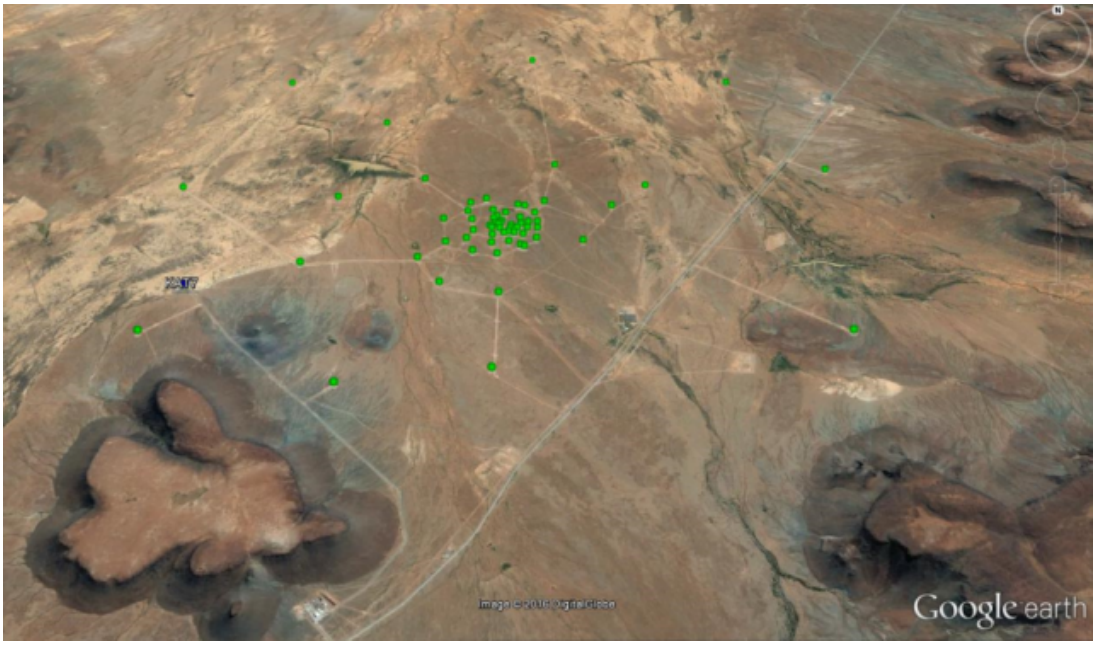

Figure 2.13: An artist's impression of what the MeerKAT radio telescope will look like on completion by 2020 [57].

Figure 2.14: Phase 1 of the MeerKAT radio telescope construction where 16 of the 64 antennas have been completed and were already in use by June 2016 [57].

The main focus of this research lies in using the MeerKAT L-band receiver as a commensal receiver (in a sense that it will be used as it is) for space debris and asteroid observations. Before we evaluate whether the existing hardware is compatible for radar application, an overview of the MeerKAT receiver,

particularly the L-band receiver, is looked at. Figure 2.15 shows the MeerKAT radio telescope DBE [56].

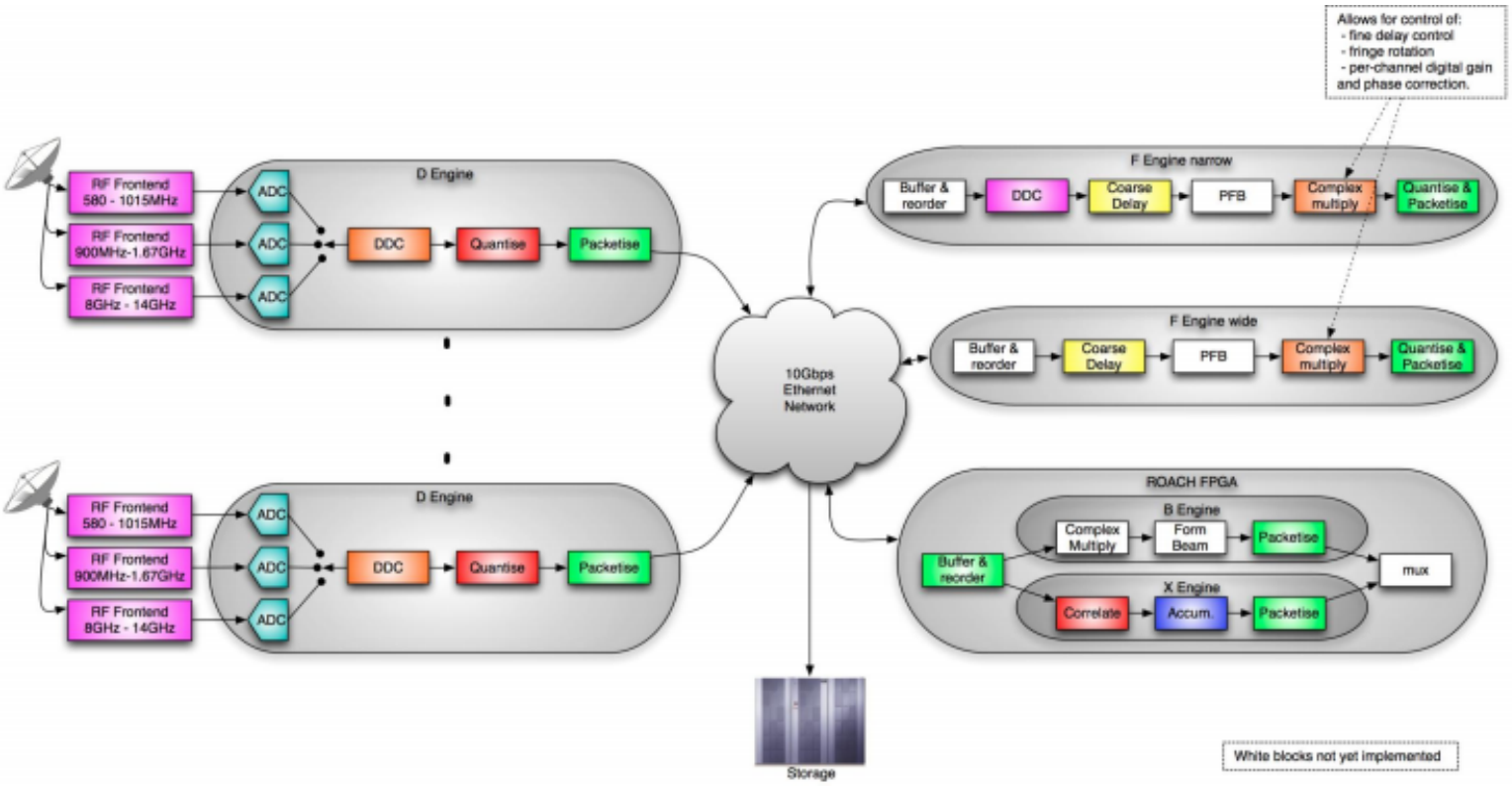

Figure 2.15: The MeerKAT radio telescope DBE for the L, UHF and X band receivers [58].

One of the advantages of the MeerKAT receiver design is the fact that the signal is digitised directly from the feed, without requirement for analog mixing. The data is then packetised, time stamped to a sub-nanosecond precision for transport to the central processor over Ethernet optical fibres for realtime (online) and offline analysis and storage and reprocessing. Direct sampling reduces the cost and complexities of an analog mixer and transporting the digital signal rather than the analog signal prevents amplitude and phase variation caused by temperature variations in the optical fibre. In addition, the typical 40 dB linear dynamic range limitation for commercial RF-over-fibre is overcome [58].

At the MeerKAT L-band receiver, the RF signal that has been reflected off the 13.4 m main reflector onto the 3.8 m sub-reflector, reaches the antenna feed, where it undergoes a number of processes. Below is a summary of the received signal path and the required data transfer speed:

1. Feed
    - L-band receiver
2. Digitiser
    - 900 MHz - 1.67 GHz RF front end
    - 10 bits ADC at 1712 Msps
    - 4 k Polyphase Filter Bank (PFB)
    - 600 μs cross plarisation correlator
    - Raw time-domain streaming at 873 Mbps
    - Digital down converter (DDC) at 34 Gbps x 64
    - Transient buffer
    - Quantiser at 1 Gbps x 64
3. Coherent summer
    - Gain scalling
    - Phase correlation
    - Steer beam
    - Sum
4. Incoherent summer
    - Antenna selection
    - Sum

2.3.1 MeerKAT FX correlator

The FX correlator (Fourier transform 'F' followed by Cross-correlation 'X') computes all four complex polarisation products for all baselines (including autocorrelations). The F-engine channelises the incoming data into spectral components, and the X-engines multiplies and accumulates every product pair. The F-engines and their ADCs are synchronously clocked from a GPS-disciplined rubidium common clock source, and the X-engines are compute nodes that operate from their own asynchronous clocks [58].

The MeerKAT correlator implements fringe rotation and delay compensation within the F-engines by employing a combination of time-domain and frequency-domain processing. This allows for phased-tracked wide-band and spectral-line observations, but it does not allow online Doppler tracking. Beamforming in the frequency domain is done by recording a copy of the channelised data destined for the X-engines, and sending it to a co-located beamformer (B-engine) which performs beam steering and summation. The existing F-engines are shared by the X-and B-engines. The B-engine only needs a single complex multiplier and adder to sum the already serialised data. It uses a lookup table to obtain steering coefficients, needed to create additional beams. In a sense, this is similar to implementing sub-arrays.

2.3.2 MeerKAT telescope data storage and usage

In the MeerKAT telescope DBE, the coherently summed beamformer operates parallel to the wide-band correlator by coinciding the channelised beamformer voltages with the correlator's channels. The correlator out put is stored in the processor for re-synthesising and re-sampling at a later stage. Data usage and streaming is done using the Streaming Protocol for Exchanging Astronomical Data (SPEAD) protocol. This protocol enables the MeerKAT radar to have multicasting capability and effective space usage by using co-current multicast groups and IP multicasting allows [59].

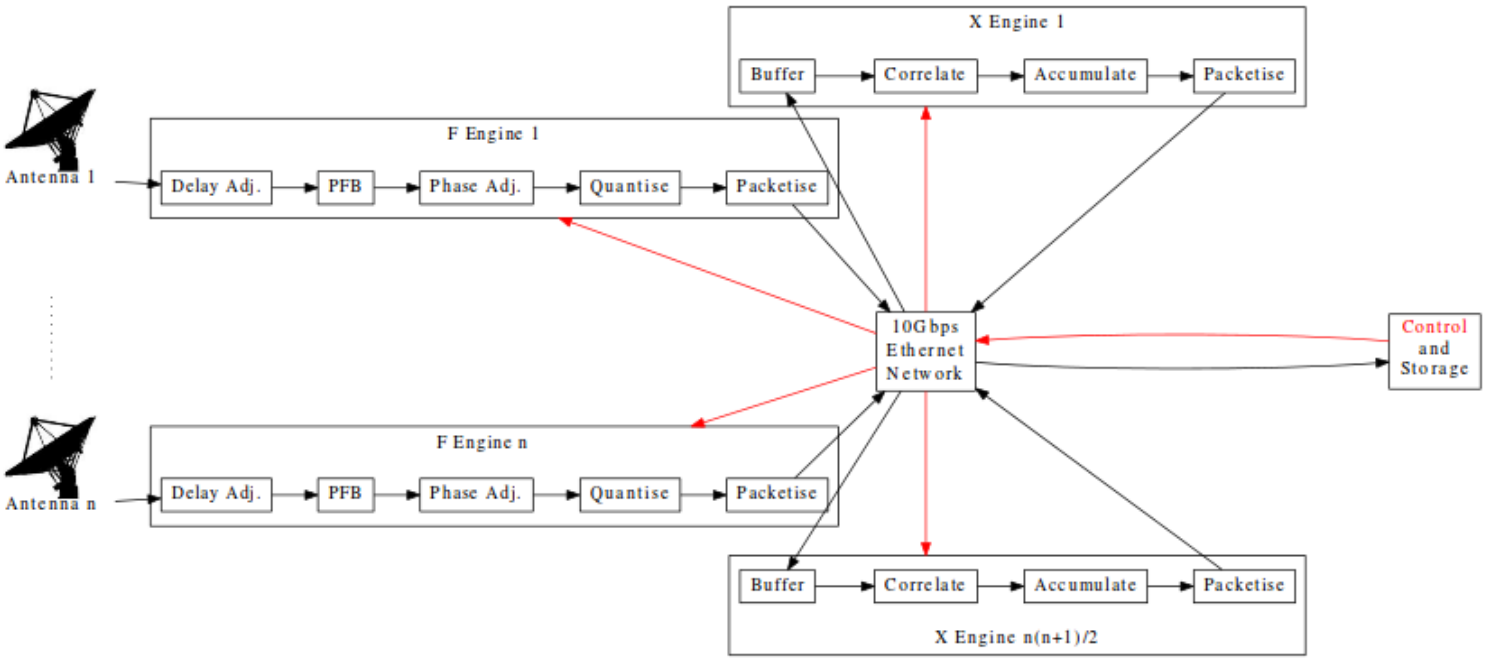

Figure 2.16: An approximation of the MeerKAT FX correlator showing the signal chain (black) for two of the telescopes and the control and monitoring (red), for one polarisation. The F-engines do the Fourier transform and X-engines do the correlations. For n antennas there are $\frac{n(n+1)}{2}$ correlation products including all autocorrelations [56].

The SPREAD protocol is a one way data transport operating over the User Datagram Protocol (UDP) on Ethernet networks. It is machine and human readable and supports multiple devices subscribing to the same data stream (or a subset of it) users to automatically unpack, comment and debug data, and perform real-time inspection and plotting. During the transmission of arbitrary structures of data, the receivers copies can be updated with changes occurring in the radar DBE, such as: correlator mode, LO frequency alteration. However, if the update of these changes is not required, a faster static mode can be implemented. For data packets being received out of sequence, buffering is used. Basing on the data rates in Figure 2.17, the MeerKAT 3D radar will collect data at the end on one or more beam out puts using a GPU box. The radar will have an option to steer the beam only when there are no other scientists using the telescope. Since time domain data is not usually stored, an observation window

would have to be scheduled to record the data. So for 16 antennas, the L-band receiver would record data at 76 GB/s and from a single dish at 1712 Msps, 10 bit, dual polarisation, plus header is about 35Gbps. To avoid the challenge of few machines for raw data and the large amount of space required, we can obtain channelised beamformed data at about 29 Gbps.

Since the MeerKAT L-band digitisers were designed to sample at 1.712 GHz, and this sampling frequency is 6.68 times above the maximum possible receiver bandwidth, the received signals will be oversampled. This is advantageous to radar signal processing because it:

- increases the ability to implement anti-aliasing filters to maximise the available bandwidth without exceeding the Nyquist limit
- increases A/D D/A resolution, SNR and dynamic range by a oversampling factor. The dynamic range required to cover targets of diameters 10 m to 1mm and a range of 300 km to 2000 km is 113 dB. This requires a ADC with 19 bits. However, with oversampling by a factor of 1712 Msps adds an extra 5 bits, enabling one to sample at 14 bits (ENOB of12).
- reduces ADC noise by taking multiple samples of the same quantity with uncorrelated noise added to each sample.

In order to implement Multi-beam digital beamforming, the receiver needs to have a narrow bandwidth, that is, less that 5% of the RF frequency. Using the channel bandwidth of MeerKAT, it is possible to divide the IF bandwidth of 400 MHz into 256 channels, with bandwidth of 1.56 MHz (0.12 % of 1.35 GHz). Also, the antenna beamwidth should not be too narrow, so that the 3 dB beamwidth in degrees is greater than the percent bandwidth.

For the bistatic set-up, the beamwidth of one MeerKAT antenna is 1.34 degrees, which is greater than the percentage bandwidth of 0.12. When the above conditions are fulfilled, phase shifters can be used to introduce a time delay in the received signal of each element, such that when all of the outputs of the time delays are summed, they add up coherently to form a beam (or sub-beams) in the desired direction.

Therefore, the MeerKAT antennas and DBE make it a suitable RF receiver for signals coming from orbiting debris and asteroids. The data will be digitised, channelised, scaled and stored in hdf5 format for post-processing. It also possible to obtain raw data upon request, however that requires more storage space compared to the pre-processed data.

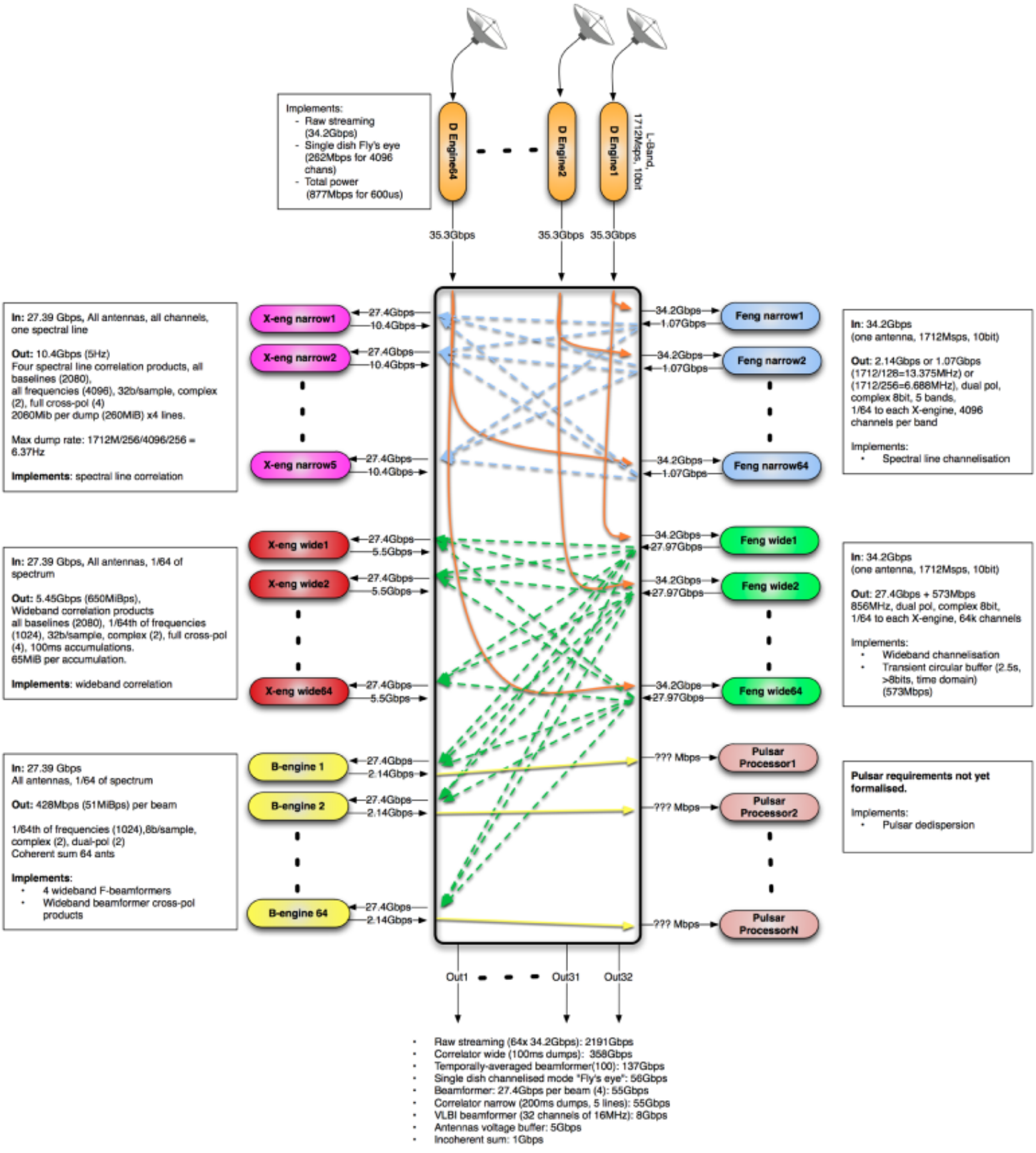

Figure 2.17: The MeerKAT L-band receiver DBE showing the digitiser (D-Engine), the Fourier transform sub-systems (F-Engine), the cross-correlation sub-systems (X-Engine) and the beamforming sub-system (B-Engine), with the corresponding data rates [56].

2.4 MIMO radar overview

Multiple Input Multiple Output (MIMO) radar is an idea that was inspired by the Synthetic Impulse and Aperture Radar (SIAR) and MIMO communication. The definition for MIMO radar has evolved since the idea first emerged. [60, 61, 62, 63] define a MIMO radar as one that enables simultaneous transmission and reception of orthogonal (or quasi-orthogonal) and/or non-correlated multiple waveforms, and the use of matched filtering to separate the multiple transmit beams. Orthogonality can be achieved within a pulse using codes or inter-pulse orthogonality [64, 65].

Some authors have challenged the novelty of the MIMO radar with distributed antennas, arguing that it is a case of the multistatic or multisite radar with sufficient spatial separation to de-correlate target RCS fluctuations by combining data from the radars incoherently [66, 67]. Others state that MIMO radar is not different from a phased array. However, phased arrays transmit a single waveform which is fed to the different antennas with different phases/delays to form a beam in a desired direction. In this case the waveforms at the different antennas are perfectly correlated [68], making MIMO radar different from a phased array.

MIMO radars can be collocated or widely spaced (statistical / S-MIMO) [69, 62]. Collocated and widely spaced MIMO radars can be used in monostatic and/or bistatc geometries. Some other MIMO subsets include: Single Input Multiple Output (SIMO), Multiple Input Single Output (MISO), Single Input Single Output (SISO) [70], Transmit-Receive MIMO (TR-MIMO) [71], Transmit Beamspace MIMO (TB-MIMO) [72] and Transmitting MIMO (T-MIMO) [73].

2.4.1 Benefits of the MIMO technique

In non coherent mode (such as the S-MIMO) the phase of the signals of interest is not controllable and a statistical approach is considered for signal processing so as to overcome target RCS fluctuations and mitigate the propagation fading. Non-coherent MIMO radar offers improved target detection, recognition,

classification and tracking accuracy.

Coherent MIMO radar controls the phase of the signals of interest and a deterministic approach is used on signal processing enabling beam forming on transmit and receive [73]. MIMO coherent processing combines the transmit and receive array patterns to form a virtual array. In MIMO radar, one can apply arbitrary and adaptive dwell scheduling through transmitting duration overlapping to improve radar scheduling performance [74].

Collocated MIMO radar offers increased spatial resolution [75], interference rejection capability, sensitivity to detecting slowly moving targets [64], better parameter identifiably [60, 62], reduces fading due to multipath and offers direct applicability of adaptive array techniques. Widely spaced MIMO radars provide increased spatial diversity [76, 71] for improved detection and angle estimation [77].

2.4.2 Drawbacks of the MIMO technique

Some of the drawbacks of the MIMO radar technique include: increased computational complexity, synchronisation challenges, spread of transmitted power compared to electronic scanning antenna. For only target detection, the MIMO configuration may not be much more superior to conventional phased arrays. However, under some conditions, MIMO coherent processing can be used to separate the scatterers by taking into account the virtual sparse array.

A radar in orthogonal waveform mode must increase integration time to compensate for reduced antenna gain by a factor of the number of transmitter elements, as compared to directed beam mode [78]. [79] establishes the SNR loss, compared to conventional radars due to transmit power loss as a result of non-coherent combination of orthogonal waveforms. However, the use of orthogonal waveforms leads to enhanced estimation accuracy for both angle of arrival and target Doppler frequency, as compared to directed beam mode.

Compared to electronic beam steering antenna power budget penalty for MIMO

is high because all the directions are illuminated at the same time. Therefore, for a given set of power budget parameters, (total emitted power, gain, noise figure) the MIMO radar needs to compensate for defocusing losses. This can be done by improving the integration time (coherent / integration), which may result in degraded detection performance in a MIMO radar compared to that of a directed beam radar for accelerating targets.

Even though most authors have shown MIMO radar superiority over conventional phased arrays, other authors claim that for certain applications and geometries, it is not always superior and the computational requirements may outweigh its benefits. Dr. Eli Brookner in [80, 81, 82] gives an analysis for a full/thin MIMO radar whose performance is similar to the conventional phased array radar. However, the choice to use a MIMO or multistatic or phased array approach depends on the radar geometry, target environment and the required applications.

2.4.3 Focus on the SIMO technique

In this research, we are not attempting to prove the MIMO radar superiority, but rather to evaluate its suitability to the MeerKAT telescope receivers. The target environment may be inform of a single large asteroid or a cluster containing several small space debris. In order to detect and track the targets accurately, one needs radar data that will provide a high SNR and good range, Doppler and angular resolution. In order to make use of the MIMO radar advantages while minimising its trade offs (such as how to exploit the transmit geometry to effectively enhance parameter estimation) and computational load (in terms of required matched filters), we propose the use of a SIMO radar.

A SIMO radar uses a single antenna on transmit and perform beamforming on receive only. The motivation for this choice comes from [68]) who showed that in certain radar scenarios, the MIMO and SIMO and Phased array radar performances are similar. Here the receiver array geometry is relatively straightforward to exploit, since each transmit-receive channel is known [83].

SIMO radar takes advantage of the MIMO radar benefits while limiting the MIMO radar constraints.

2.5 Chapter 2 summary

This chapter was an overview of some results and challenges experienced by available dedicated or contributing terrestrial radars for detection and tracking of small space debris and PHAs. The design of a high power and cost effective transmitter was discussed based on available technology and its suitability to the MeerKAT radar.

A detailed description of the MeerKAT radio telescope receiver sub-systems was given, showing the relevant subsystems from the L-band receiver to digitiser, sampler, channeliser, correlator, beamformer and finally to data storage. A brief overview of the MIMO and SIMO techniques and used in radar were given, clearly stating the different types, their benefits and drawbacks. It was clearly stated that the SIMO technique is of interest to this analysis because of its suitability, simplicity and less computational requirements compared to other MIMO subsets.

Basing on the MeerKAT digital back end and data rates, it is proposed that raw data be obtained directly after the digitiser and then down-sampled, or channelised data at lower data rates to be recorded. The bistatic, multistatic and SIMO radar configurations are chosen to be evaluated in terms of detection, tracking and imaging as elaborated in the preceding chapter.

Chapter 3: MeerKAT radar, proof of concept

This chapter gives a description of the MeerKAT bistatic radar as a proof of concept indicating the minimum detection and tracking capabilities. The bistatic radar specifications are formulated, justifying the choices for transmitter, receiver and target parameters. A geometry analysis was done to determine the maximum achievable dwell time for the receiver minimum and maximum elevation and azimuth angles.

Then a sensitivity analysis was performed to determine the lower and upper limits for RCS and SNR. This theoretical analysis was validated by radar simulations for coherent processing. Lastly, range-Doppler ambiguity compensation methods were discussed and implemented in theory and simulations. This feasibility study offers the minimum performance of the MeerKAT radar as per the radar specifications given in this study. It is a test for the radar design and methodology chosen by comparing theoretical and simulated performance.

3.1 MeerKAT radar: Transmitter

A suitable transmitter for the MeerKAT radar would be a Power-Amplifier-Transmitter, in which a high-power amplifier is driven by a highly stable continuous RF source or waveform generator. By keeping the RF source phase stable and making sure that the RF is a multiple of the PRF, each

Figure 3.1: The transmitter and receiver locations on the South African map. The transmitter is 435 km from the receiver location. [85]

pulse starts with the same phase thus maintaining full phase coherence from pulse to pulse. A coherent radar system enables the ability to differentiate small changes in velocity that correspond to small changes in phase. This Doppler resolution improvement is in addition to the SNR gain that is obtained after coherent processing [84]. Both SNR and Doppler resolution are important when detecting small space debris and PHAs because of the low levels of return signal voltage and the closeness of objects' radial velocities.

The proposed transmitter location is Denel Overberg Test Range (DOTR) in Cape Town, South Africa, latitude 34^{o}36'9.92" S, longitude 20^o 18' 9.74" E, altitude 20 m. This choice was based on the availability of infrastructure and the suitability of the site. It should be noted that the transmitter parameters and location are not limited to the ones used for this analysis, this is merely a case study of an optimal site in the receiver's field of view. Figure 3.1 is a Google map showing locations of the proposed transmitter site (Denel OTR) and the KAT-7/MeerKAT/SKA radio telescope site.

3.1.0.1 Radio frequency interference (RFI) analysis

Using the Egli propagation model and assuming two worst case scenarios: the transmitter's main lobe and first side lobe pointing in the direction of the receiving antenna, the amount of power that would reach the receiver is calculated. This value is then compared to the RFI threshold levels for the SKA site as defined by the International Telecommunication Union (ITU) for a radio quiet zone, which is -260 dB(W/(m^{2}Hz)) at 1.35 GHz. This analysis can be extended to determine other possible transmitter sites, but we limit it to evaluating the suitability of the proposed DOTR site [86].

The Egli equation for a particular transmit power, P_t (10 kW), transmitter/receiver gain, G_t/G_r, transmitter/receiver height, H_t/H_r and baseline L, predicts the RF path loss for point to point links. It is derived from real world data and it is suitable for irregular terrain. It however, does not take into account signal propagation through vegetation so it should only be used as a first order approximation. The Egli propagation path model is applicable for the ITU very high frequencies,VHF (30 MHz-300 MHz) and the ultra high frequencies, UHF (300 MHz-3 GHz) [87].

$$P_r = P_t G_t G_r \Big(\frac{H_t H_r}{L}\Big)^2 \Big(\frac{40}{f_c}\Big) \tag{3.1}$$

This section showed that the transmitter parameters and location chosen are suitable to use for a radio telescope receiver in a "radio quiet" zone, without causing interference to the telescope operation. The RFI calculated from both the main beam and the first sidelobe is below the recommended SKA power threshold levels as shown in Figure 3.2.

3.2 MeerKAT radar: Receiver

The receiver is one of the MeerKAT radio telescope antennas and the L-band receiver back end is shown in Figure 3.3. The RF signal is received by the

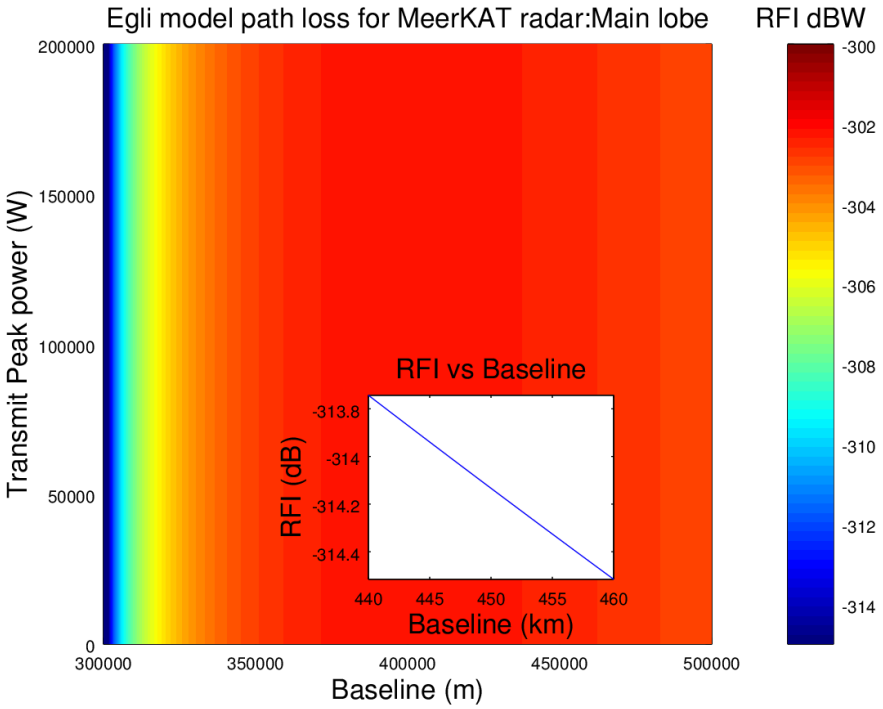

(a) Egli's power propagation from transmitter main lobe to receiver.

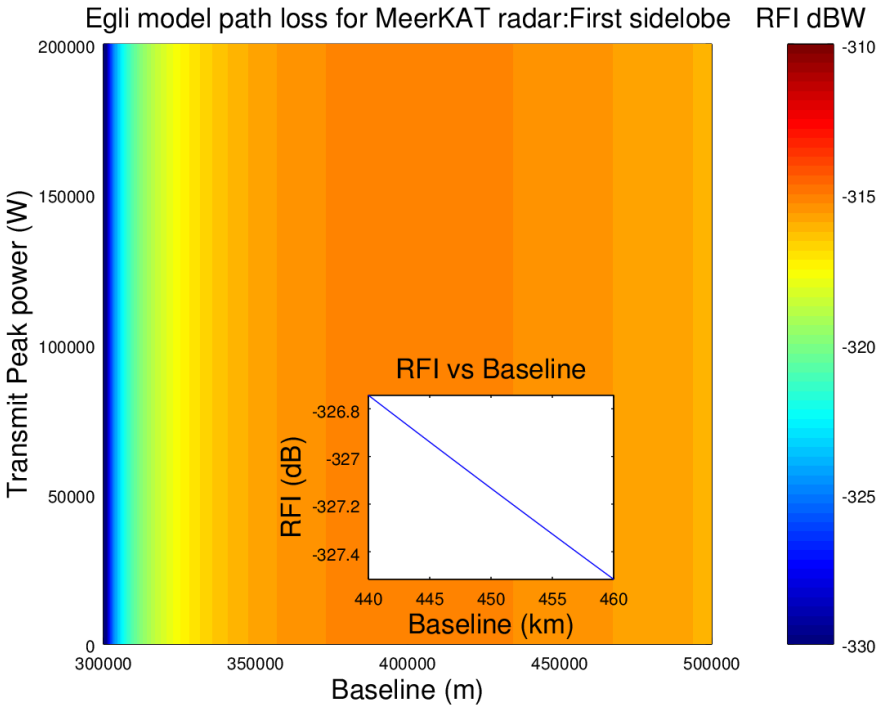

(b) Egli's power propagation from transmitter first sidelobe to receiver.

Figure 3.2: Single dish power levels below the threshold of -260 dB(W/(m^{2}Hz)) at 1.35 GHz. The zoomed in plot shows RFI from a 10 m diameter transmitter of height 19.5 m to a 13.4 m antenna of height 19.5 m separated by 450 km.

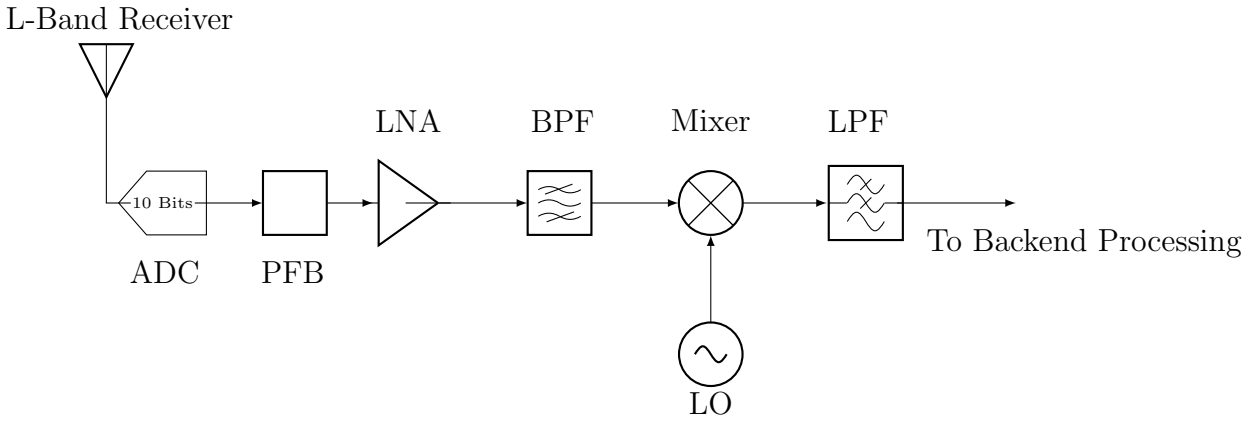

Figure 3.3: The MeerKAT radar receiver back end showing the L-band antenna feed that receives RF at 900 MHz-1.67 GHZ, the 10 Bits, 1712 Msps ADC, then the 4k PFB, the L-band high gain LNA, BPF to reject undesired frequencies, the mixer, the 2GHz LO and the LPF to remove high frequencies from the mixer. The data rate at the receiver input is 35 Gsps and at the output is 1 Gbps, for one antenna.

L-band feed (900 MHz-1.67 GHz) and is sent to the digitiser (located on the antenna) which consists of a 10 Bit 1712 Msps ADC (effective number of bits =7.6) and polyphase filter bank (PFB). The digitised signals are then filtered and downsampled in the PFB due to the high ADC sampling rate. The polyphase filter splits sample streams into different frequency channels, thereby allowing radio Astronomy users to control the frequency response of each channel. With careful design, a PFB can enable near ideal signal reconstruction after channeling. In essence, the PFB mimics independent quadrature downconverters with more computational efficiency. Table 3.1 gives the radar parameters with justification for each of the choices made.

3.2.1 Geometry and target specifications

Due to slow antenna rotation of the MeerKAT receivers (2^o/s in azimuth and 1^o/s in elevation), the high speed of motion for debris and asteroids and the geometry limited dwell time, we assume that the transmit and receive antennas

Table 3.1: Parameters used in the bistatic radar set-up

Parameter	Value (Units)	Reason
Transmitter		
Type	Pulsed	High gain
f_c	1.35 GHz	L-band (IEEE)
P_T	10 kW	Minimum value
B	10 MHz	$\Delta R = c/2B = 15$ m
D_T	10 m	Existing antenna size
G_T	40.789 dBi	From existing antenna
BW_T	1.61^o	From existing antenna
L_T	2 dB	Expected value
Duty factor (DF)	15 %	τ_{min}=2μs, τ_{max}=1ms
PRF (Base)	150 Hz	$R_{max,unamb}$=1000 km
PRF (High)	75 kHz	$v_{max,unamb}$=8.325 kHz
τ	5 μs	τB=50
Receiver		
D_R	13.5 m	MeerKAT antenna
G_R	43.395 dBi	MeerKAT antenna
BW_R	1.34^o	MeerKAT antenna
T_s	20 K	MeerKAT antenna
Azimuth	-185^o to 275^o	MeerKAT antenna
Elevation	$15^o$to 88^o	MeerKAT antenna
f_s	25 MHz	Oversampling gain of 3.9794 dB
L_R	2 dB	Expected value

are stationary. Any form of beam scanning is accomplished through beamforming as illustrated in chapter 4.

Debris orbital parameters are obtained from the NORAD two line element (TLE) database, then converted to Earth centred Earth fixed (ECEF) Cartesian coordinates and then to the local East North Up (ENU) Cartesian coordinates. Five representative catalogued small orbital debris are chosen arbitrarily, all within an altitude of 700 km and 900 km, where the largest orbital debris flux is in the LEO according to debris evolution models and measurements. The missions from which the representative small orbital debris are chosen are:

- Fengyun-1C debris generated on January 11^{th} 2007 from the Chinese anti-satellite missile test, where the Chinese weather satellite Fengyun-1C was destroyed by a kinetic kill vehicle traveling at a speed of 8 km/s in the satellite's opposite direction. In October 2007, 2150 pieces of debris from this event were catalogued [88].

- Iridium 33 and Cosmos 2251 debris from the first (and possibly the worst) accidental hypervelocity collision between two intact artificial satellites in the LEO. On February 10^{th} 2009, Iridium 33, an active communication satellite and an inactive Russian Cosmos 2251 satellite collided at an altitude of about 800 km. This collision produced $\approx$ 2,000 pieces of debris, measuring at least 10 cm (4 inches) in diameter, and thousands more smaller pieces [88].

- Delta-1 debris, one of the American Delta family of expendable launch systems that has provided space launch capability in the United States since 1960 [21].

- DMSP-5D2 (Defense Meteorological Satellite Program Block 5D2) was the tenth version of the military meteorological satellites of the DMSP. In April 2004, a 13-year-old DMSP-F11 spacecraft experienced a catastrophic breakup that produced 56 pieces of cataloged space debris.

A TLE is a data format encoding a list of orbital elements of an Earth-orbiting object for a given epoch obtained from simplified perturbation models. Using suitable prediction formula, the present or future state (position and velocity) can be estimated to some accuracy. For all trackable objects, classified or not, NORAD creates corresponding TLE data describing their orbits and trajectories around Earth. From an object's TLE set, we obtain the epoch (date and time), ballistic coefficient (ability to overcome air resistance in flight) Db, semi-major axis a, inclination i, right ascension of the ascending node(RAAN) Ω, eccentricity e, argument of periapsis ω, mean anomaly, μ and mean motion, n [10].

From these parameters, we are only interested in the six Keplerian elements $(a, e, i, \omega, \Omega, \mu)$, which describe the orbit size, orbit shape, orientation of orbit

with respect to Earth's Equator, position of orbit in the low point perigee with respect to Earth's surface, location of ascending and descending orbit locations with respect to Earth's Equatorial plane, objects's motion within the orbit with respect to perigee, respectively. Debris latitude, longitude, altitude, linear orbital speed, azimuth and elevation angles relative to the Earth station (in this case the transmitter) are derived from orbital elements and summarised in Table 3.2.

The orbital linear speed, v can be calculated from the Gravitational parameter, μ, the Earth's radius, R_E and the semi-major axis, a.

$$v = \sqrt{\mu\Big(\frac{2}{R_E} - \frac{1}{a}\Big)} \tag{3.2}$$

The Earth station/transmitter elevation angle (E) to orbital debris can be obtained from the debris altitude, H and the great circle angle between the Earth station (transmitter) and orbital debris, N_{gc}.

$$\mathrm{E} = \tan^{-1}\left(\cos\left(\frac{N_{gc} - R_E}{H + R_E}\frac{1}{\sin(N_{gc})}\right)\right) \tag{3.3}$$

The Earth station azimuth angle to debris measured from true North (A) is given obtained from the debris longitude (lon_d), debris latitude (lat_d), Earth station latitude (lat_{tx}), substation longitude and latitude (lon_s, lat_s) and inclination (i).

$$\mathrm{A} = \tan^{-1}\left(\frac{\sin(\mathrm{lon}_d - \mathrm{lat}_d)}{\sin(\mathrm{lat}_{tx})\cos(\mathrm{lon}_s - \mathrm{lat}_s) - \tan(i)\cos(\mathrm{lat}_{tx})}\right) \tag{3.4}$$

The slant range (S in metres) between an earth station/transmitter and orbital debris s given by:

$$S = R_E\left(\frac{\sin(N_{gc})}{\cos(\mathrm{E} + N_{gc})}\right) \tag{3.5}$$

The following assumptions were made in describing debris orbits:

- a stationary Earth

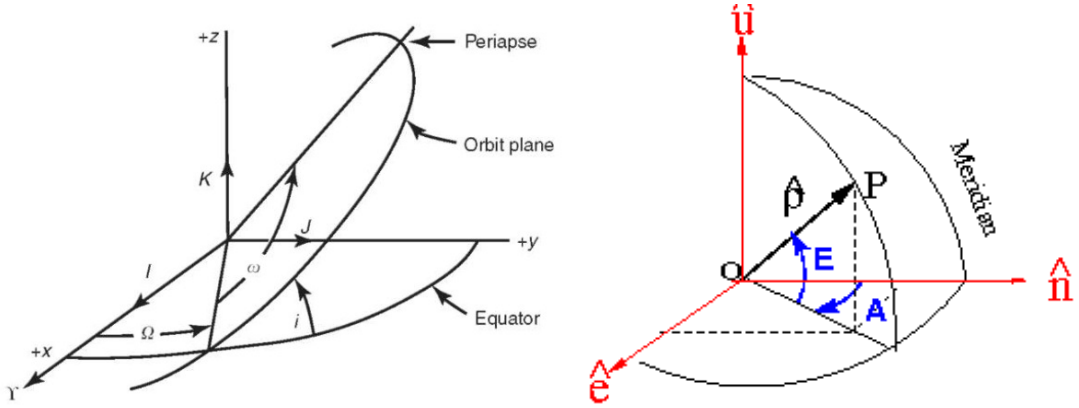

(a) Orbital elements to ECEF (b) ECEF to ENU

Figure 3.4: Illustration of orbital elements transformed into geocentric ECEF, then to geodetic ENU Cartesian coordinates [89]. E is the elevation, A is the azimuth and P is the altitude.

- origin of all coordinates is located at the Earth's centre
- debris and Earth are spherically symmetric (point masses)
- debris are subject to only the gravitational attraction from Earth
- gravitational force varies as the inverse ratio to the square of the distance between centres of mass
- debris orbit is approximately circular ($e \approx 0$)

Following the assumptions given above, conversion equations for latitude-longitude-height (h_d) above mean sea level to geocentric ECEF to geodetic ENU, are formulated as illustrated in Figure 3.4.

Let $\overline{P}$ be a 3 by 1 vector of ECEF coordinates, then:

$$\begin{bmatrix} \overline{P}_x \\ \overline{P}_y \\ \overline{P}_z \end{bmatrix} = \begin{bmatrix} r_s \cos(\lambda_s) \cos(\text{lon}_d) + h_d \cos(\text{lat}_d) \cos(\text{lon}_d) \\ r_s \cos(\lambda_s) \cos(\text{lon}_d) + h_d \cos(\text{lat}_d) \sin(\text{lon}_d) \\ r_s \sin(\lambda_s) + h_d \sin(\text{lat}_d) \end{bmatrix} \tag{3.6}$$

where:

$$\lambda_s = \tan^{-1}\left((1-f)^2 \tan(\text{lat}_d)\right) \tag{3.7}$$

$$r_s = \sqrt{\frac{R^2}{1 + (\frac{1}{(1-f)^2-1}) \sin^2(\lambda_s)}} \tag{3.8}$$

and f is the Earth's flattening , R is the Equatorial radius obtained from the WGS84 planet model. Note that the matrix P may generate unexpected errors at latitudes of $\pm 90^o$ due to singularity at the poles.

$$\begin{bmatrix} \overline{X} \\ \overline{Y} \\ \overline{Z} \end{bmatrix} = \begin{bmatrix} -\sin(\text{lat}_d) & 0 & \cos(\text{lat}_d) \\ 0 & 1 & 0 \\ -\cos(\text{lat}_d) & 0 & \sin(\text{lat}_d) \end{bmatrix} \begin{bmatrix} -\cos(\text{lon}_d) & \sin(\text{lon}_d) & 0 \\ \sin(\text{lon}_d) & \cos(\text{lon}_d) & 0 \\ 0 & 0 & 1 \end{bmatrix} \begin{bmatrix} \overline{P}_x \\ \overline{P}_y \\ \overline{P}_z \end{bmatrix} \tag{3.9}$$

Table 3.2: Table summarising transmitter, receiver, debris East (Y) North (X) Up (Z) values for selected in-orbit debris, debris altitude (H) and radial speed (v). Orbital elements were obtained from NORAD TLE sets on 29^{th} September 2016, epoch=16273.09571677.

	X (km)	Y (km)	Z (km)	H (km)	v (km/s)	σ (m^2)
Transmitter	0	0	0	0.02		
Receiver	106.2	429.6	-14.4	1.038		
Fengyun-1C	3054.3	-6344	-4145.4	885	7.41	0.0065
Iriduim 33	3565.5	4380.6	11.15	830	7.44	0.0068
Cosmos 2251	-4054.8	5410	-8636.8	728	7.49	0.005
Delta 1	6791.8	2017.7	-6341	901	7.49	0.0045
DMSP-F11	1182.6	6959.9	-4618.8	818	7.44	0.007

In order to determine the time for which a debris object orbiting at a certain radial velocity remains in the bistatic resolution cell, (dwell time for detection or track time if the radar is used in tracking mode), the resolution cell area is calculated from the bistatic angle (β), transmitter/receiver 3 dB beamwidth

Table 3.3: Table of debris simulation parameters: transmitter to target range (R_T), target to receiver range (R_R), transmitter azimuth(θ_T), for the two geometries as a result of the minimum and maximum receiver azimuth angles (185^o and -275^o).

Debris	R_T (km)	R_R (km)	θ_T^o	α_T^o
Fengyun-1C	817.2	8464.5	-64.3	-30
Iriduim 33	5648.2	5251.5	51	0.12
Cosmos 2251	10968	10792	-53.2	-51.9
Delta 1	9508	9340.5	16.5	-41.8
DMSP-F11	8436.4	8062.5	80.4	-33.2

(BW_T, BW_R), linear 3 dB beamwidth of the transmitter and receiver ($W_T = R_T BW_T$ and $W_R = R_R BW_R$) and the pulse width (τ). The effective linear beamwidth of the transmitter and receiver beams between two adjacent isorange contours separated by the range resolution (or the transverse dimension of the resolution cell), is given by [90]:

$$W_E = \frac{\sqrt{2} W_T W_R \sec(\beta/2)}{\sqrt{W_T^2 + W_R^2}} \tag{3.10}$$

Combining W_E with the bistatic range resolution ($1/2 c\tau \sec(\beta/2)$) yields the bistatic resolution cell area in 2D, A_{cb} given by:

$$A_{cb} = \frac{1}{2} c\tau W_E \sec(\beta/2) \tag{3.11}$$

3.2.1.1 Coherent integration limitations

The instantaneous Doppler frequency f_D for a target approaching a radar with radial velocity, v_r is $f_D = 2v_r/\lambda$. If the target is moving at a constant radial acceleration a, then the change in Doppler frequency in the coherent processing

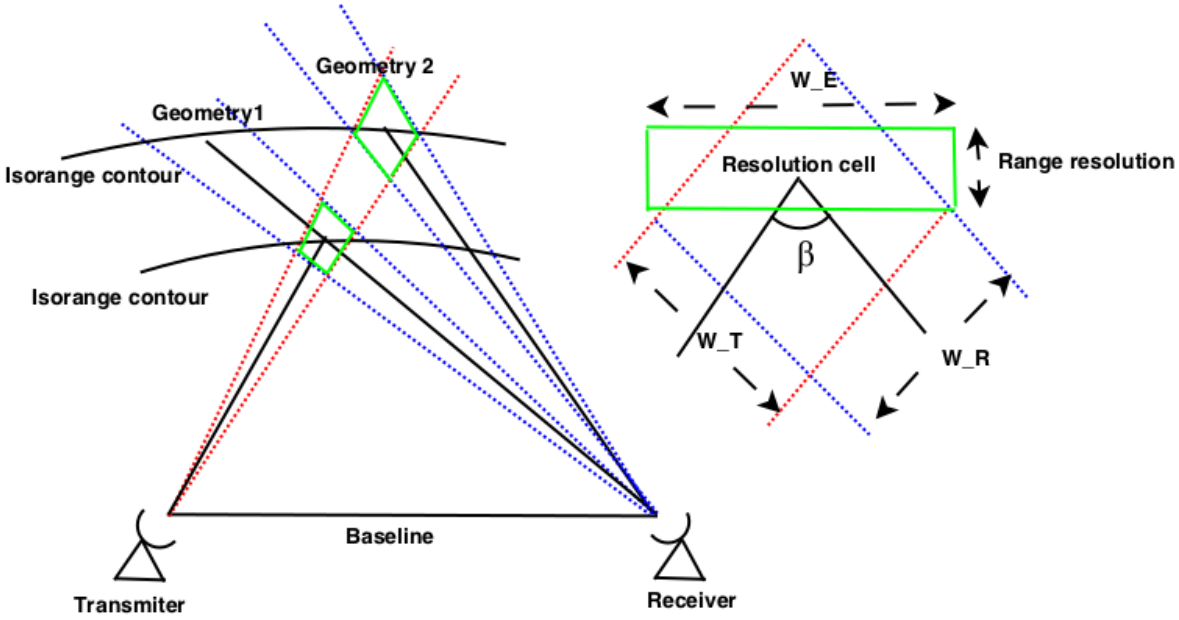

Figure 3.5: Illustration of the two geometries used in the MeerKAT Bistatic radar analysis. In geometry 1, the receiver azimuth=-185^o, elevation=15^o and in geometry 2, the receiver azimuth=275^o, elevation=88^o, both of which are lower and upper limits of the meerKAT antenna beam. Image reconstructed using the bistatic radar geometry described by McJackson in [90].

interval (CPI) is given by:

$$\Delta f_D = \frac{2aT_{cpi}}{\lambda} \tag{3.12}$$

In order for the target to remain in a single Doppler bin ($\delta f_D = 1/T_{cpi}$) during the CPI, the following condition must hold:

$$\Delta f_D \leq \delta f_D \tag{3.13}$$

which leads to the CPI for accelerating and non-accelerating targets, respectively given by:

$$T_{cpi} \leq \sqrt{\frac{\lambda}{2a}} \tag{3.14}$$

Table 3.4: Table of resolution cell area (A_{cb}) in km^2, effective beamwidth (W_E) in km, and maximum dwell time (T_{dwell}) in seconds for two geometries arising from the minimum and maximum receiver azimuth angles. The negative dwell times arise from geometry ambiguities and are neglected in further analysis.

Debris	$A_{cb,1}$	$W_{E,1}$	$T_{dwell,1}$	$A_{cb,2}$	$W_{E,2}$	$T_{dwell,2}$
Fengyun-1C	15.67	44.5	6	70.4	94.3	127.3
Iriduim 33	130	-255	-34.4	21.7	104.2	14.07
Cosmos 2251	170	413	55.5	315	563.4	75.7
Delta 1	346	-1737	-231.9	508	211	28.1
DMSP-F11	80.9	-248	-33	30.3	152	20.4

$$T_{cpi} \leq \frac{c}{2v_r B} \tag{3.15}$$

Increasing the CPI leads to range migration (details in Section 1.3). For orbital debris in a circular LEO, we assume that the only force acting on the object is the centripetal force due to Earth. So, the approximate acceleration from orbital mechanics is given by:

$$a = \frac{v_r^2}{(R_E + R)} \tag{3.16}$$

Table 3.5 shows the maximum possible CPI for a high PRF (75 kHz) and low PRF (150 Hz) and for geometries 1 and 2 (minimum and maximum receiver azimuth angles). The CPI values calculated are used for the bistatic radar sensitivity analysis shown in Figures 1.6, 1.7 and 1.8. It should be noted that most of the CPI values may not be practically achievable for this radar.

The SNR vs diameter plots (Figures 3.7 and 3.8) show that the bistatic radar will only be able to detect small debris below 700 km for dwell times of about a minute, otherwise, all the other geometries give a SNR below zero. Therefore, either transmit power should be increased or we can use more receivers to improve detection. Using all the MeerKAT receivers would increase the SNR by a factor of 64, without considering processing gain.

Table 3.5: Table of radial acceleration, a, radial velocity, v, maximum CPI, T_{cpi} and Doppler resolution, δf_D for the chosen small orbital debris.

Debris	v_r (km/s)	a (m/s^2)	T_{cpi} (ms)	δf_D (Hz)
Fengyun 1C	7.41	0	2.02	494
		7.57	121.15	8.25
Iridium 33	7.44	0	2.01	496
		7.69	120.20	8.32
Cosmos 2251	7.49	0	2.00	499
		7.90	118.59	8.43
Delta 1	7.49	0	2.00	499
		7.71	120.04	8.33
DMSP-F11	7.44	0	2.01	496
		7.70	120.12	8.32

Increasing the transmit power to 2 MW using a low cost Gallium Nitride (GaN) High Electron Mobility Transistors (HEMT) amplifier, the bistatic SNR is improved (Figure 3.9), but the it is still below the desired SNR of 13 dB corresponding to P_D of 88% and P_{fa} of 10e-6. In Chapter 4, we show the SNR improvement by increasing the number of receivers and applying beamforming.

In this section, we showed how the target parameters were derived from TLEs and the required coordinate conversions. We also gave a description of the radar receiver and the data rates needed to collect the radar data from the L-band feed. We performed a bistatic geometry analysis showing the maximum possible dwell times and coherent integration limitations for accelerating and non-accelerating targets. Coherent and non-coherent bistatic SNR calculated was below the require threshold of 13 dB. Target detection would be possible in the bistatic mode, but the SNR needs to be improved further.

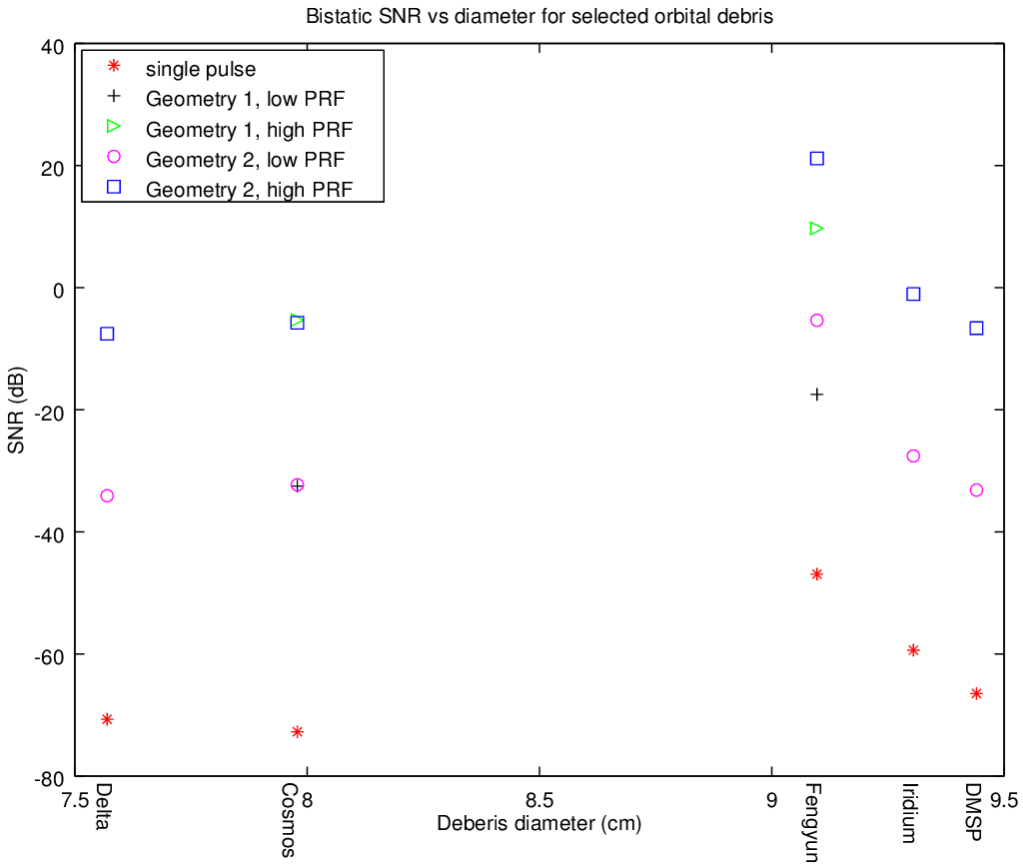

Figure 3.6: MeerKAT bistatic radar SNR vs diameter for the chosen orbital small debris for a single pulse ($*$) and the maximum number of pulses that can be realised for geometry 1, low PRF ($+$), geometry 1, high PRF ($\triangleright$), geometry 2, low PRF ($\circ$), geometry 2, high PRF ($\square$). Low PRF =150 Hz and high PRF = 75 kHz.

3.3 Range and Doppler ambiguity compensation

Range-Doppler processing collects fast-time ("ft") /slow-time ("st") data over the CPI and performs a slow-time DFT on all range bins to convert it to an range-Doppler matrix. It is assumed that the target velocity v_r, CPI duration T_{cpi}, and range bin spacing δR are chosen such that the target's range change

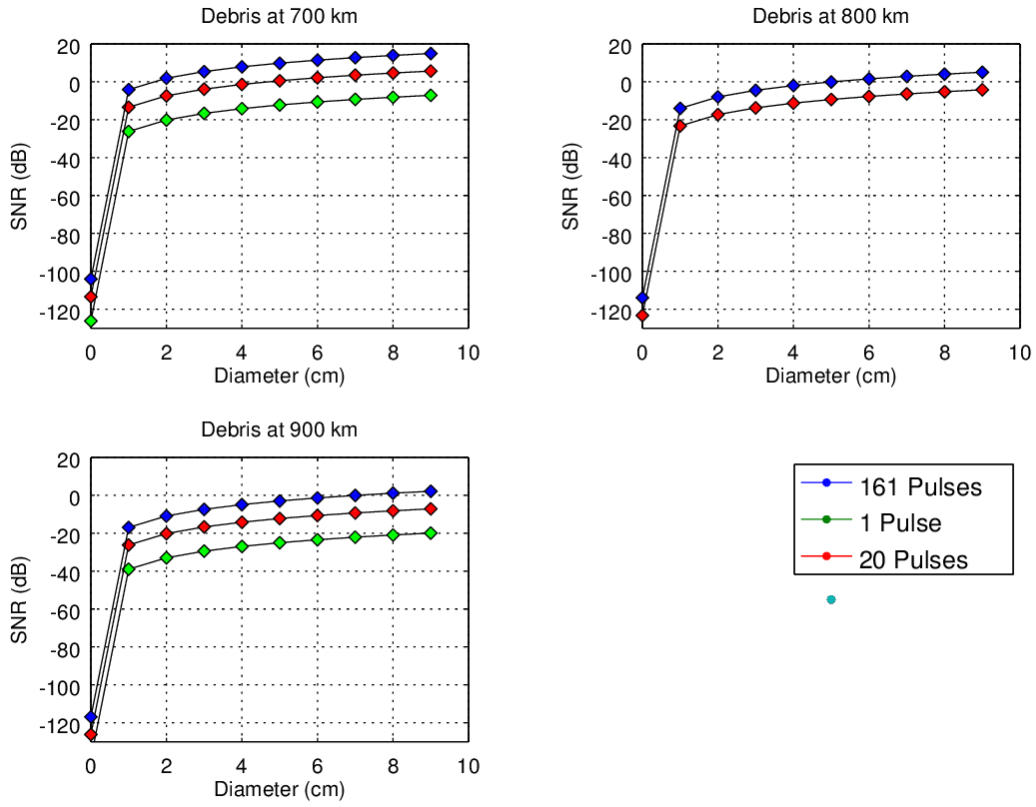

Figure 3.7: MeerKAT bistatic radar SNR vs diameter for the debris altitudes of 700 km, 800 km and 900 km. Coherent integration is considered for two cases of CIT limitations. $\diamond$ represents single pulse SNR, $\diamond$, 20 pulses for accelerating debris, low PRF radar and $\diamond$, 160 pulses for non-accelerating debris, high PRF radar

in the CPI is less than one range bin, $v_r T_{cpi} < \delta R$ (the target stays in the same range bin over the entire T_{cpi}). This means that all of the target signature will be in the same range bin and a 1D slow-time DFT will be a well-formed, fully resolved Doppler spectrum. For a constant-velocity target without slow-time windowing, this spectrum will be just an aliased sinc function in the Doppler coordinate with a Rayleigh width of $\approx 1/T_{cpi}$ Hz. In this section, we discuss the range migration problem and implement range shifting and the Keystone transform compensation methods.

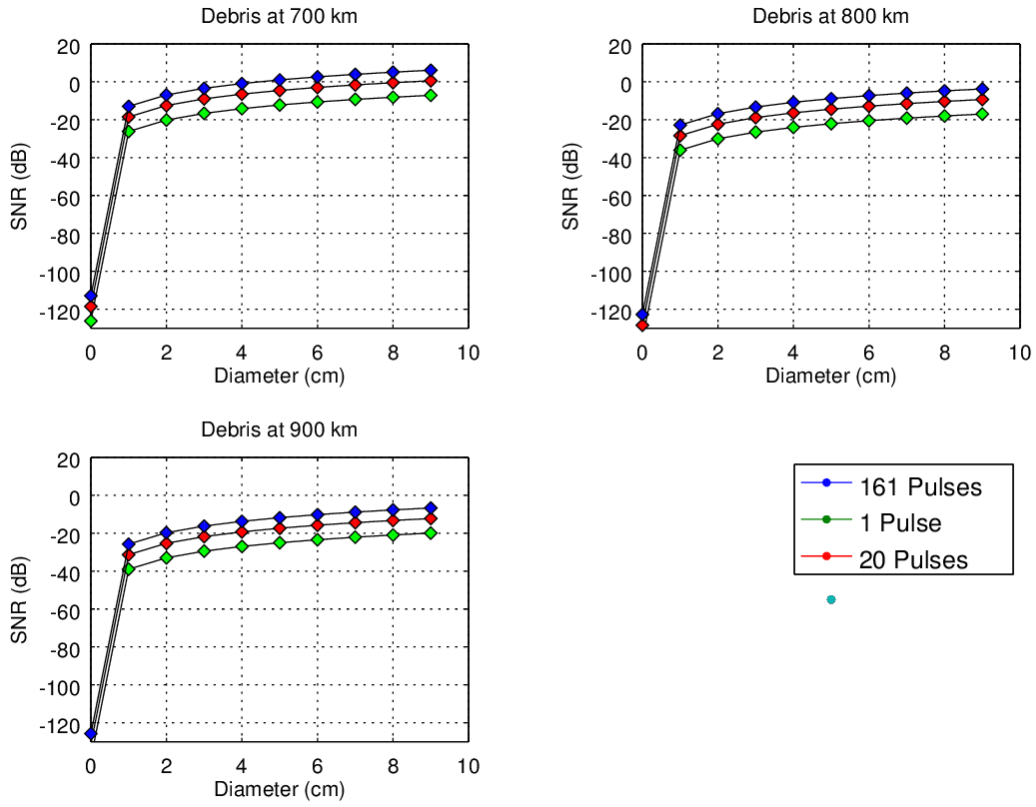

Figure 3.8: MeerKAT bistatic radar SNR vs diameter for the debris altitudes of 700 km, 800 km and 900 km. Non-coherent integration is considered for two cases of CIT limitations. ◇ represents single pulse SNR, ◇, 20 pulses for accelerating debris, low PRF radar and ◇, 160 pulses for non-accelerating debris, high PRF radar

Range migration occurs when the target does not remain within a single range bin over the CPI, and the target Doppler "smears" in both range and Doppler, because portions of the target signature appear in more than one range bin and any one range bin contains the signature for a portion of the CPI. These effects are more severe for high speed targets and wide-bandwidth (fine range resolution) systems.

The goal of the range migration compensation methods is to obtain the range-Doppler spectrum corresponding to a target's relative range and

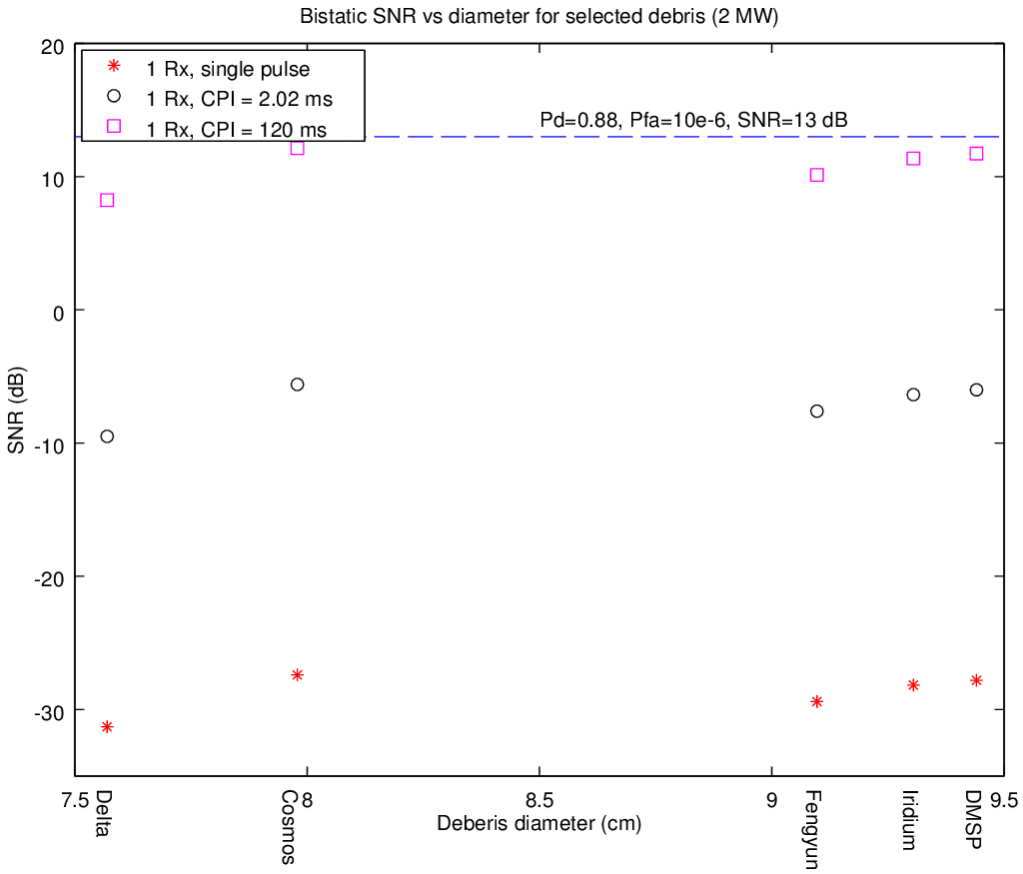

Figure 3.9: MeerKAT bistatic radar coherent SNR vs diameter for the chosen orbital small debris for a single pulse (∗), CPI of 2.02 ms for non-accelerating debris (o), CPI of 120 ms for accelerating debris (□).

normalised Doppler with full resolution in both dimensions as determined by the waveform bandwidth B and CPI. Even though range migration may be unavoidable as stated by Li in [91], there are a number of compensation algorithms including: Keystone, range-shifting, range- bin alignment, envelope interpolation, and time-frequency analysis, among other algorithms. In this analysis, we consider range shifting for non-accelerating single target detection and the Keystone transform for non-accelerating multiple target detection.These methods were chosen due to their computational efficiency, suitability to fast moving orbital debris, and applicability to a pulse-Doppler radar.

Suppose a radar transmits a pulse $\overline{x}$:

$$\overline{x}(t) = x(t)\exp(j2\pi f_c t) \tag{3.17}$$

where $x(t)$ is the LFM baseband waveform.

In an $L \times M$ ft-st matrix, a series of $M = 2M_{cpi} + 1$ transmitted pulses which are reflected from a target are sampled in slow time at T_{st} seconds (PRI). The CPI is in the range of $-T_{cpi}/2 = -M_{cpi}T_{st}$ to $+T_{cpi}/2 = +M_{cpi}T_{st}$ and the centre of the CPI is at $t = 0$ and $M = 0$. The fast-time sampling interval is T_{ft} and the range bin spacing is $cT_{ft}/2$.

Let's assume that the range corresponding to the first range bin ($l = 0$) is R_0 and R_{rel} is the reference range relative to R_0, then the target range at the centre of the CPI is $R_{ref} = R_0 + R_{rel}$. Let the range bin corresponding to R_{rel} be l_{rel}. Thus, $l_{rel} = (2R_{rel}/c)/T_{ft} = R_{rel}/\delta R$. The target range on the m_{th} pulse ($-M_{cpi} \leq m \leq M_{cpi}$) will be $R_{ref} + v_r T_{st} m = R_0 + R_{rel} - v_r T_{st} m$, corresponding to range bin $l_{rel} - 2v_r T_{st} m/cT_{ft} = l_{rel} - v_r T_{st} m/\delta R$. (The range bin number is rounded to the nearest integer.)

After taking out the delay of mT_{st} to the start of a pulse's transmission and demodulating the signal to baseband (by multiplication with the function $exp(-j2\pi f_c t)$ to remove the carrier), the received fast-time signal (ignoring amplitude terms) for the m^{th} pulse is of the form:

$$y_m(t) = x\left(t - \frac{2}{c}\Big(R_{ref} - v_r T_{st} m\Big)\right) exp\left[-j\frac{4\pi f_c}{c}(R_{ref} - v_r T_{st} m)\right] \tag{3.18}$$

The demodulated matched filter output is:

$$y_m(t) \approx \exp\left(-j\frac{4\pi f_c}{c}R_{ref}\right) exp\left(+j\frac{4\pi f_c}{c}v_r T_{st} m\right) \mathrm{sinc}\left(\mathrm{B}\left(\mathrm{t} - \frac{2}{\mathrm{c}}\Big(\mathrm{R_{ref}} - \mathrm{v_r T_{st} m}\Big)\right)\right) \tag{3.19}$$

The resulting continuous fast-time vector after taking samples at times $t = 2R_0/c + l.T_{ft}, l = 0, ...L-1$ from M pulses ($l_m = v_r T_{st} m/\delta R$) in the CPI are put in an ideal (no range migration) 2D ft/st matrix $y_{rd}(t, m]$:

$$y_{rd-ideal}(t, m] = \exp\left(-j\frac{4\pi f_c}{c}R_{ref}\right)exp\left(+j\frac{4\pi f_c}{c}v_r T_{st} m\right)\text{sinc}\left(\text{B}\left(\text{t}-\frac{2}{\text{c}}\left(\text{R}_{\text{ref}}\right)\right)\right) \tag{3.20}$$

Computing the Fourier transform (FT) of Equation 3.20 in fast-time results in the fast-time baseband frequency F and velocity v being uncoupled (as shown in 3.21). The range migration methods aim to manipulate the actual data to be of the form of the ideal 3.20, where the corresponding range-Doppler spectrum is correctly centred and well focussed.

$$Y_{Rd-ideal}(F, m] = \begin{cases} exp\left(-j\frac{4\pi}{c}(F+f_c)R_{ref}\right)exp\left(+j\frac{4\pi}{c}f_c v_r T_{st} m\right), & \\ -B/2 < F < +B/2, \quad -M_{cpi} < m < +M_{cpi} & \\ 0, \qquad\qquad\qquad\qquad \text{otherwise} & \end{cases} \tag{3.21}$$

In practice, the Fourier transform of the actual fast-time signal (3.22) gives frequency and velocity that are not separable, but instead are coupled in the slow-time phase term. At frequencies greater than f_c ($F > 0$) the sample-to-sample slow-time phase progression rate is faster than the desired value of $f_c v_r T_{st}$, while at frequencies lower than f_c ($F < 0$) it is slower than desired.

$$Fy_m(t) = Y_{Rd}(F, m] = \exp\left(-j\frac{4\pi}{c}(F+f_c)R_{ref}\right)exp\left(+j\frac{4\pi}{c}(f_c+F)v_r T_{st} m\right) \tag{3.22}$$

3.3.1 Compensation by Range Shifting

A target with known radial velocity moves $v_r T_{st}/\delta R$ rage bins closer to the radar on each successive pulse. Range shifting corrects each successive fast-time vector by $-v_r T_{st}/\delta R$ bins with respect to the previous data. The reference range (R_{ref}) to which all target echoes will be shifted relative to the first range bin (R_0) is chosen to correspond to the target range [92].

This method is only suitable for cataloged space debris and asteroids whose orbital parameters are known from measurements and orbital mechanics. Range shifting is implemented by multiplying $Y_{Rd}(F, m]$ by the phase term $\exp(-j\frac{4\pi}{c}F v_r T_{st} m)$. Figure 3.10 shows the application of range shifting on Fengyun-1C debris and the MeerKAT bistatic radar parameters.

3.3.2 Keystone transformation

The "Keystone" transform aims to remove the frequency-velocity coupling by resampling the fast-time slow-time data. This method is suitable for range migration correction in multiple targets of various known or unknown velocities [93].

The Keystone transform is applied on the slow-time term, since that is where the coupling occurs. Sampling $Y_{Rd}(F, m]$ in slow-time at times $\tau_m = m.T_{st} - M_{cpi} \leq m \leq M_{cpi}$ where $M = 2M_{cpi} + 1$, gives:

$$Y_{Rd}(F, \tau] = \begin{cases} exp\Big(- j\frac{4\pi}{c}(F + f_c)R_{ref} \Big) exp\Big(+ j\frac{4\pi}{c}(F + f_c)v_r\tau \Big), \\ -B/2 < F < +B/2, -M_{cpi}T_{st} < \tau < +M_{cpi}T_{st} \end{cases} \tag{3.23}$$

Defining a new slow-time variable $\tau' = \left(\frac{f_c+F}{f_c}\right)\tau$ that rescales the slow-time axis as a function of fast-time frequency $\tau = \left(\frac{f_c}{f_c+F}\right)\tau'$ and substituting in 3.23 gives

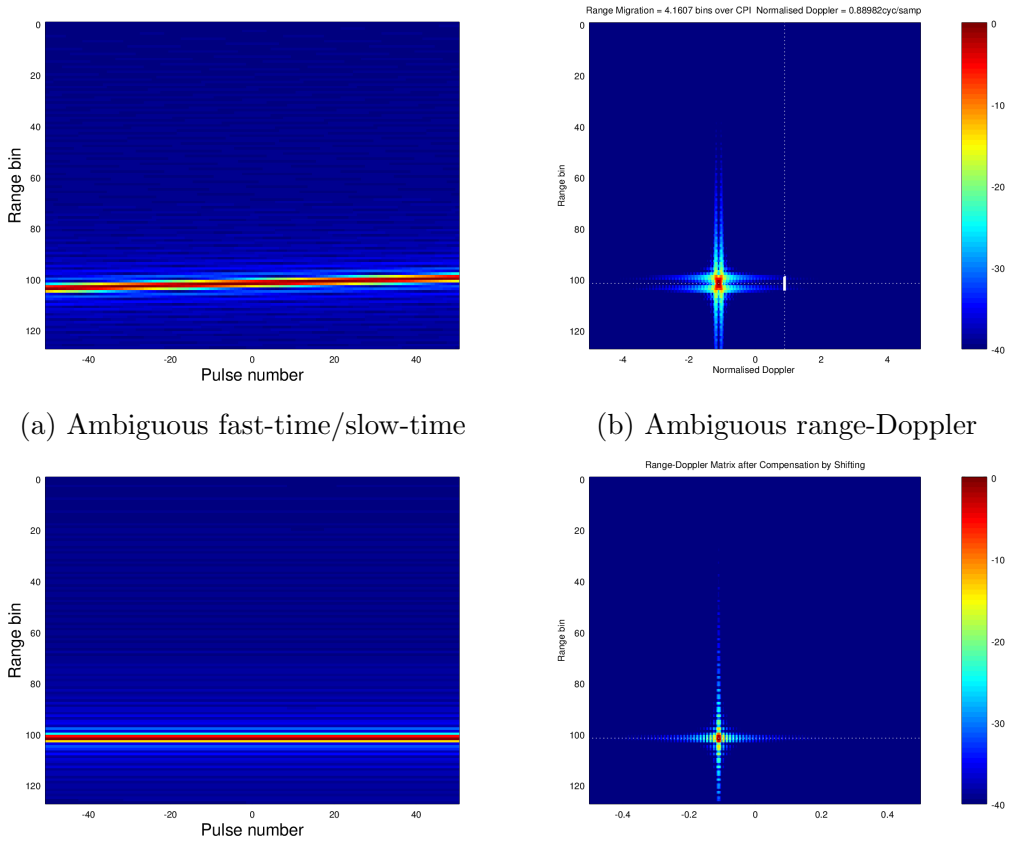

(a) Ambiguous fast-time/slow-time

(b) Ambiguous range-Doppler

(c) Shifted fast-time/slow-time

(d) Shifted range-Doppler

Figure 3.10: Fast-time/slow-time data for Fengyun-1C debris at R=885 km , v=7.41 km/s and a=0 m/s^2, showing range migration across 2.6511 range bins due to the small range bin size of 6 m (a and b) and no range migration and fine Doppler resolution after range shifting (c and d). Doppler frequency = 66690 Hz, normalised Doppler frequency= 0.88920 cycles/sample, wrapping to -0.11080 cycles/sample.

the Keystone transform function 3.24. For $F > 0$ this will have a stretching effect of the sample to sample phase progression over a longer time interval, thereby reducing the time rate of phase change and therefore the slow-time frequency.

For $F < 0$ the slow-time frequency will be increased in the rescaled data. An IFT in the range dimension and a forward FT in the pulse number dimension will result in the focused range-Doppler image with no degradation due to range migration as illustrated for small debris in Figure 3.11.

$$Y_{Rd-Key}(F,\tau'] = Y_{Rd}(F,\left(\frac{f_c}{f_c+F}\right)\tau] = exp\left(-j\frac{4\pi}{c}(F+f_c)R_{ref}\right)exp\left(+j\frac{4\pi}{c}v_r f_c\tau'\right) \tag{3.24}$$

The range shifting method removed range migration for a single debris target and the Keystone transform compensated for range migration for multiple debris targets successfully. Consequently, the Doppler resolution improved in both cases after range migration compensation.

3.4 MeerKAT bistatic radar PHA detection

Three asteroids; 2015 BN50g, 2010 NY65, 1998 SL36, were chosen to represent the 1736 PHAs that are known as of 2017. Predicted physical parameters for their close pass to Earth were obtained from the NASA and ESA websites and used to perform a theoretical analysis and simulations. Asteroids are heliocentric, but the online minor planets visibility tool allows one to choose the centre of their motion. In order for the orbital mechanics to be similar to the ones used for orbital debris, we transform the asteroids to be geocentric. This makes the parameters needed for the simulation easy to generate.

Some of the asteroid physical parameters and technical terms used include:

- Absolute magnitude: the magnitude of an asteroid at zero phase angle and at unit heliocentric and geocentric distances

- Astronomical Unit: the mean distance between the Earth and the Sun. In 2012, the International Astronomical Union defined the distance to be 1.496e+8 km.
- Albedo: the ratio of the light reflected by a body to the light received by it. Albedo values range from 0 (pitch black) to 1 (perfect reflector).
- Geometric albedo: the ratio of a body's brightness at zero phase angle to the brightness of a perfectly diffusing disk with the same position and apparent size as the body (0.25 to 0.05 for asteroids).

The diameter (D_{pha}) of an asteroid can be estimated from the absolute magnitude (H) and geometric albedo (p) as:

$$D_{pha} = \frac{1329}{\sqrt{p}} 10^{-0.2H} \tag{3.25}$$

Table 3.6 show the predicted Earth and asteroid orbits for when the chosen PHAs will pass "very" close to Earth in 2017 and their physical parameters.

Table 3.6: Table of PHAs physical parameters for the predicted close passes to Earth on Feb. 7th 2017 at 21:31 (asteroid 2015 BN50g), June 24th 2017 at 06:38 (asteroid 2010 NY65) and March 16th 2017 at 13:32 (asteroid 1998 SL36).

PHA	R(AU)	R(km)	v_r (km/s)	H(mag)	Albedo	D_{pha}(km)
2015 BN50g	5.01e-5	91e3	19.4	20.6	0.046	0.470
2010 NY65	0.00049	73e3	12.7	21.5	0.071	0.249
1998 SL36	0.00036	54e3	14.8	22.3	0.08	0.162

Because of the large distance at which the asteroids orbit, the geometry approximates a quasi-monostatic radar. The 2μs pulse that we used for debris is insufficient and a longer pulse ($\approx$ 30μs) is required. This can be effectively achieved by transmitting phase codes. Barker codes of length 13 are considered, increasing the pulse width and improving the SNR as shown in Figure 3.12, is not sufficient in the bistatic mode and more receivers need to be used. Only the

coherent case was considered in asteroid detection since the non-coherent case yielded an undesirably low SNR.

Figure 3.13 shows the asteroid range migration problem due to the "very" high orbital speed. To reduce the range walk, the sampling frequency was reduced to half the bandwidth since PHAs may not orbit close to each other as is the case with orbital debris. Table 3.7 shows that there was a significant decrease in the number of range bins traversed by the target when the sampling frequency is made equal to (and half) bandwidth to an acceptable level.

Table 3.7: Table of range bins migrated by the asteroids and how the numbers reduce with a reduction in f_s.

f_s	2015 BN50g	2010 NY65	1998 SL36
25 MHz	69.4089	45.4378	52.9511
10 MHz	27.7636	18.1751	21.1804
10 MHz	27.7636	18.1751	21.1804
5 MHz	13.8818	9.0876	10.5902

In this section, the asteroid parameters were given for selected objects that were predicted to make a close pass to Earth in 2017. Using the 2 MW transmitter, coherent SNR for the quasi-monostatic geometry was calculated. Due to the large unambiguous range required, a long pulse was implemented using Barker codes of length 13. The maximum SNR obtained from this set up was 26 dB. Implementing range migration compensation showed that there was a large number of range bins being traversed by the asteroids and range migration was not fully compensated for. Since asteroids do not orbit close to one another in the order of meters, the range bin size was increased by decreasing the signal bandwidth to 5 MHz. This lead to significant reduction in range migration by 80%.

3.5 MeerKAT bistatic radar simulations

Using FERS (Flexible Extensible Radar Simulator), simulations were done for radar parameters in Table 3.1 and small space debris whose parameters are in Table 3.2. Two geometries shown in Figure 3.5 are considered and the simulation duration was limited to the CPI because theory showed that the non-coherent SNR was too low for detection using the bistatic mode. Limiting the dwell time to the CPI also minimises the effect of range-Doppler ambiguities. All targets were considered to be Swerling case 1 at this stage.

Due to the large range and target velocities, a multiple PRF system is proposed, such that a basic PRF (PRF_b) can give an unambiguous range and the high PRF, an unambiguous Doppler frequency. However, since the radar simulator used in this analysis does not yet have multiple PRF capability, the simulations are done for a high PRF and the ambiguities are explained. In the cases where a considerable amount of range migration persisted, the simulation time is then further limited to the number of pulses within a single range bin.

In a real world, a multiple PRF radar implements the Chinese remainder theory to obtain range and range rate with a high PRF. We assume a two PRF system with a basic PRF of 150 Hz for an unambiguous range of 1000 km and we choose an integer 499, such that $\mathrm{PRF}_1 = \mathrm{N}\ \mathrm{PRF}_b = 74850$ Hz and $\mathrm{PRF}_2 = (N+1)\mathrm{PRF}_b = 75000$ Hz. N and $N+1$ are relative prime numbers. It is possible to use a third PRF to increase the unambiguous range, with increased computational requirements. The average of PRF_1 and PRF_2 is used in the simulations.

Since known target range and velocities are "fed" to the simulator, it is sufficient to compensate for range migration by adjusting the start of the fast-time sampling times for each successive pulse, so that the target remains in a constant delay relative to the transmission time for the current pulse.

3.5.1 FERS radar simulator

FERS is an open source radar simulator that allows radar engineers to explore the radar system design space, both qualitatively and quantitatively. Its applications include: netted, pulse-Doppler, airborne, electronic warfare and continuous wave, MIMO, FMCW radar systems. In using FERS, one can chose a transmit waveform, system geometry, bandwidth and numbers of targets, transmitters and receivers.

Target, transmitter and receiver platforms can be modelled as stationary or moving, with a motion profile that is either linear or cubic. Azimuth and elevation extents for the transmitter, receiver and target platforms are taken into consideration. For the case of a search radar, the rate of change of azimuth and elevation is added to the simulation specifications. Signal processing of the simulated data is done independent of the simulator and in this work, it was done using software written Octave.

The FERS simulator program consists of three independent software elements: the environment model (propagation environment), the signal renderer (specifies transmit signal) and extension modules as shown in Figure 3.14. The simulation environment is defined using the extensible mark-up language (xml) and the generated simulated data can be in the form of: .csv, .xml and HDF5. More details on the use of FERS can be found in [94]. The transmit signal is generated externally and input as an HDF5 file. Perfect synchronisation is assumed and the simulator records the reference signal to be used in post processing. A flow chart summarising the post-processing is shown in Figure 3.15.

The use of phase codes in simulating asteroids was used to mimic Swerling case 2 by diving the transmitted pulses into bursts of equal length, then processing each burst coherently, but non-coherently from burst to burst. This effectively mimics Swerling case 1 in a single burst, and Swerling case 2 from burst to burst. Figure 4.18 shows the delay-Doppler plots for the simulated data indicating the correlation of the debris delay and Doppler matching the values calculated in theory.

This section tackled the radar simulator, signal processing and the generation of ARD plots for both debris and PHAs. The bistatic simulation using the high power transmitter, showed that coherent detection for non-accelerating targets is possible, but with a low SNR. Figure 4.18 shows that range shifting removes range migration from up to only 80% when the range bin size is increased from 6 m to 30 m. Figure 3.17 shows the deviation of theoretical calculations from simulated results. These errors were validated by simulating radars of varying parameters and comparing the obtained simulated data with theory to 4 significant figures. The values obtained from the simulator and theory tally up to 4 significant figures, but vary slightly beyond that, due to different modes of calculating and rounding off.

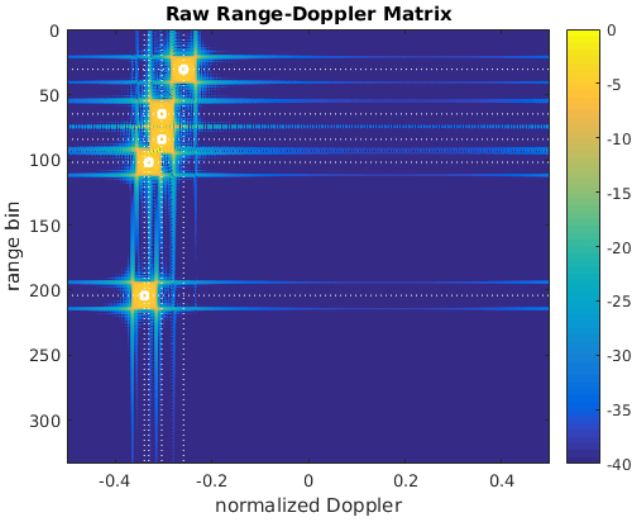

(a) Ambiguous range-Doppler

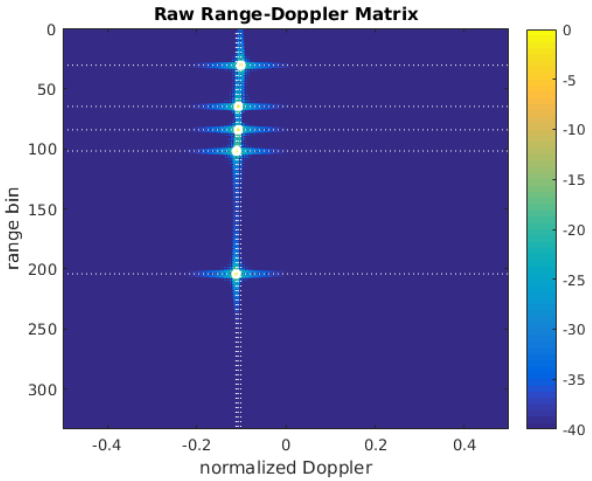

(b) Keystone corrected range-Doppler

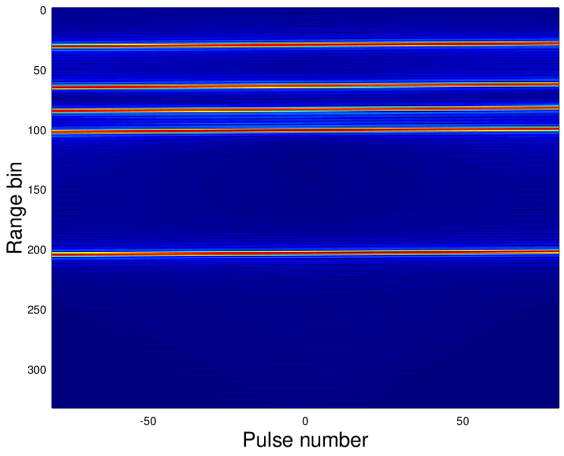

(c) Range migration for debris

Figure 3.11: Debris: Fengyun-1C, Iridium 33, Cosmos 2251, Delta 1, and DMSP-F11 at wrapped normalised Doppler frequencies of: -0.11080 -0.10720 -0.10120 -0.11200 -0.10720 cycles/sample, respectively. The number of range bins migrated are: 2.6511, 2.6619, 2.6798, 2.6476, 2.6619, respectively and zero after the Keystone compensation.

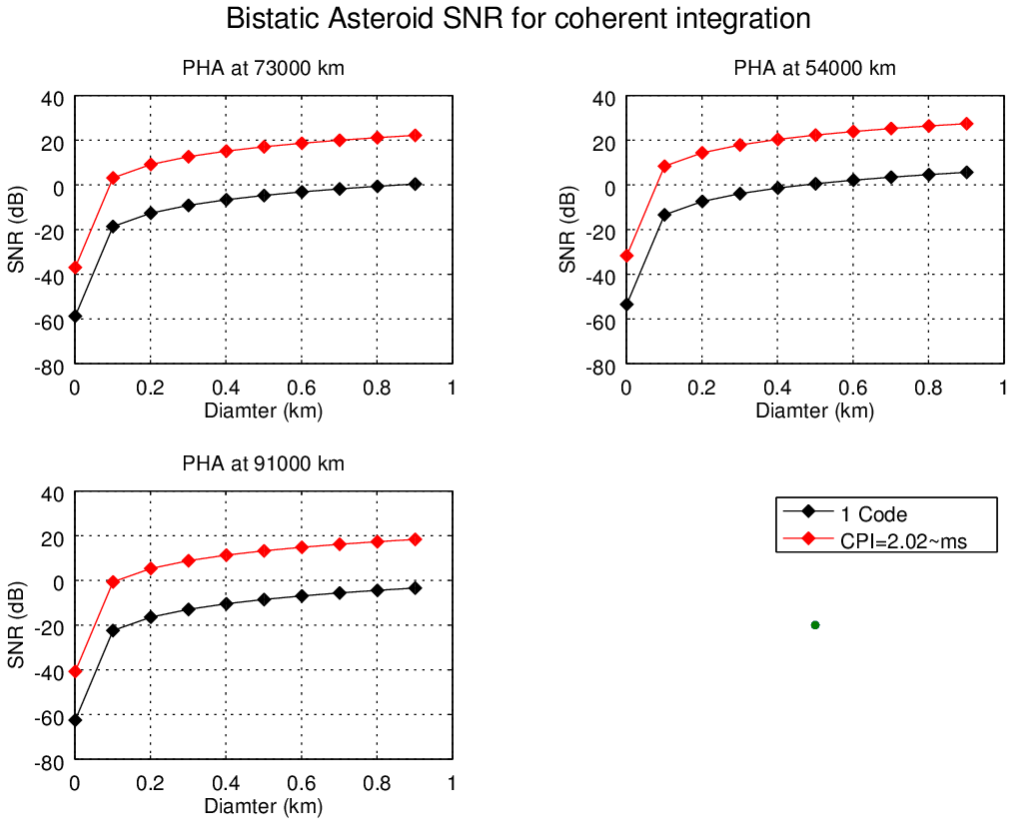

Figure 3.12: SNR for asteroids 2015 BN50g, 2010 NY65 and 1998 SL36, at 50,000 km, 70,000 km and 90,000 km for 1 pulse(◇), 13 Barker codes for geometry 1 (◇) and 13 Barker codes for geometry 2 (◇).

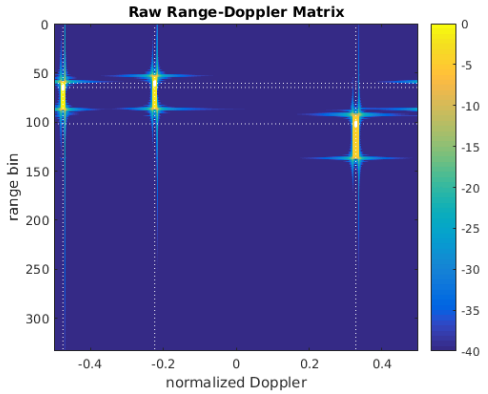

(a) f_s=25 MHz

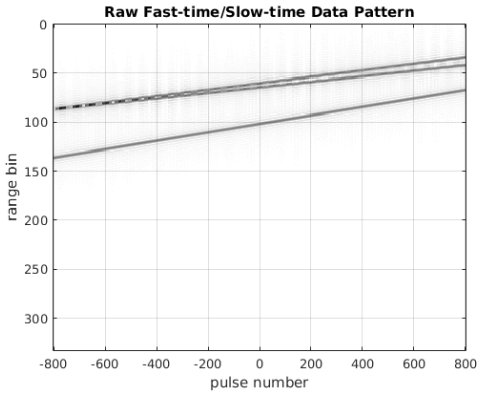

(b) f_s=25 MHz

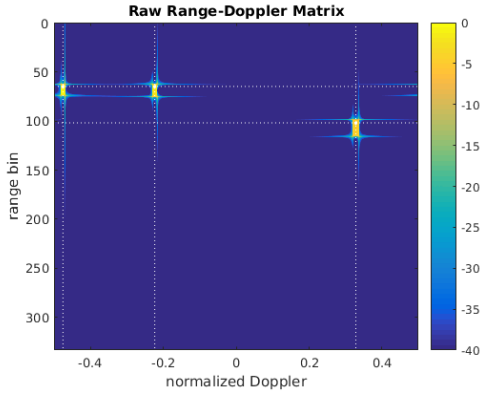

(c) f_s=12.5 MHz

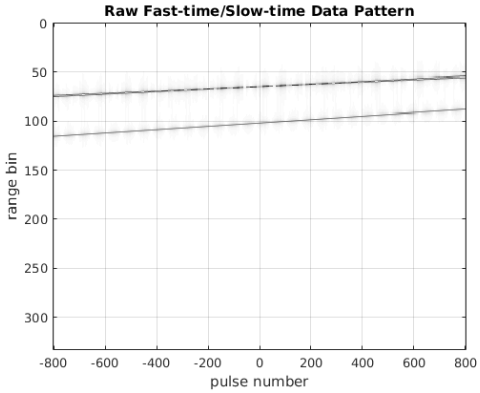

(d) f_s=12.5 MHz

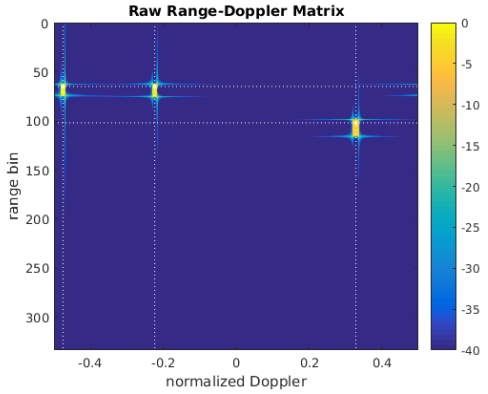

(e) f_s=5 MHz

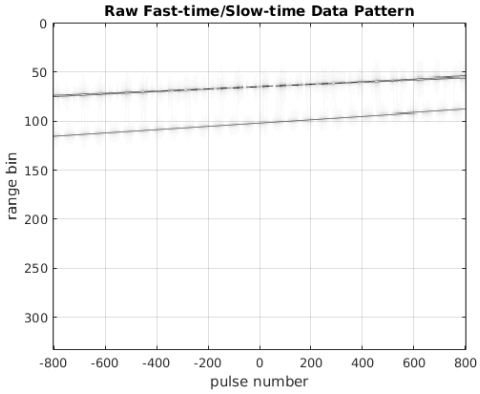

(f) f_s=5 MHz

Figure 3.13: Range-Doppler plot for 3 representative potentially hazardous asteroids: 2015 BN50g, 2010 NY65 and 1998 SL36. The ambiguous normalised Doppler frequency is: 0.3280, -0.4760 , -0.2240, respectively. The number of range bins migrated decrease with a decrease in slow-time rate, but even when the slow-time is decreased by a quarter, there is still an acceptable range migration.

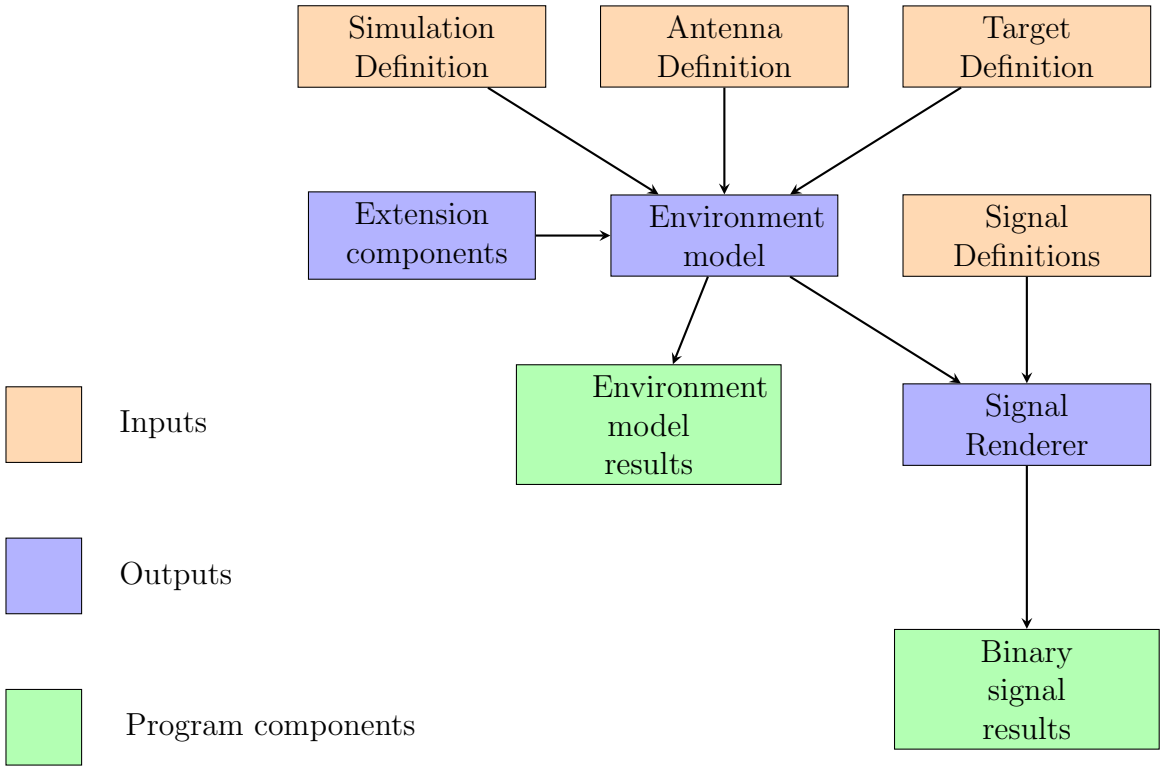

Figure 3.14: The FERS radar simulator sub-systems showing inputs, outputs and program components. In the inputs, the simulation is defined and named, the transmit waveform is "called" from an external file, the transmit/receive antennas are defined and the target parameters are given. The program then "creates" an environment model and simulates the transmission/reception process, and then outputs simulated data in a pre-specified format.

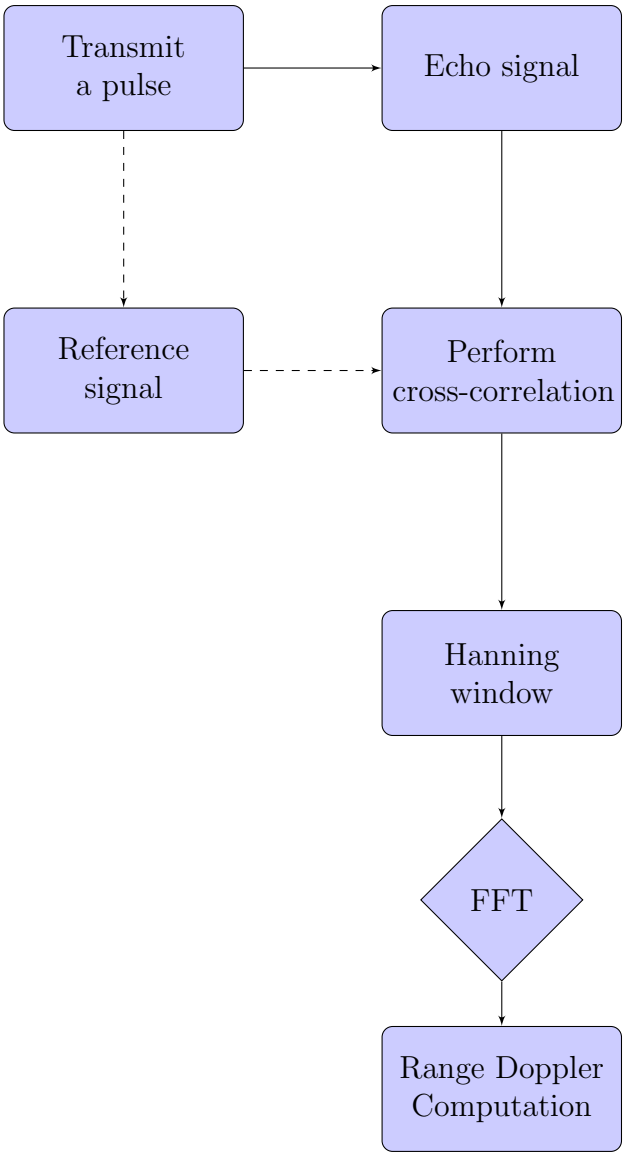

Figure 3.15: Flow chart summarising the post processing of FERS simulated data, showing matched filtering, windowing and range-Doppler computation. The reference signal is generated by the radar simulator. All data was in HDF5 format and the processing was done in the Octave language.

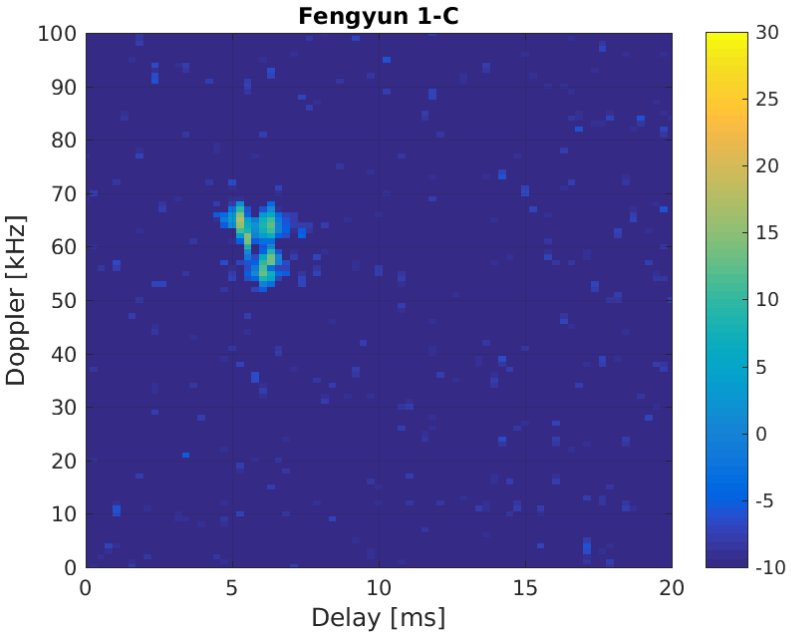

(a) All debris: Bistatic coherent with transmit power of 2 MW

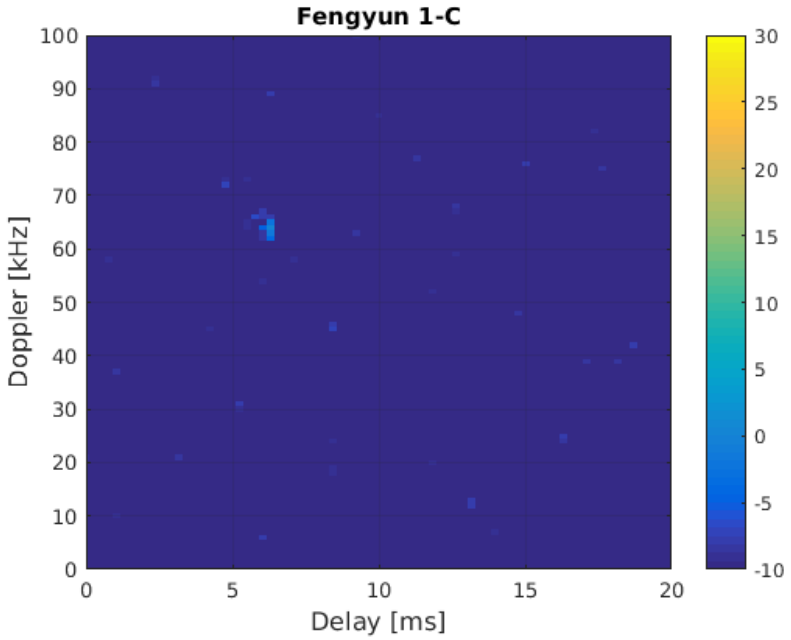

(b) Fengyun: Bistatic coherent with transmit power of 10 kW

Figure 3.16: Simulated delay-Doppler map for all debris for the bistatic, geometry for both coherent and non-coherent processing.

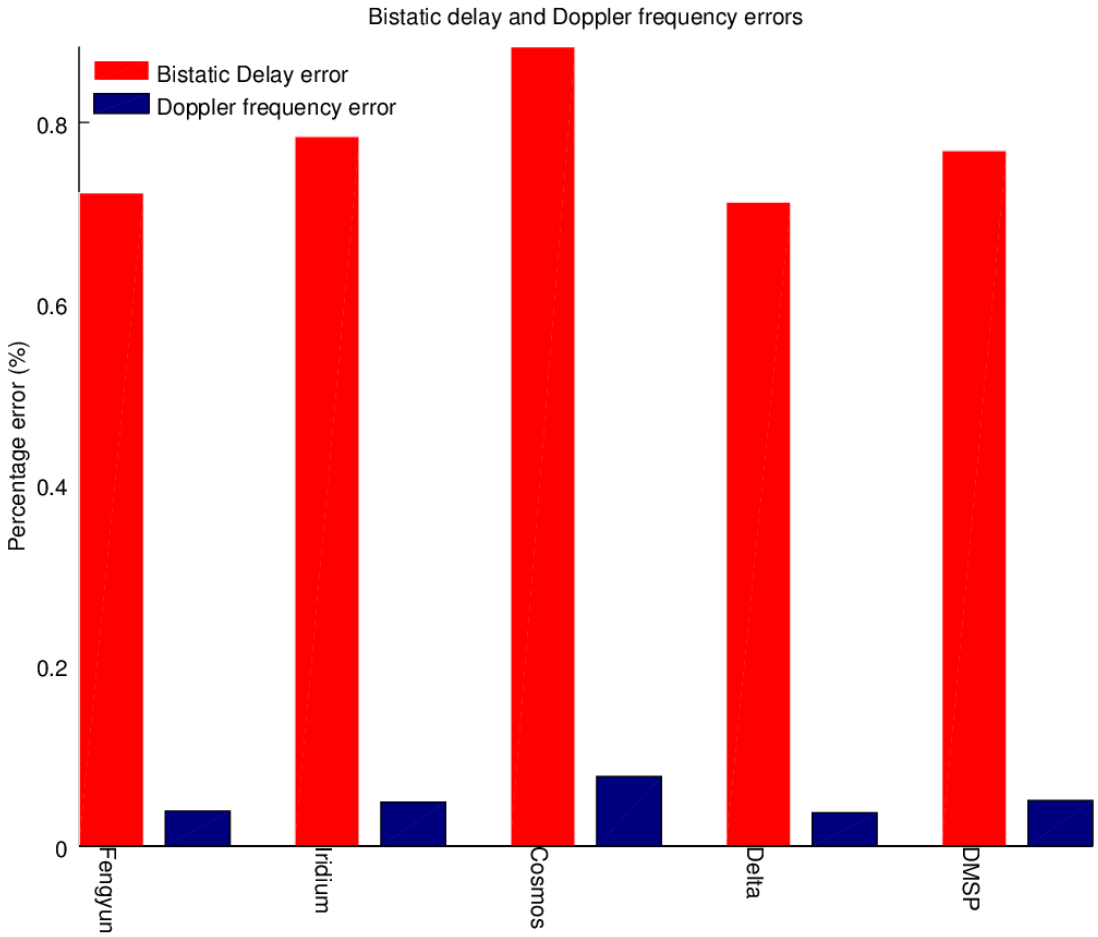

Figure 3.17: Percentage deviation of theoretical bistatic delay and aliased normalised Doppler frequency from simulations for the 5 debris objects. The maximum error for Doppler frequency is 0.076% while that for delay is 0.88% and the error seem to correlate in variation for both Doppler frequency and delay. Note that the simulated and theoretical values match up to 4 significant figures and these deviations are from 5 to 7 significant figures.

3.6 Conclusion

From theory, it was found that the maximum coherent SNR for the MeerKAT bistatic radar was higher that the non-coherent integration by 7 dB for the maximum number of pulses for geometries 1 and 2. Therefore, in simulations, only coherent integration was considered and the simulation duration was limited to the CIT limitation (2.02 ms) for non-accelerating targets.

Using range shifting, range migration was compensated for in the FERS simulation of the Fengyun1-C debris. From geometry, accelerating targets have the largest CIT leading to better Doppler resolution compared to non-accelerating targets. Geometry 2 and high PRF gave the nearest to optimal mode of detection. Comparison of theory with simulations shows deviations in bistatic delay and aliased normalised Doppler frequency.

For asteroids, the quasi-monostatic set up, using phase codes, is not sufficient to detect objects with a positive SNR. More receivers need to be used in order to obtain meaningful NEA detections. The range walk is worse for asteroids due to their high speed, and both the range shifting and Keystone transform were unable to completely remove the range migration. One of the solutions to this problem is severely undersampling the asteroid data so as to increase the range bin size significantly.

In conclusion, it is only suitable to use the bistatic configuration for the MeerKAT radar using a high power transmitter and geometry 2 which considers the maximum receiver azimuth and elevation. Coherent processing for accelerating targets gives the largest dwell time and hence the most coherent integration gain. Coherent integration for non-accelerating targets and non-coherent integration do not give sufficient SNR increase for a probability of detection of at least 88 % and probability of false alarm of 1e-6. It is necessary to increase the SNR further by using more than one receiver. However, the purpose of proof of concept was achieved by showing the suitability of the transmitter site and the radar geometry for small debris and PHAs monitoring.

Deviation of theory from simulations was a result of simplifying assumptions in the simulator and rounding off in the signal processing algorithm. The results from theory and simulations match up to 4 significant figures.

In the next chapter, the multistatic configuration is discussed where the radar uses more than one MeerKAT antenna for reception. The antennas are divided into inner, middle and outer circular sub-arrays and evaluated together and separately. The SIMO radar geometry is compared to the conventional multistatic radar, in terms of performance and computational efficiency.

Chapter 4: MeerKAT multistatic configuration

The MeerKAT multistatic and SIMO radar configurations are discussed in this chapter. The signal models and assumptions made for each set-up are given, then simulations are compared to what is theoretically expected in terms of detection capability, suitability to the receiver DBE and computational requirements. Multi-beam tracking is discussed using three concentric circular sub-arrays in the SIMO configuration. A summary of the ISAR technique used to illustrate the imaging capability of the MeerKAT 3D radar and results are given. Then an analyses the range, velocity and angular radar measurement errors, and how these errors propagate to orbital period and inclination prediction is done.

4.1 Multistatic radar analysis

The MeerKAT multistatic radar consists of one transmitter and 64 receivers with overlapping coverage and combining target returns at a central location. Each transmitter-receiver baseline is modelled as a bistatic radar and all baselines combined make the multistatic radar. Signal synchronisation and spatial coherence among receiving elements is assumed.

Using the bistatic dwell time, the total time for which the target will reman in the field of view of the 64 receivers is calculated and plotted in Figure 4.1. The 5 representative debris targets show that the maximum multistatic dwell time

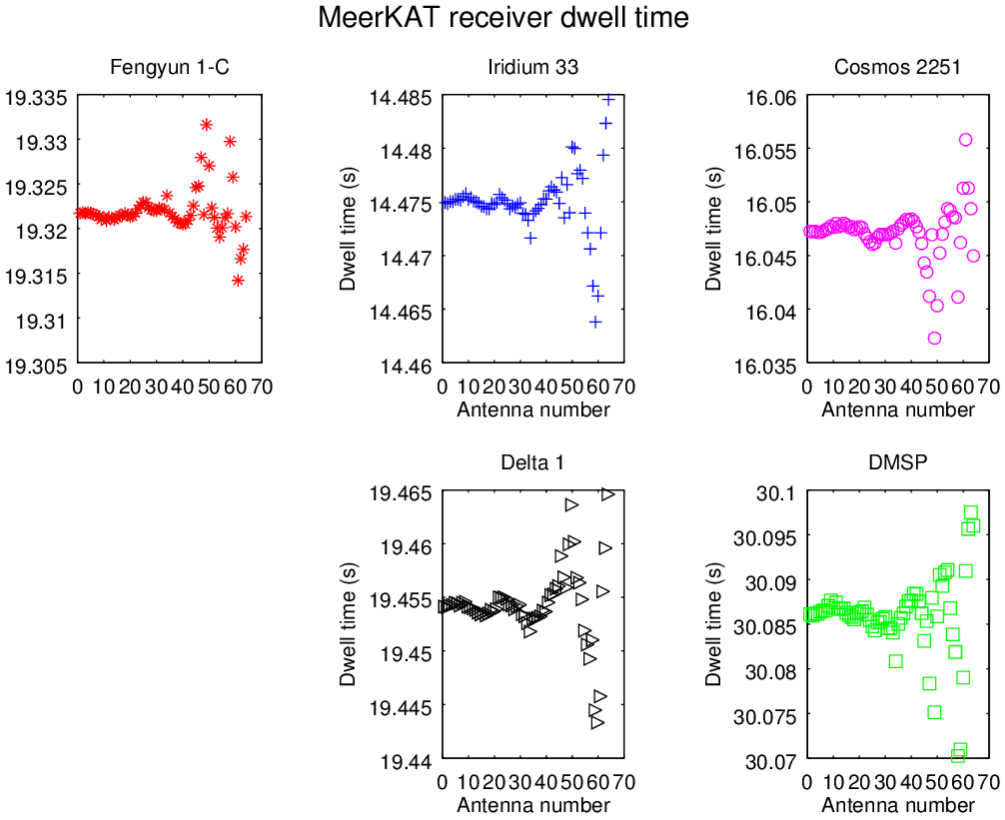

Figure 4.1: Geometric multistatic dwell time for each of the 5 representative orbital debris from 1 transmitter to the 64 MeerKAT receivers. Dwell time varies with target altitude, transmitter/receiver antenna azimuth and elevation. The maximum dwell time is 30 s and the minimum dwell time is 14 s.

variation is low for the inner "compact" receivers and increases with increasing baseline. The maximum dwell time is 30.1 s and the minimum dwell time is 14.5 s, corresponding to the minimum and maximum target altitudes, respectively. The multistatic radar equation for one transmitter and i receivers when the target is located in the line of sight of each bistatic plane is give by [95, 67]:

$$P_{Ri} = \frac{P_T G_T G_{Ri} \lambda^2 \sigma_B}{(4\pi)^3 R_T^2 R_{Ri}^2 l_T L_{Ri}}, i = 1, 2, ..., n \tag{4.1}$$

where, P_T is the transmit peak power G_T is the transmit antenna gain, G_R is

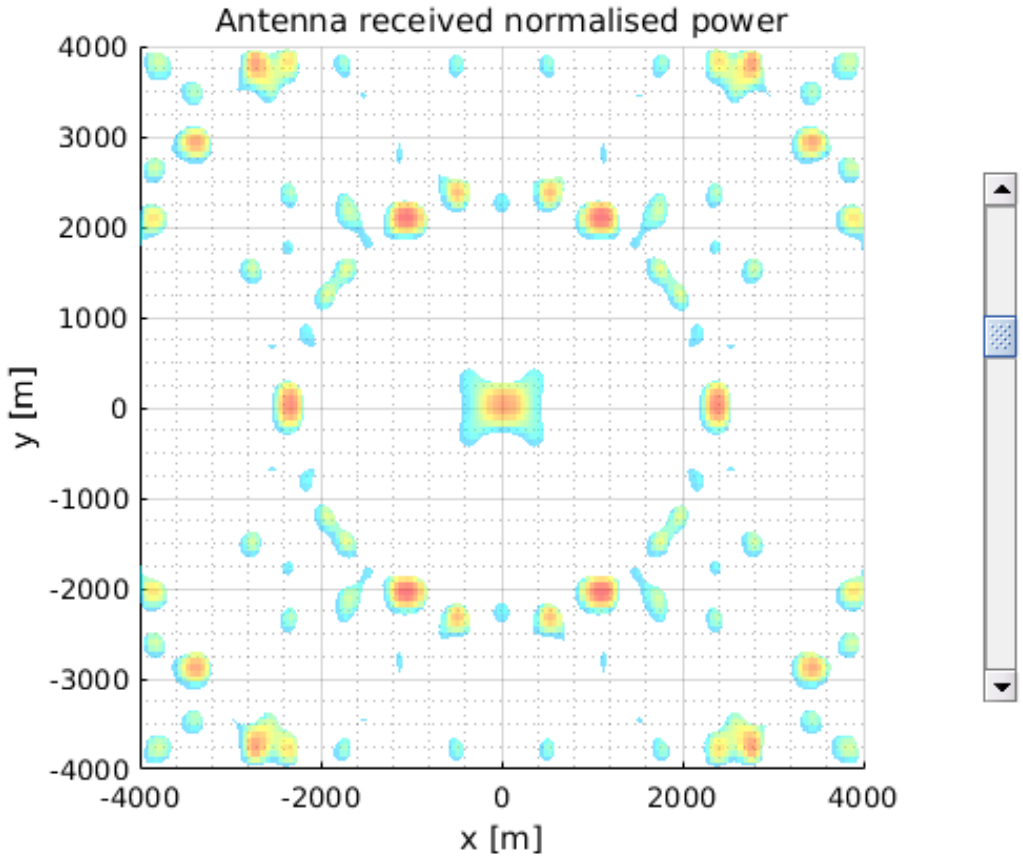

Figure 4.2: Multistatic receiver main beam distribution showing the received power for the Fengyun1-C debris at the 64 antennas. The received power is concentrated in areas where receive antennas are closely spaced, and the circular placement of antennas at 500 m, 4 km and 8 km from the centre of the array is shown.

the receiver antenna gain, B is the bandwidth, L_T is the transmit antenna loss, L_R is the receiver loss, λ is the wavelength, σ is the target's RCS, R_T is the distance from the transmitter to the target, R_R is the distance from the target to the receiver and n is the number of receivers [96, 97].

As in the bistatic radar geometry, the target range, angle of arrival θ_T and the bisector β, can be estimated from the measured two way delay ($R_T + R_R = c\delta T$)

using [98]:

$$R_T = \frac{(R_T + R_{Ri})^2 - L_i^2}{2\Big[R_T + R_{Ri} - L_i \sin(\theta_{Ti})\Big]}, i = 1, 2, ..., n \tag{4.2}$$

$$R_{Ri} = \Big[R_T^2 L_i - 2R_T L_i \sin(\theta_{Ti})\Big]^{\frac{1}{2}}, i = 1, 2, ..., n \tag{4.3}$$

$$\beta_i = \sin^{-1}\left[\frac{L_i \cos(\theta_{Ti})}{R_{Ri}}\right], i = 1, 2, ..., n \tag{4.4}$$

The target position in ENU Cartesian coordinates (x, y, z) can be obtained from the transmitter location (x_T, y_T, z_T) and the i^{th} receiver location (x_R, y_R, z_R) using:

$$R_T = \Big[(x - x_T)^2 + (y - y_T)^2 (z - z_T)^2\Big]^{\frac{1}{2}} \tag{4.5}$$

$$R_{Ri} = \Big[(x - x_{Ri})^2 + (y - y_{Ri})^2 (z - z_{Ri})^2\Big]^{\frac{1}{2}}, i = 1, 2, ..., n \tag{4.6}$$

The multistatic Doppler frequency for a target moving with radial velocity (v_{ri}) relative to the i^{th} receiver at an aspect angle of Δ_i, is given by:

$$f_{Di} = \frac{1}{\lambda}\Big[\frac{dR_T}{dt} + \frac{dR_{Ri}}{dt}\Big], i = 1, 2, ..., n \tag{4.7}$$

$$f_{Di} = \Big[\frac{2v_{ri}}{\lambda}\Big] \cos(\phi_i) \cos(\beta_i/2), i = 1, 2, ..., n \tag{4.8}$$

For n_t identical transmitting elements each with gain of G_t and n_r identical receiving elements each with gain of G_r, the multistatic SNR is given by:

$$SNR = \frac{n_T n_R P_T G_T G_R \sigma_b F_T^2 F_R^2}{(4\pi)^2 R_T^2 R_{Ri}^2 k T_n B L_T L_R} \tag{4.9}$$

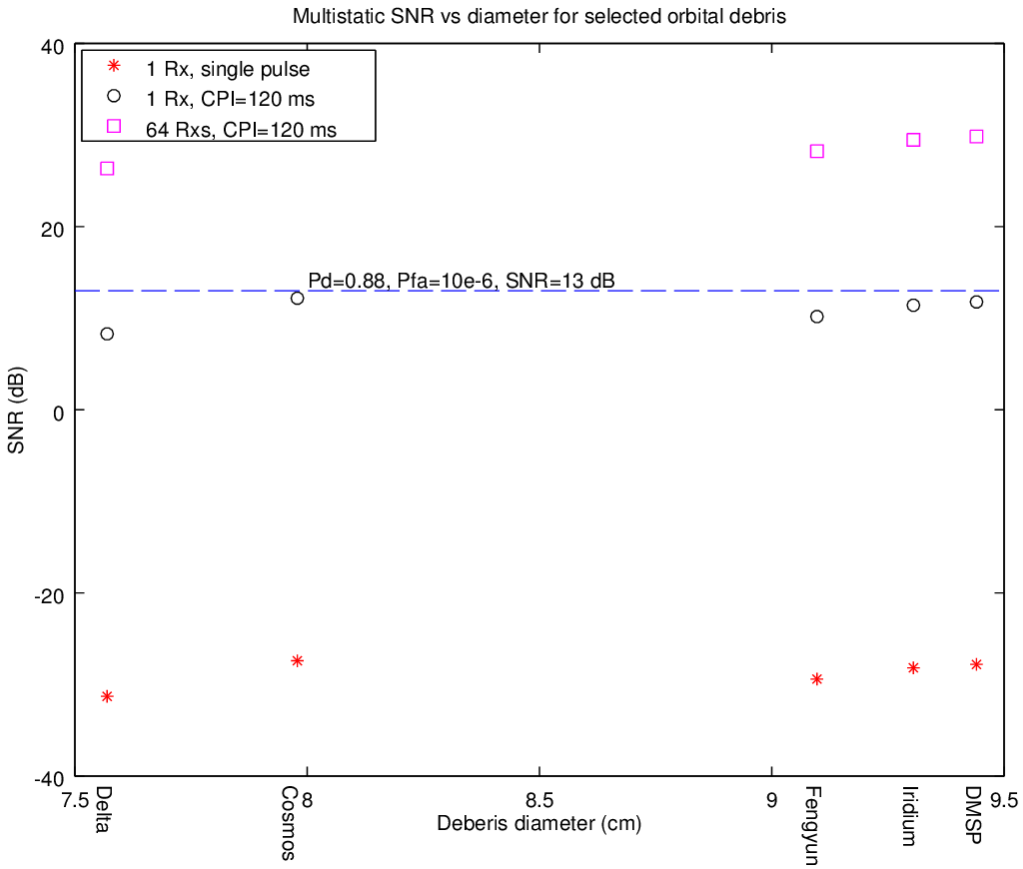

Figure 4.3: Debris SNR vs diameter for the multistatic configuration showing SNR improvement from bistatic set-up to the multistatic set-up. The SNR improvement is about 15 dB accounting for losses due to different orientations of receivers with respect to the target.

where F_T and F_R are the transmitter and receiver propagation factors, k is the Boltzmann constant and T_n is the receiver noise temperature.

Using FERS, coherent and non-coherent radar simulations for debris were done and the results are shown in Figures 4.5, 4.6 and 4.6.

Let s be the average spacing between the n_r receiving elements, the receiver HPBW and given by:

$$\frac{0.866s}{n_R} \tag{4.10}$$

Even though multiple receivers increase the gain of the receiving array by a factor

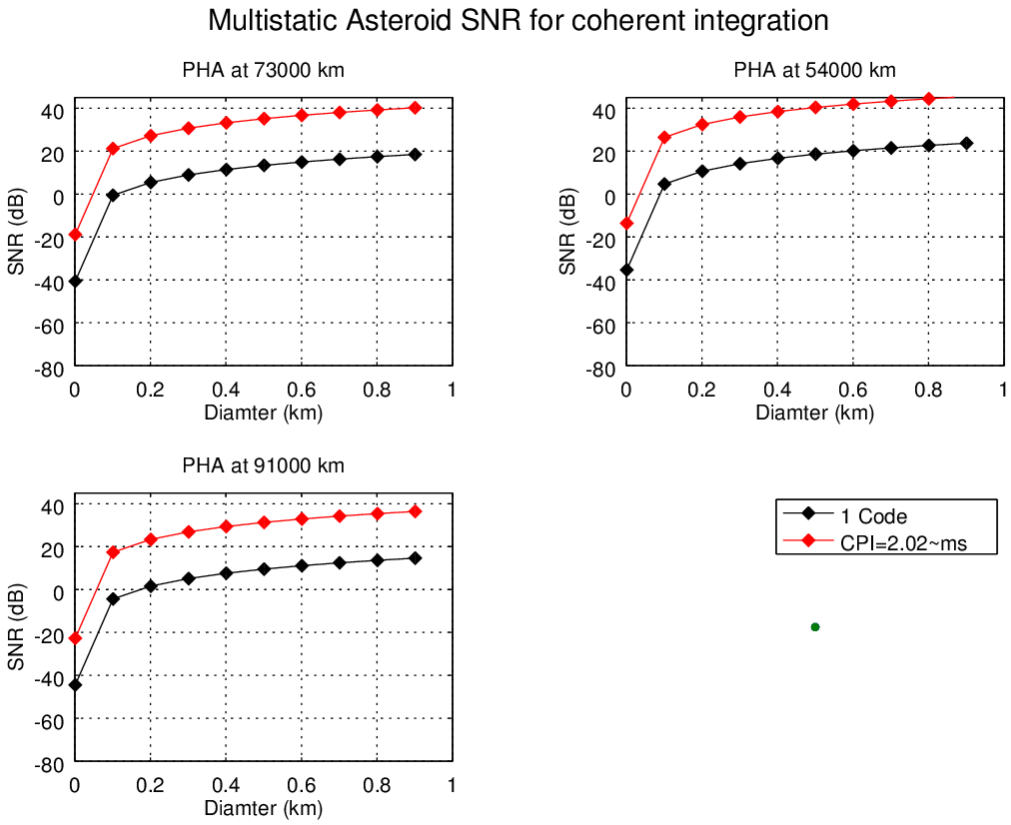

Figure 4.4: Asteroid SNR vs diameter for the multistatic configuration showing improvement from biststic set-up using a single code to the multistatic set-up with 11 Barker codes within a CPI of 2.02 ms.

of n_R as shown in Figure 4.3 for debris and 4.4 for asteroids, the radar beam becomes large making it difficult to pinpoint exactly where the target position is. The next section shows how beamforming can be applied to the receiver array to create a smaller beam pointing in a specified direction.

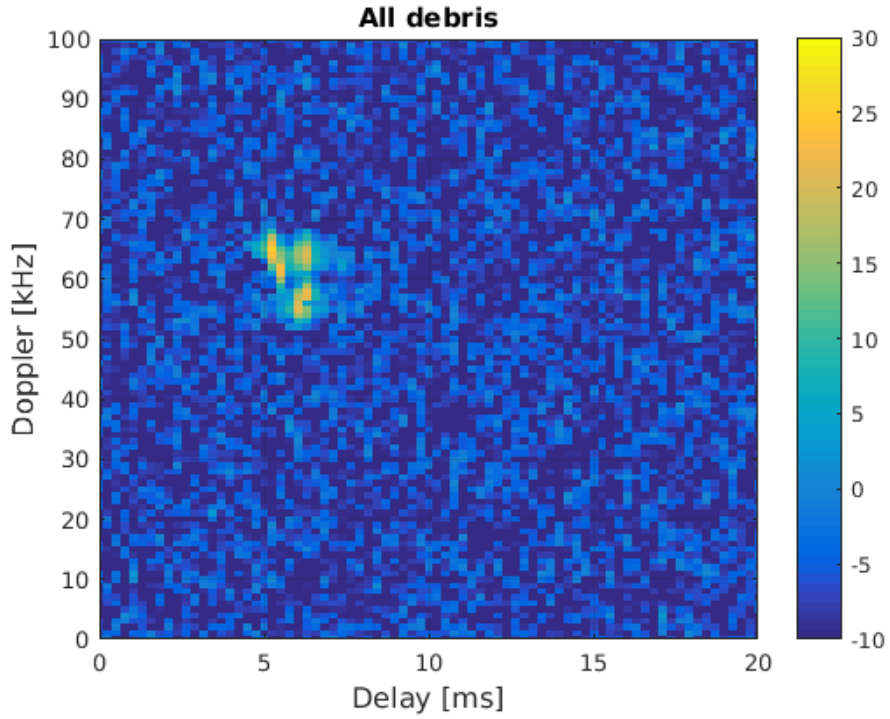

Figure 4.5: Figure showing the output from the radar simulator (FERS) for coherent multistatic radar data from all small debris representative objects. Due to the SNR improvement, the 5 objects can all be observed at the expected delay and Doppler frequencies.

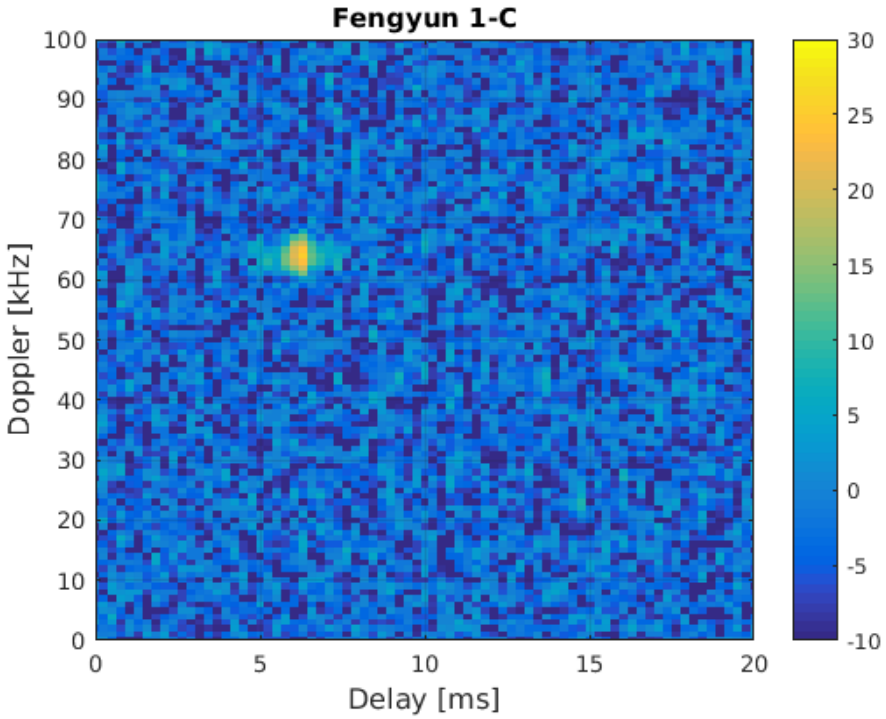

Figure 4.6: Figure showing the output from the radar simulator (FERS) for coherent multistatic radar data from Fengyun 1-C debris object, observed at the expected delay and Doppler frequency.

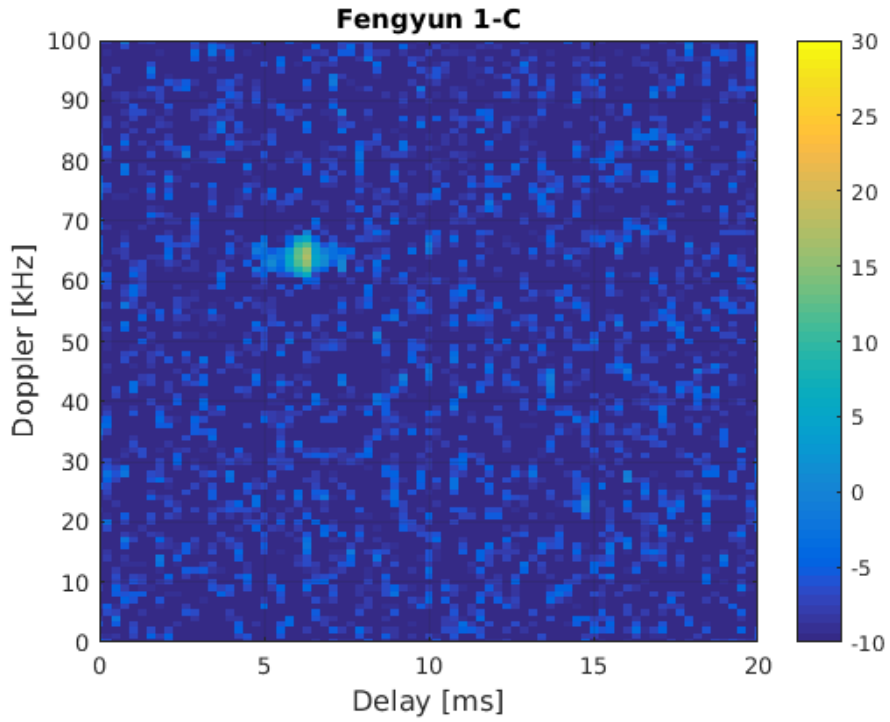

Figure 4.7: Figure showing the output from the radar simulator (FERS) for non-coherent multistatic radar data from Fengyun 1-C debris object, observed at the expected delay and Doppler frequency but with a lower SNR as a consequence of non-coherent integration.

4.2 MeerKAT SIMO radar with sub-arrays

In the MeerKAT SIMO radar, the 64 receivers are divided into 3 concentric circular sub-arrays such that the inner sub-array which consists of 44 antennas has a diameter of 0.5 km, the middle sub-array consists of 11 antennas, within a diameter of 4 km and the outer sub-array consists of 11 antennas within a diameter of 8 km, as illustrated in Figure 4.8.

The geometry for a radar using concentric circular sub-arrays is shown in Figure 4.9 showing how each sub-array is treated as a separate "large" antenna with a "pencil" beam that can be steered in a desired direction. This approximation is possible with the MeerKAT antennas because they are fitted with phase centres which can enable phase "locking" a number of antennas to approximate a "larger" antenna.

The angles of arrival for the Fengyun1-C debris at each antenna in the 3 sub-arrays were plotted in Figure 4.10, which shows the azimuth and elevation range decreasing from the inner, middle and outer sub-arrays. The elevation angles are around 20^o but azimuth angles vary from 20^o to 50^o, with some outliers at 100^o and 250^o. This sub-array approximation was derived from the distribution the multistatic received power at the 64 antennas shown in Figure 4.2 in the previous sub-section.

The SIMO radar geometry illustrated by Figure 4.11 shows the transmitter and receiver sub-systems indicating that at each receiver, a matched filter will be implemented making its implementation similar to a decentralised multistatic radar.

4.2.1 SIMO radar equation and signal model

Let's assume a SIMO radar with N=1 transmitter and M receivers, where:

- no mutual coupling occurs between sensors

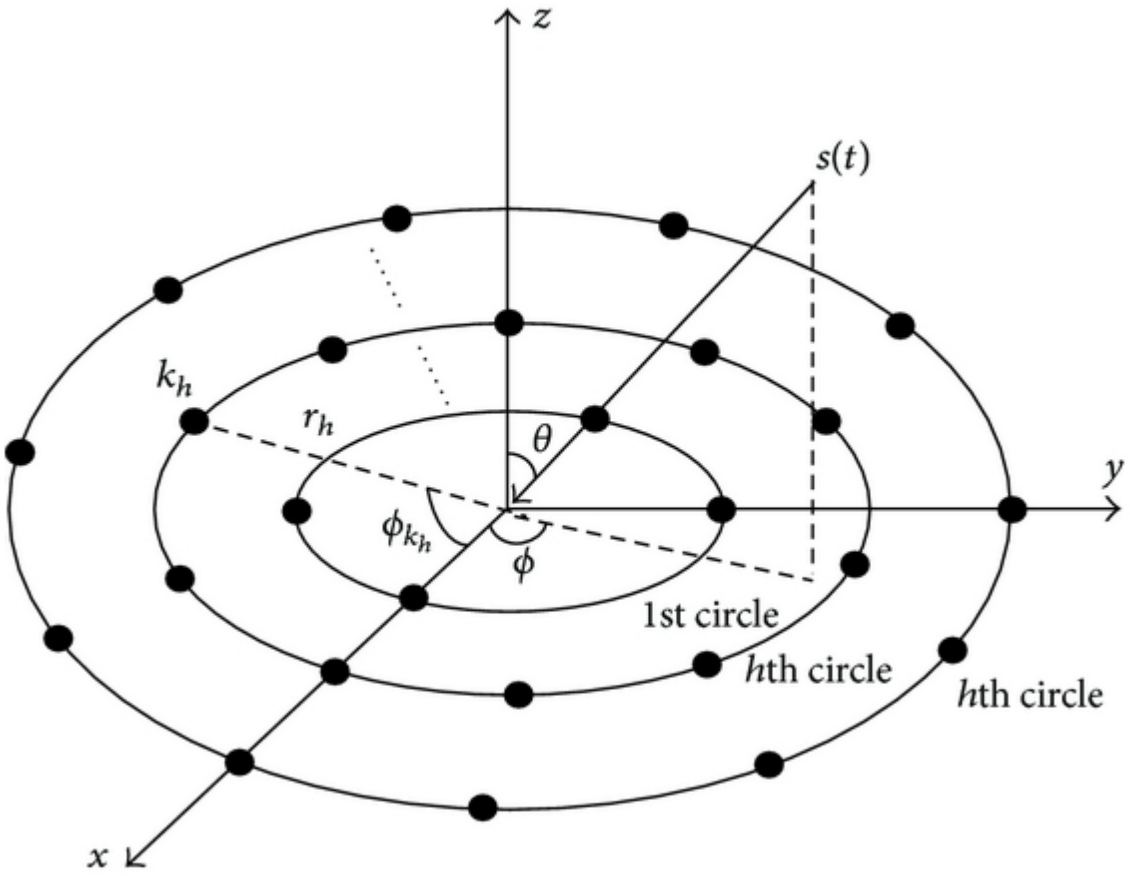

Figure 4.8: Ideal geometry for concentric circular sub-arrays in a local Cartesian coordinate system indicating the incoming signal from the target onto each circular sub-array.

- the transmit and receive sensors are assumed to be fixed on ground (fixed radar)
- transmits nearly orthogonal envelope waveforms
- all sensors operate at the same carrier frequency and bandwidth

Let s_m represent the m^{th} transmitted signal ($m = 1, ..., M$), of the form;

$$s_m(t) = A_0 u_m(t) e^{-j2\pi f_0 t} \tag{4.11}$$

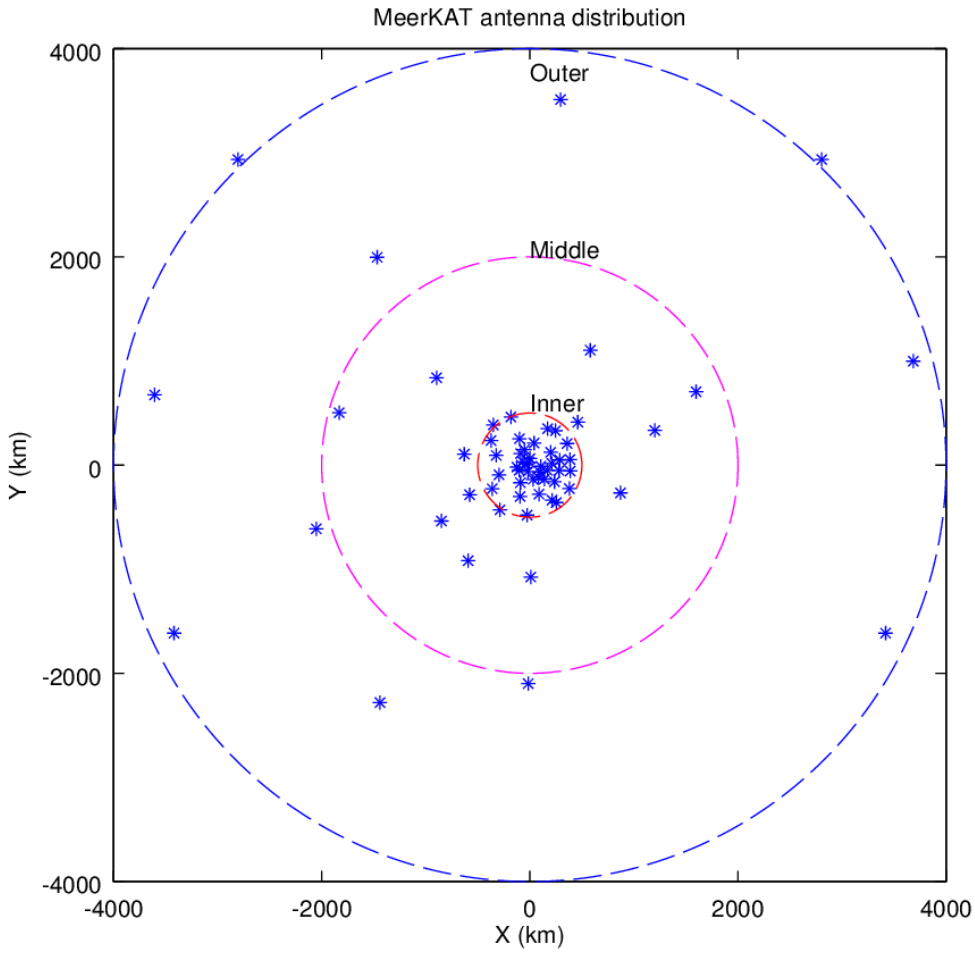

Figure 4.9: MeerKAT antenna distribution showing the approximate geometry of the inner, middle and outer concentric circular sub-arrays with diameters of 1 km, 4 km and 8 km. The MeerKAT antennas are distributed in a Gaussian set-up, however, for this analysis, the concentric circular sub-arrays is an acceptable approximation.

where A_0 represents the amplitude of modulation, u_m represents an orthogonal narrow-band envelope, and can be model by;

$$u_k(t) * u_l^*(-t) = \beta(t)\delta_{kl}(t) \tag{4.12}$$

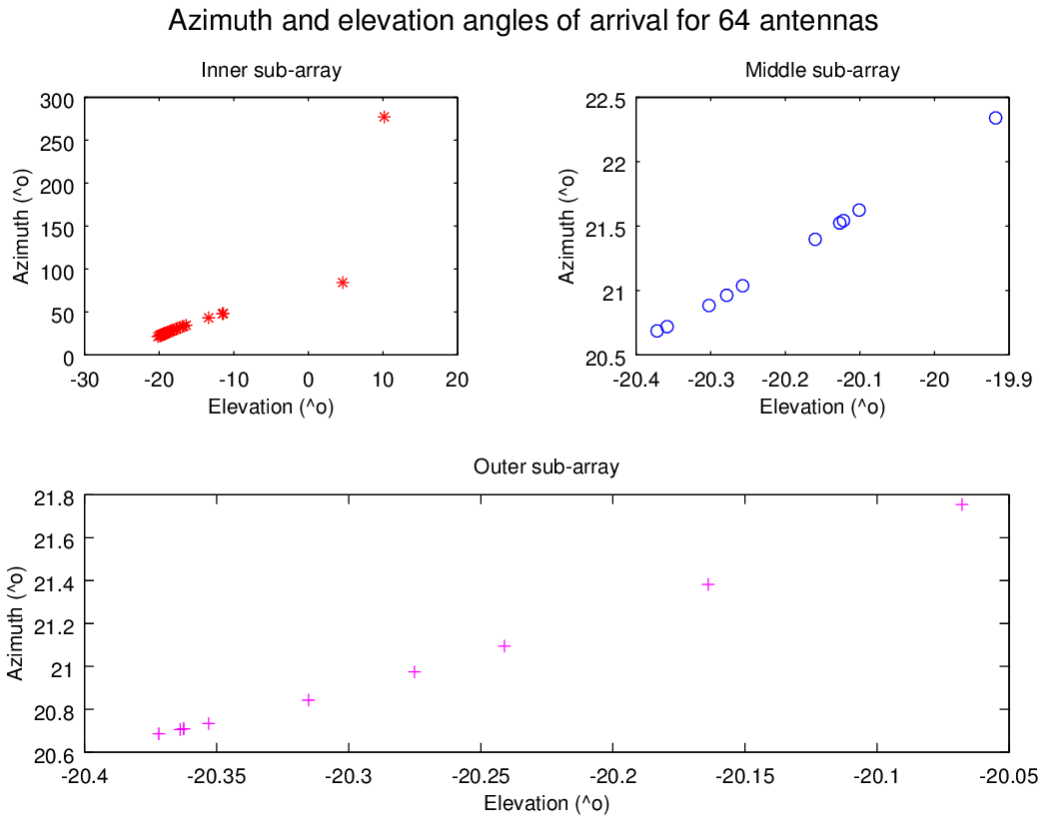

Figure 4.10: Figure showing angles of arrival for signals reaching the MeerKAT antennas at each sub-array. Azimuth receive angles range from 20 to 60 degrees with some outliers at 100 and 300 degrees, and elevation angles from -20 to -10 degrees with outliers at 10 and 20 degrees. For this analysis, the outliers are ignored.

where * represents the convolution operation, $\beta(t)$ represents the main-lobe response or base-band waveform, which is assumed to be the same for all M transmitted signals.

If we assume that the targets in the far field of the arrays can be viewed as an ideal point target model and the signal propagation channels in the space are ideal, then the propagation channel properties can be modelled with parameter time delay, with different path-lengths having different time delay.

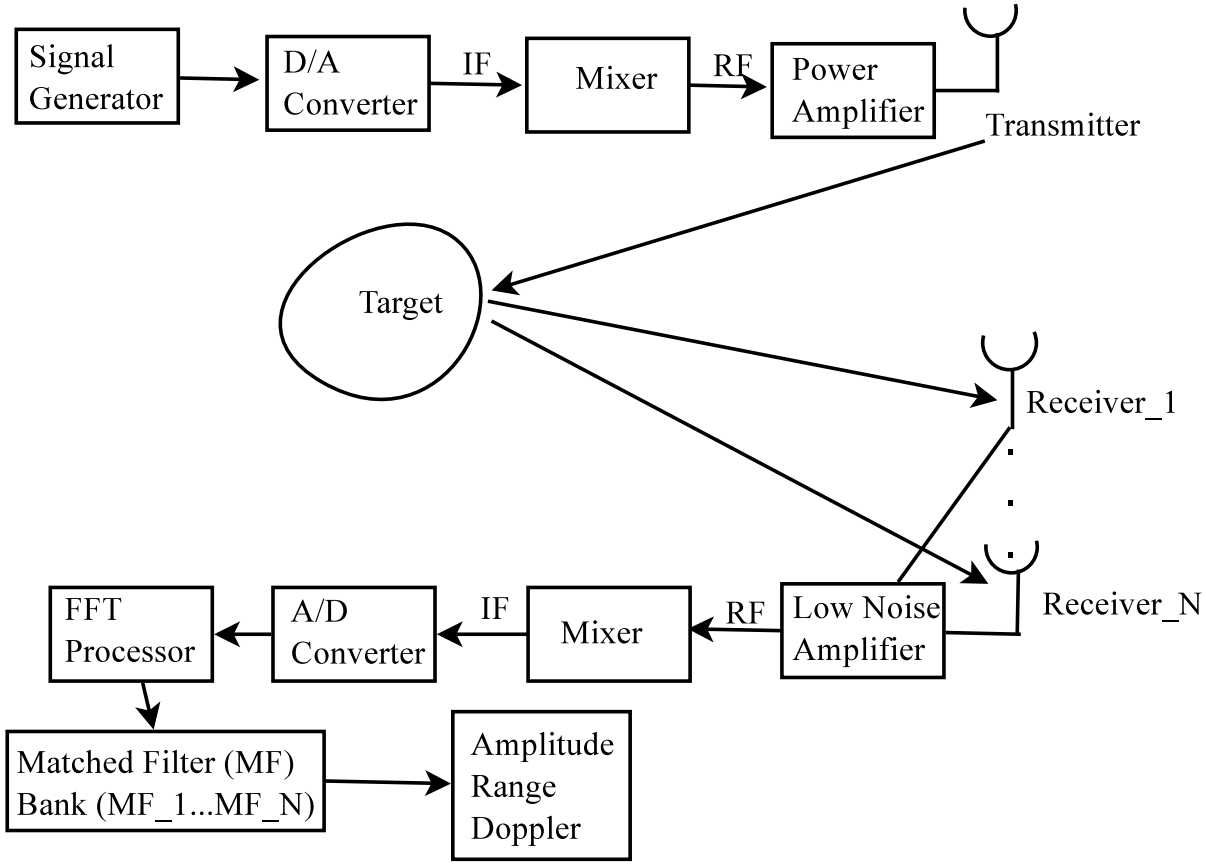

Figure 4.11: MeerKAT single in-put multiple out-put (SIMO) radar block diagram indicating the signal generation, transmission, reception and post-processing blocks. Important to note is the decentralised processing where there is a matched filter at each receiver compared to the centralised processing considered in the multistatic configuration.

The transmitted signals propagate through free space to the $n^{th}(n = 1, ..., N)$ receiver array element over a time delay $\tau_m + \tau_n$, and is scattered by an ideal target with response a_0, producing;

$$s^r_{mn}(t) = a_0 A_0 u_m(t - \tau_m - \tau_n) e^{-j2\pi f_0(t-\tau_m-\tau_n)} \tag{4.13}$$

where τ_m represents the one-way relative time delay from the m^{th} transmit array element to the target, and τ_n represents the one-way relative time delay from the target to the n^{th} receive array element. The n^{th} receiver array element, in free

space, observers the superposition of all the N orthogonal waveforms [99]:

$$s_n^r(t) = \sum_{m=1}^{M} a_0 A_0 u_m(t - \tau_m - \tau_n) e^{-j2\pi f_0(t-\tau_m-\tau_n)} \tag{4.14}$$

During the A/D conversion, s_n^r gets contaminated with thermal noise, which can be modelled as additive Gauss white noise. Thermal noise in different receive channels before digitisation will not be correlated, but have the same power:

$$N_0 = kT_sB_s$$

where $k = 1.38e-23J/K$ is Boltzmann's constant, T_s is the receiver input noise temperature in degree Kelvin, and B_s is the bandwidth of the receive channels, we assume here that all the processing channels have the same bandwidth.

Each receive array element has M' different matched filters (MF). At this point, the orthogonal property of the waveforms are exploited as each MF may match to a specified transmitted signals, and it can be implemented by making the m^{th} MF's impulse response $h_m(t)$ of each receive array element satisfy

$$h_m(t) = u_m^*(-t) \tag{4.15}$$

After filtering, the received signal of the n^{th} receive array element corresponding to the m^{th} transmitted signals can be separated from s_m^r, and it can be written as;

$$s_{mn}^r \quad (t) = a_0 A_0 u_m(t - \tau_m - \tau_n) * u_m^*(-t) e^{j2\pi f_0(\tau_m+\tau_n)} + n_n(t) * u_m^*(-t) \tag{4.16}$$

N receive array elements, will have NM matched filter outputs. All the NM signals will be then sent to beamformer which includes transmit beamforming and receive beamforming. If the main lobes of transmit beamformer and receiving

beamformer are all point at the target, $\tau_m = \tau'_m, \tau_n = \tau'_n$, the output of beamformer is of the form:

$$y_{out}(t) = MNa_0A_0\beta(t) + \sum_{m=1}^{M}\sum_{n=1}^{N} N_{0,mn}(t) \tag{4.17}$$

Noise from one transmitter to several receivers is not correlated, so the matched filtered received signal can be viewed as MN coherent pulses integration under the additive white noise background, and the SNR of the beamformer output will be improved MN times than single matched filter output.

4.2.1.1 SIMO radar equation

Let P_n represent the transmitted power of the $n^{th}(n = 1, ..., N)$ array element ($N = 1$ for SIMO radar), and A_n^e represent the effective aperture of the $m^{th}(n = 1, ..., N)$ receive array element. For the transmit antenna gain of G_s. The power of the m^{th} reflected signal received by the n^{th} receive array element is:

$$P_{mn}^{\text{SIMO}} = \frac{P_m G_s \sigma_0 A_n^e}{(4\pi)^2 R_0^4} \tag{4.18}$$

where R_0 represents the distance between the target and array antenna, σ_0 represents the target Radar Cross Section (RCS) [100].

After down mixing, matched filtering, and transmit digital beamforming, the power of the n^{th} transmit beamformer output is

$$P_m^{\text{SIMO}} = \frac{G_s \sigma_0 A_n^e}{(4\pi)^2 R_0^4} \sum_{m=1}^{M} P_m \tag{4.19}$$

The transmit beam former output is then sent to the receive digital beamformer

and the power of the array processing output is:

$$P^{\text{SIMO}} = \frac{G_s \sigma_0}{(4\pi)^2 R_0^4} \sum_{m=1}^{M} P_m \sum_{n=1}^{N} A_n^e \tag{4.20}$$

The antenna effective aperture is related to the antenna's gain and the wavelength by

$$A^e = \frac{G\lambda^2}{4\pi},$$

so we have;

$$\sum_{n=1}^{N} A_n^e = \sum_{n=1}^{N} \frac{G_n \lambda^2}{4\pi} \tag{4.21}$$

where G_n represents the n^{th} receive array element gain. If the total transmitted power is MP_0, then

$$\sum_{m=1}^{M} P_m = MP_0.$$

We now get:

$$P^{\text{SIMO}} = \frac{MP_0 \sigma_0 \lambda^2}{(4\pi)^3 R_0^4} G_s \sum_{n=1}^{N} G_n \tag{4.22}$$

The SIMO array output is given by:

$$P^{\text{SIMO}} = \frac{MP_0 G_{\text{SIMO}}^2 \sigma_0 \lambda^2}{(4\pi)^3 R_0^4} \tag{4.23}$$

Assuming that that all the array element's gain are identical, and not considering the antenna electromagnetic characteristic, like coupling effect, the SNR at the array output with noise level of N_0 is

$$SNR_{\text{SIMO}} = \frac{MP_0 G_{\text{SIMO}}^2 \sigma_0 \lambda^2}{(4\pi)^3 R_0^4 N_0} \tag{4.24}$$

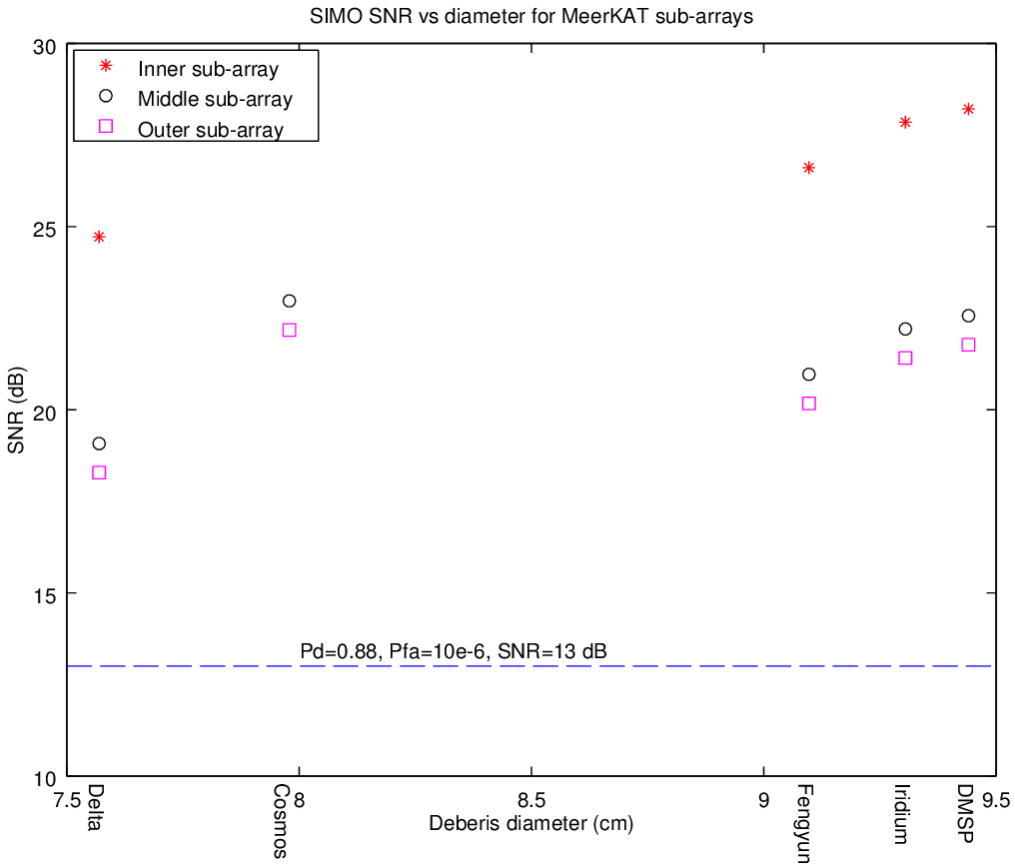

Figure 4.12: A plot showing SNR from the MerKAT SIMO radar for the inner, middle and outer circular concentric sub-arrays after coherent integration of 152 pulses. The SNR improvement is greatest in the inner sub-array because it has the largest number of antennas (44) closely spaced compared to the middle and outer sub-arrays each with 10 antennas but with different diameters.

Figures 4.12, 4.13 and 4.14 show the theoretical SIMO radar SNR for the 3 sub-arrays and the simulated range-Doppler plots for coherent and non-coherent MeerKAT SIMO radar for the Fengyun 1-C debris, respectively.

4.2.2 SIMO radar multi-beam tracking

The SIMO radar gives rise to a virtual array known as a co-array, whose overall beam pattern is the product (composite) of the transmit and receive

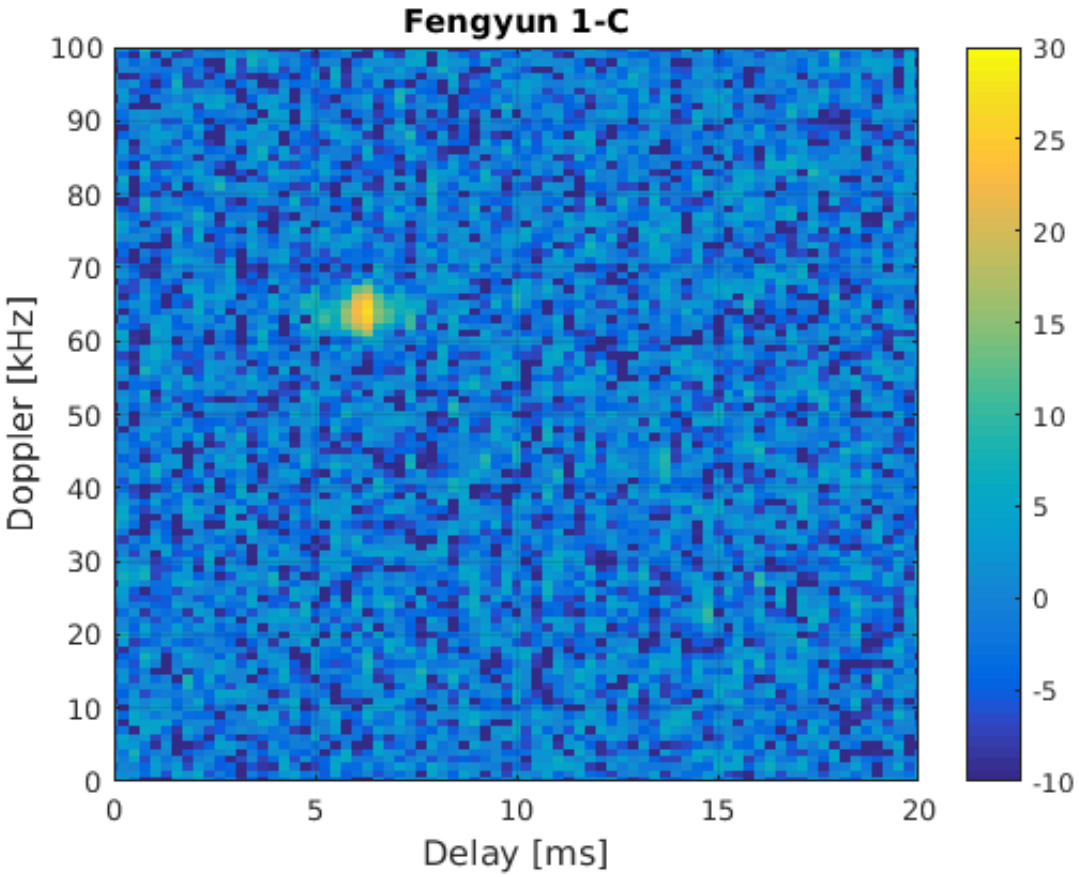

Figure 4.13: Figure showing the output from the radar simulator (FERS) for coherent SIMO radar data from a Fengyun 1-C debris object, observed at the expected delay and Doppler frequency and with comparable SNR to the multistatic configuration.

beam patterns [83]. The overall beam pattern is defined by a weight vector w_{tr} that equals the convolution of the transmit beamformer w_t and the receive beamformer w_r :

$$w_{tr} = w_t * w_r \tag{4.25}$$

The new weight vector w_{tr} can be viewed as a beamformer of a longer co-array.

We make use of the SIMO co-array property to a implement multi-beam system in delay and sum (DAS) beamforming on receive. Multi-beam target tracking simulations were done for t he MeerKAT SIMO radar. Using multiple beams

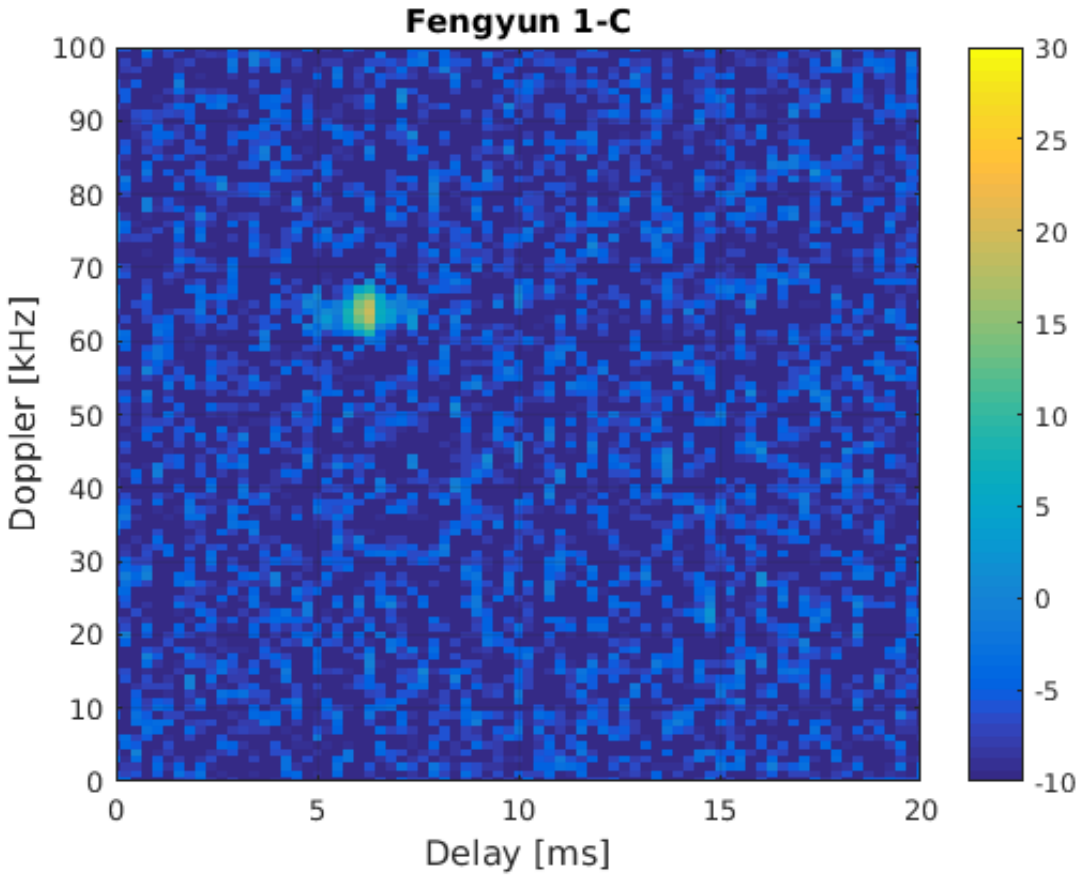

Figure 4.14: Figure showing the output from the radar simulator (FERS) for non-coherent SIMO radar data from a Fengyun 1-C debris object, observed at the expected delay and Doppler frequency but with a lower SNR as a consequence of non-coherent integration.

increases track time by "stacking" the beams from the 3 sub-arrays together at the 3 dbB point.By adjusting the azimuth and elevation angles of each sub-array beam, and mimicking a 3D view of the target.

DAS beamforming operates under similar principles to radio Astronomy interferometry for a target in a far field. For each beam, the received signals from each antenna are transformed from time domain to frequency domain using FFT, then the signal amplitude is multiplied by an appropriate weighting factor, the weighted signals are then summed, converted back to time domain to obtain a beamformed output.

The array factor (AF) for a circular configuration, such as the MeerKAT sub-arrays, for N antennas placed in the X-Y plane along a circular ring of radius a, is given by:

$$AF_{circ} = \sum_{n=1}^{N} I_n exp(j(ka\sin(\theta)\cos(\phi - \phi_n) + \sigma_n) \tag{4.26}$$

where I_n is the amplitude excitation of the n^{th} element, $\phi_n = \frac{2\pi n}{N}$ is the n^{th} angular position of element, σ_n =phase excitation of the n^{th} array element. The maximum of the AF occurs when all the phase terms are equal. And for $\sigma_n = 0$, the maximum occurs in the direction $\theta = 0^o$.

The beamformer output from the inner, middle and outer concentric circular sub-arrays and the resultant beam for a target at 20^o is shown in Figure 4.15. The 3D view of the beamformer output for the three sub-arrays is plotted in Figure 4.16. Figure 4.17 shows the SNR improvement after beamforming and instantaneous spatial matched filtering for received signals in additive while Gaussian noise. The inner sub-array has the greatest SNR improvement compared to the middle and outer sub-arrays, due to the large number of receivers (44 antennas). Figure 4.18 compares the simulated bistatic, multistatic and SIMO radar capabilities in radar detection.

4.2.2.1 Multi-beam tracking of small space debris

Tracking of small space debris is important in verifying and updating their orbital parameters in catalogs. Multi-sensor tracking requires a mechanically scanning sensor, however in this approach, we implement multiple beams "stacked" together in the direction of the target. A linear target track is simulated using FERS and plotted with error bars showing deviation of theoretical delay and Doppler for small debris. Three beams from the three concentric circular sub-arrays are used to implement multi-beam tracking and to mimic 3D capability by concatenating the three beams. Figure 4.19 shows that it is possible to track small space debris at altitudes less that 1000 km using multiple

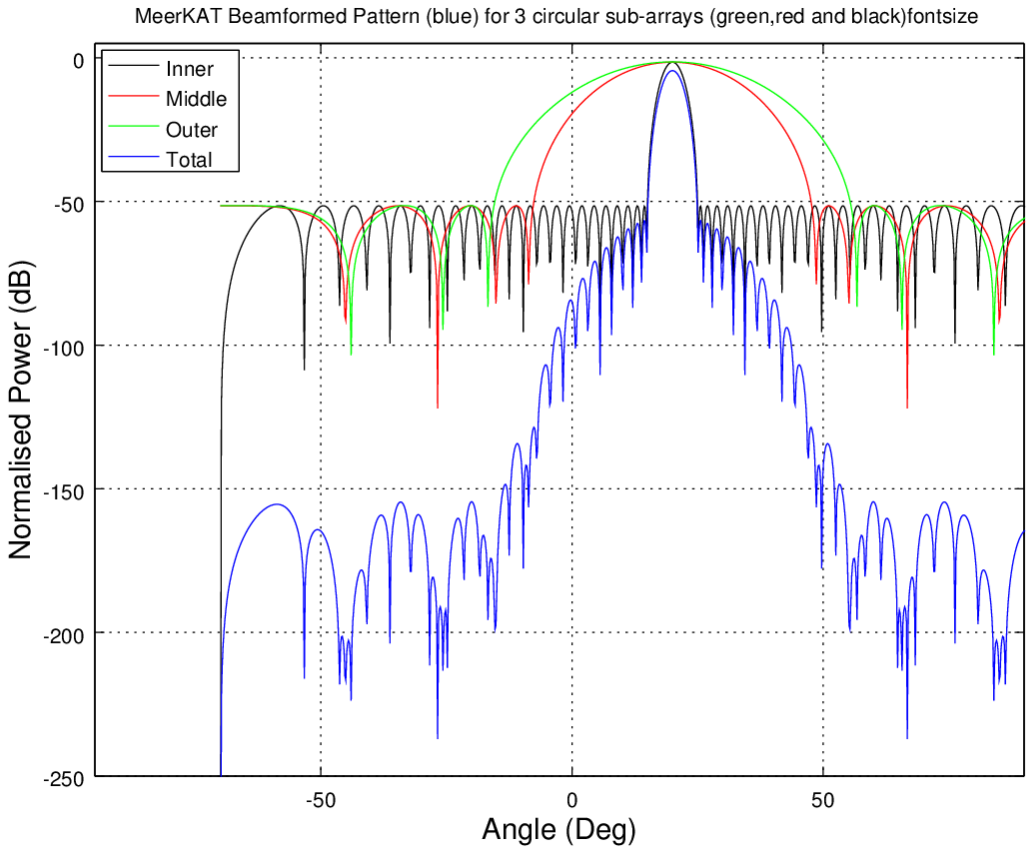

Figure 4.15: Delay and sum beamformer output for the inner (black), middle (red) and outer (green) circular sub-arrays for the MeerKAT radar. The resultant beam from the 3 sub-arrays is shown in blue

beams. The simulated and theoretical debris tracks matched well and the inner sub-array gave the least error bars compared to the middle and outer sub-arrays.

4.3 ISAR debris imaging

We consider the use of LFM waveform in an inverse synthetic aperture radar (ISAR) for small debris imaging because of the benefits of high resolution in both down range (direction of propagation of the radar beam) and cross range (distance from the axis of rotation) [101]. In the ISAR imaging simulations, a

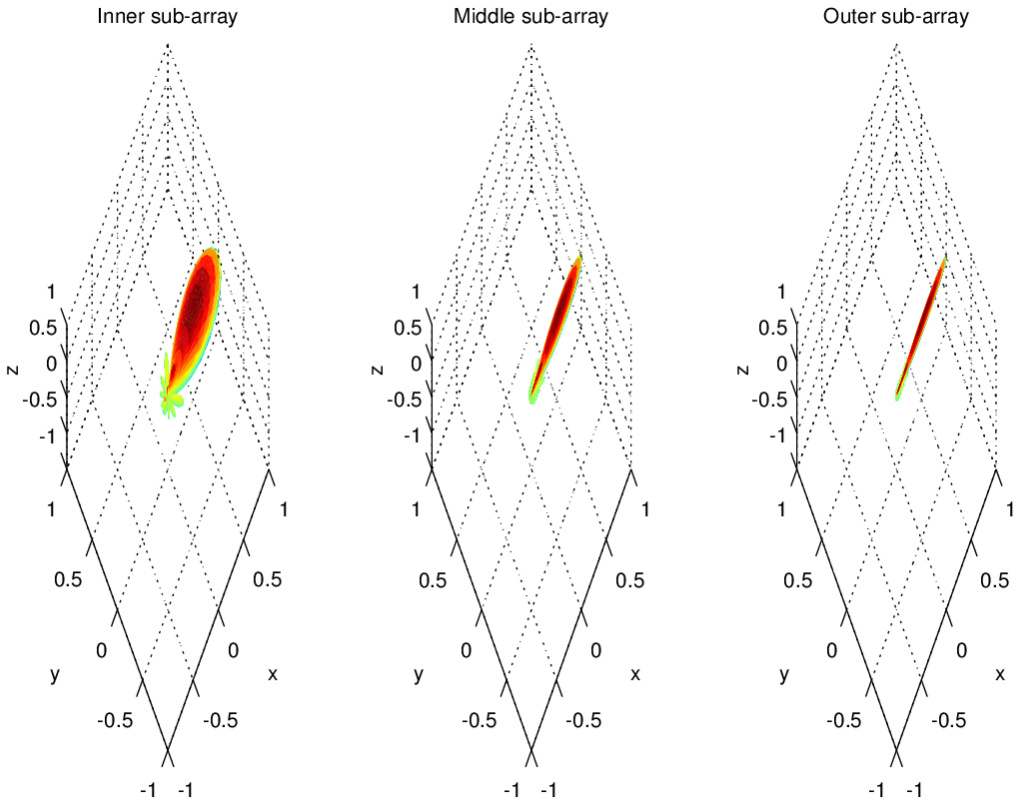

Figure 4.16: 3D view of the inner, middle and outer sub-arrays beams showing the beams becoming "thin" as the circular sub-array diameter increases.

linear imaging approximation was assumed and the following assumptions were made for the target [102]:

- only constant target rotation
- constant angular rotation speed of ω rad/s about the axis perpendicular to the horizontal plane
- no translational motion between the radar and the target
- all scatters on the target and the radar are on the same horizontal plane
- small viewing angle change during the PRI

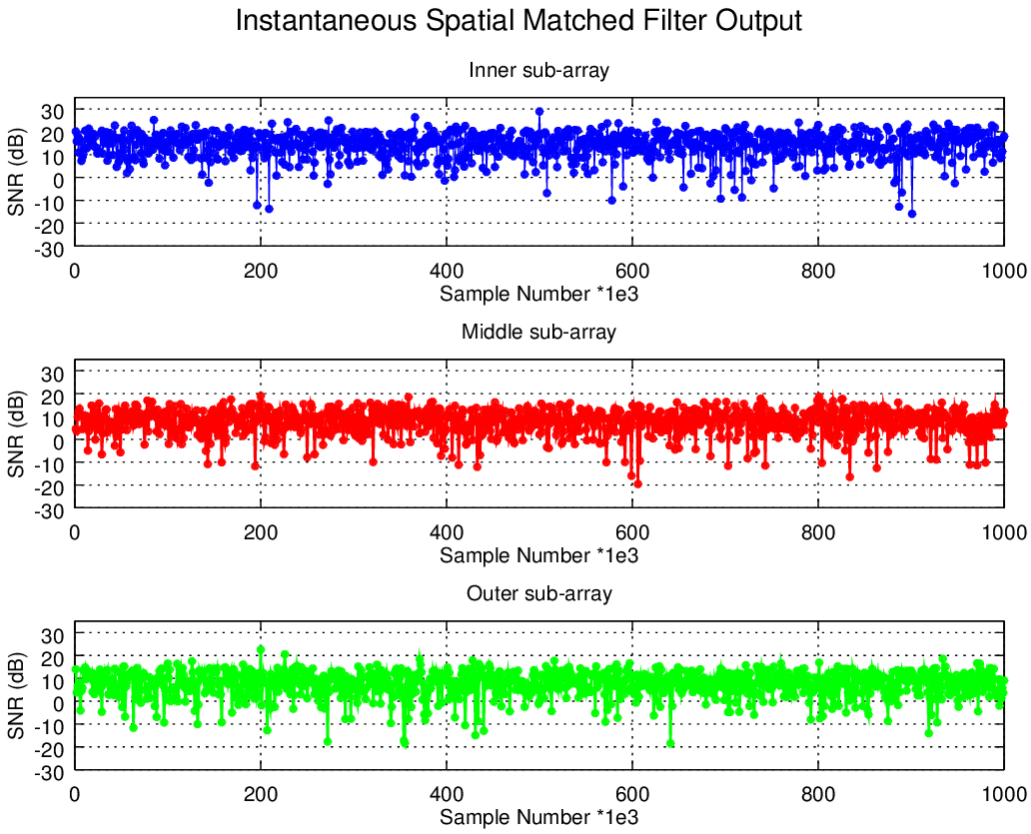

Figure 4.17: Additional SNR improvement after beamforming through matched filtering for a signal arriving at the inner, middle and outer sub-arrays. The signal, which is embedded in additive while Gaussian noise, is seen to be "amplified" most at the inner array due to the large number of receivers (44 antennas) compared to the middle and outer arrays (10 antennas).

Let the transmitted LFM waveform of bandwidth B, at the centre frequency f_c and LFM coefficient, $\mu = B/\tau$, be of the form:

$$s_{tx}(t) = \text{Rect}(\frac{t}{\tau})exp(j2\pi(f_c + \frac{\mu}{2}t^2) \tag{4.27}$$

For a target at range R from the radar with M prominent scatters each with a

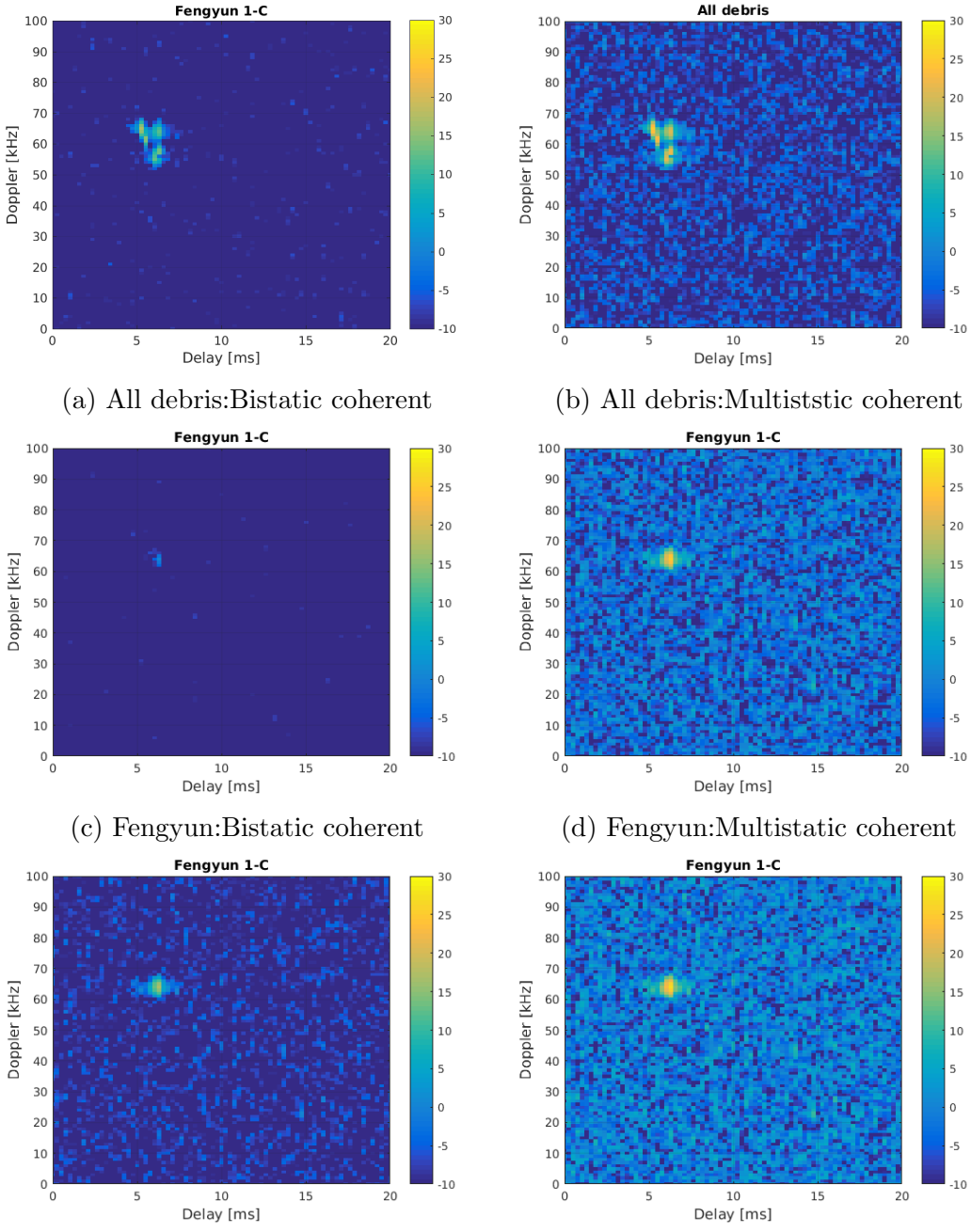

(a) All debris:Bistatic coherent

(b) All debris:Multiststic coherent

(c) Fengyun:Bistatic coherent

(d) Fengyun:Multistatic coherent

(e) Fengyun:Multistatic non-coherent

(f) Fengyun:SIMO coherent

Figure 4.18: Simulated delay-Doppler map for all debris for the bistatic, multistatic and SIMO geometries for both coherent and non-coherent processing.

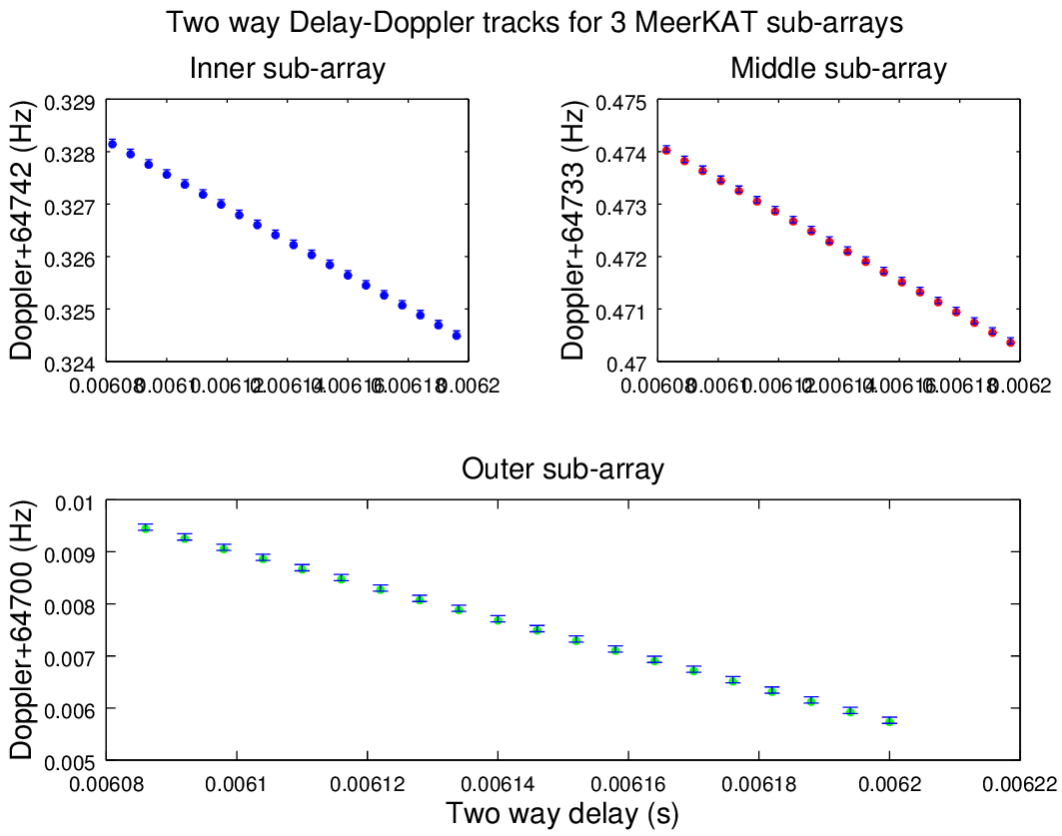

Figure 4.19: Simulated debris tracks with error bars showing deviation of simulated from calculated delay and Doppler frequencies for signals arriving at the inner, middle and outer circular sub-arrays.

time delay of , the received echo can be of the form:

$$s_{rx}(t) = \sum_{i=1}^{M} \text{Rect}(t - d\tau_i) exp(j2\pi[f_c(t - d\tau_i) + \frac{1}{2}\mu(t - d\tau_i)^2)] \tag{4.28}$$

As opposed to correlation, we choose the stretch pulse compression technique for easy implementation. The stretch technique uses a narrow bandwidth intermediate filter since the reference signal in the received filter is $e^{(j2\pi(f_c+\frac{\mu}{2}t^2)}$. The reduced sample number as shown by: $2BT_{rec}$, depends on the receive time window T_{rec}. The stretch processing technique generates a range image $s(L)$,

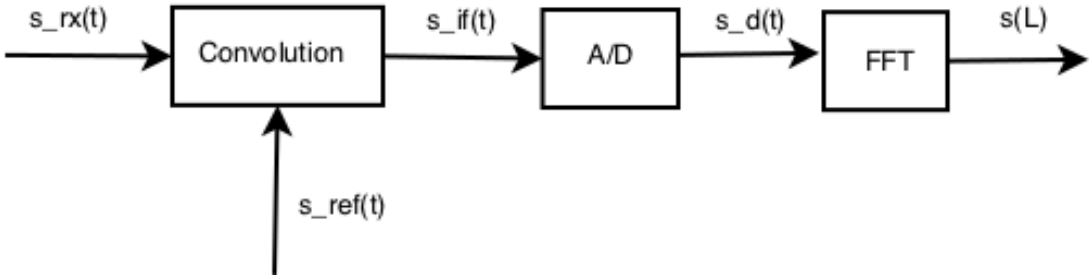

Figure 4.20: Illustration of the stretch technique showing the received signal $s_{rx}(t)$, the reference signal $s_{ref}(t)$, the intermediate frequency output $s_{if}(t)$, which becomes $s_d(t)$ after A/D conversion and then $s(L)$ after applying FFT.

following the steps shown in Figure 4.20.

For a manoeuvring target, the radial velocity (v) for the translational motion and angular rotation rate (ω) for the rotational motion are both time varying. However, for simplicity, we assume that v and ω remain constant during the integration time [37]. We chose a constant rotation rate of 5 degrees, such that the scatterers (pieces of debris) on the target (debris cloud) stay in one range and Doppler resolution cell during the observation time [103]. A debris cloud containing randomly distributes small debris is simulated and the following parameters are used in the imaging model can be summarised as:

- Total angle that the target is rotated through $\Delta\theta = \frac{2\pi\omega r_c}{\lambda}$
- Δ_R the system range measurement error at 20 dB
- $\delta_R = \Delta_R$ is the random range measurement error
- Doppler: $f_d = \frac{2\omega r_c}{c} f_c$
- Target extent, L for debris cluster
- Receive time window: $T_{rx} = \frac{4(D+\Delta R+3\sigma_R)}{\lambda}$
- Cross-range resolution: $\Delta R_c = \frac{c}{2\omega T_{\text{int}} f_c}$
- Down-range resolution: $\Delta R_d = \frac{c}{2B}$

- Unambiguous Doppler window: $W_c = \frac{c \times PRF}{2\omega f_c}$
- Range migration is limited by keeping $N_{c,d} = \left(\frac{r_{c,max}}{\Delta R_{c,d}}\right)^2 \lambda$ less than unity

An ISAR image constructed from M range profiles, each containing N range cells generating M Doppler spectra using parameters in Table 4.1 is shown in Figure 4.21. The output from this LFM ISAR simulation is a MXN 2D cross-range down-range image [102]. In order to minimise/eliminate effects due to range-Doppler interaction and range cell migration, the radial velocity of the scatterers is kept constant throughout the integration time.

Table 4.1: Parameters used in the ISAR algorithm defining the target and radar environment.

Parameter	Value	Units
L	10	m
M	100	range profiles
N	128	range cells
Δ_R	0.014	m
T_{rx}	0.133	μs
B	750	MHz
ΔR_c	1.94	m
ΔR_d	0.2	m
T_{int}	0.67	2

The ISAR image shown in Figure 4.22 shows the image of the 5 debris scatters within the debris cloud. The image was made clear by use of the CLEAN algorithm, which works by subtracting the normalised complex point spreading function (PSF) of target response from the cross correlated value of the range domain map [104]. In this approach, we considered only the one dimensional image (that is in range domain) of target after the coherent detection. PSF has been generated based on the autocorrelation of the reference signal.

The CLEAN algorithm works by identifying the brightest spot in the image map, recording its location and intensity and then removing it from the image

map [105]. This procedure is repeated with the next brightest spot in the image map until the remaining image map is below some predefined threshold criterion [106]. The amplitude and position of each source are noted and represent the "cleaned" image as shown in Figure 4.23. Even though the image was made "cleaner" not all objects are clearly visible due to low RCS values.

4.4 Radar accuracy measurements

The accuracy with which a radar measures a target characteristic is determined by several error sources:

- A SNR dependent random measurement error. These errors vary with $SNR^{1/2}$
- A random measurement error having fixed standard deviation, due to noise sources in the radar receiver. These errors are usually small, and correspond to SNR dependent errors produced at large SNR values. Thus, they set a limit on how far random errors may be reduced by increasing SNR.
- A bias error associated with the radar calibration and measurement process. These errors may vary randomly with drift in radar calibration, only with correlation times that are long compared with the usual radar observation period.
- Errors due to radar propagation conditions, or uncertainties in correcting for the propagation conditions.
- Errors from interference sources such as radar clutter and radar jamming signals
- Errors due to target scintillation and glint

The first three error sources above, SNR dependent, fixed random, and bias, are discussed in this work. According to literature, the radar accuracy can be

characterised by using the standard deviation of a Gaussian distribution σ, which reasonably models measurement error distributions for many cases of interest.

4.4.1 Range measurement errors

The range-measurement accuracy is characterised by the rms measurement error, σ_R, given by the root-sum-square (rss) of the three error components: the SNR dependent random range noise measurement error σ_{RN}^2, the range fixed random error given by the rss of the radar fixed random range error σ_{RF}^2 (is equivalent to σ_{RN}^2 at a SNR of 20 dB), the range bias error and the random range error from propagation σ_{RB}^2.

The fixed random range error may limit the range measurement accuracy for large values of SNR. Random range errors due to propagation are usually small, except when multi-path conditions exist. The magnitude of radar range bias errors usually depends on the care taken to reduce them. Since bias errors are constant for a series of measurements, or for multiple targets in the same general area, they do not affect radar tracking or the relative locations of targets.

$$\sigma_R = \sqrt{\sigma_{RN}^2 + \sigma_{RF}^2 + \sigma_{RB}^2} \tag{4.29}$$

The SNR (single pulse SNR or integrated SNR) dependent error usually dominates the radar range error and its random with a standard deviation given by:

$$\sigma_R = \frac{c}{2B\cos^2(\beta/2)\sqrt{(2SNR)}} \tag{4.30}$$

When pulse integration produces a signal processing loss, the integrated SNR should be reduced by this loss factor ($\approx$ 1 dB). In antenna arrays and dish tracking, if the target is not near the centre of the beam (as it is usually assumed), an appropriate beam-shape loss should be used in calculating SNR. Figures 4.25, 4.25 and 4.26, show the range error as a function of pulse width and error in

measuring RCS for debris and asteroids, respectively.

4.4.2 Angular measurement errors

The measurement accuracy in each angular coordinate is characterised by the rms error, σ_A, given by the rss of the three error components;

$$\sigma_A = \sqrt{\sigma_{AN}^2 + \sigma_{AF}^2 + \sigma_{AB}^2} \tag{4.31}$$

where the noise angle error $\sigma_{AN} = \frac{\theta}{(1.6\sqrt{2SNR})}$, and θ is the radar beamwidth. And σ_{AF} is the fixed random error which will limit angular accuracy for large values of SNR, due to random noise in the receiver angular errors will be assumed limited to $1/50^{th}$ of the beamwidth, and σ_{AB} is the bias error which will not affect target short tracks.

4.4.3 Velocity measurement errors

Target radial velocity may be measured in one of two ways; either from multiple range measurements or from direct Doppler frequency measurements. The Doppler radial-velocity measurement accuracy is characterised by the RMS measurement error, σ_V, given by the rss of the three error components:

$$\sigma_V = \sqrt{\sigma_{VN}^2 + \sigma_{VF}^2 + \sigma_{VB}^2} \tag{4.32}$$

where the noise velocity error, $\sigma_V = \frac{\lambda}{2\tau\sqrt{2SNR}}$, λ is the wavelength and τ is the duration of the processed waveform; σ_{VF} is the fixed error and like the fixed range error case will be assumed limited to the noise error at 20 dB SNR. As with the range and angular errors, the bias error will not be considered for short target tracks. Velocity resolution improves with increasing integration time as shown in Figure 4.27. The range, velocity and angular errors for a target arriving at broadside to the receiver are illustrated in Figure 4.28

In order to compare the performance of the MeerKAT 3D radar, its measurement errors are compared to the Haystack, HAX, FPS-85 existing radars that detect and image space debris. Haystack and HAX are MIT long range imaging and characterising debris in the LEO. The FPS-85 is a phased array radar dedicated to space surveillance. The parameters used to compare errors are given in Table 4.2. For debris at 1000 km and SNR of 20 dB, the estimated range, angle, velocity, orbital period and inclination errors given in Table 4.3 show that the MeerKAT radar has the least range error and inclination. The orbital period and angle errors are comparable. The velocity error is greatest for the MeerKAT radar, but increasing the number of pulses coherently integrated reduces the velocity error.

Table 4.2: Table of parameters used to calculate radar measurement errors of the MeerKAT, Haystack, Haystack Auxiliary (HAX) and FPS-85 radars.

Parameter	MeerKAT	Haystack	HAX	FPS-85
Peak power (kW)	2e3	250	50	32e3
Frequency (GHz)	1.35	10	16.7	0.442
Beamwidth (Deg)	0.029	0.058	0.10	1.3
Antenna Gain (dB)	61.062	64	67	43
LFM Bandwidth (GHz)	2	1	2	0.001
τ (ms)	0.005	1.64	1.64	0.25

Table 4.3: Table of MeerKAT 3D radar, Haystack, Haystack Auxiliary (HAX) and FPS-85 radar measurement errors.

Radar	σ_R (m)	σ_v (m/s)	σ_A (Deg)	σ_T (Min)	σ_i (Deg)
MeerKAT	0.0075	10.55	0.028	0.021	0.0057
Haystack	0.0100	0.65	0.001	0.12	0.021
HAX	0.005	0.41	0.002	0.11	0.020
FPS-85	11.00		0.036	0.05	0.001

4.5 Chapter 4 summary

This chapter showed the multistatic and SIMO radar configurations, their signal models and signal processing techniques. The SIMO virtual array was divided into three concentric circular sub-arrays which were used to implement multi-beam debris tracking with increased track time and a 3D coverage. According to simulations, the multistatic radar configuration was found to be the most effective compared to the bistatic and SIMO configurations due to its suitability to the MeerKAT receivers, low computational requirements, lower data storage capacity. The SIMO radar that uses multiple beams gives SNR higher than the multistatic radar by 2 dB due to beamforming.

Debris imaging was simulated using inverse synthetic radar (ISAR) and LFM waveforms and making use of the high down range and cross range resolution that can be attained from stretch processing and DFT. The CLEAN deconvolution algorithm was implemented to improve the image resolution. The small debris were modelled as a larger debris cluster/cloud of diameter 1 m with 5 evenly distributed 10 cm from the origin.

Comparison of radar measurement errors as would be expected from the MeerKAt radar with those from the HAX, Haystack and FPS-85 radars showed superior performance in range and angle measurements. Velocity measurement errors from the MeerKAT radar can be minimised by increasing the number of pulses.

Chapter 5 gives the range, velocity and angular radar measurement error analysis, and how these errors propagate to orbital period and inclination prediction. A discussion on the MeerKAT radar performance compared to existing dedicated contributing space situational awareness assets such as TIRA, Haystack, HAX and Northern Cross. A conclusion is made on how well the research questions were accomplished during this research. The preliminary results obtained for a radar that uses KAT-7 radio telescope receivers are given in Appendix A.

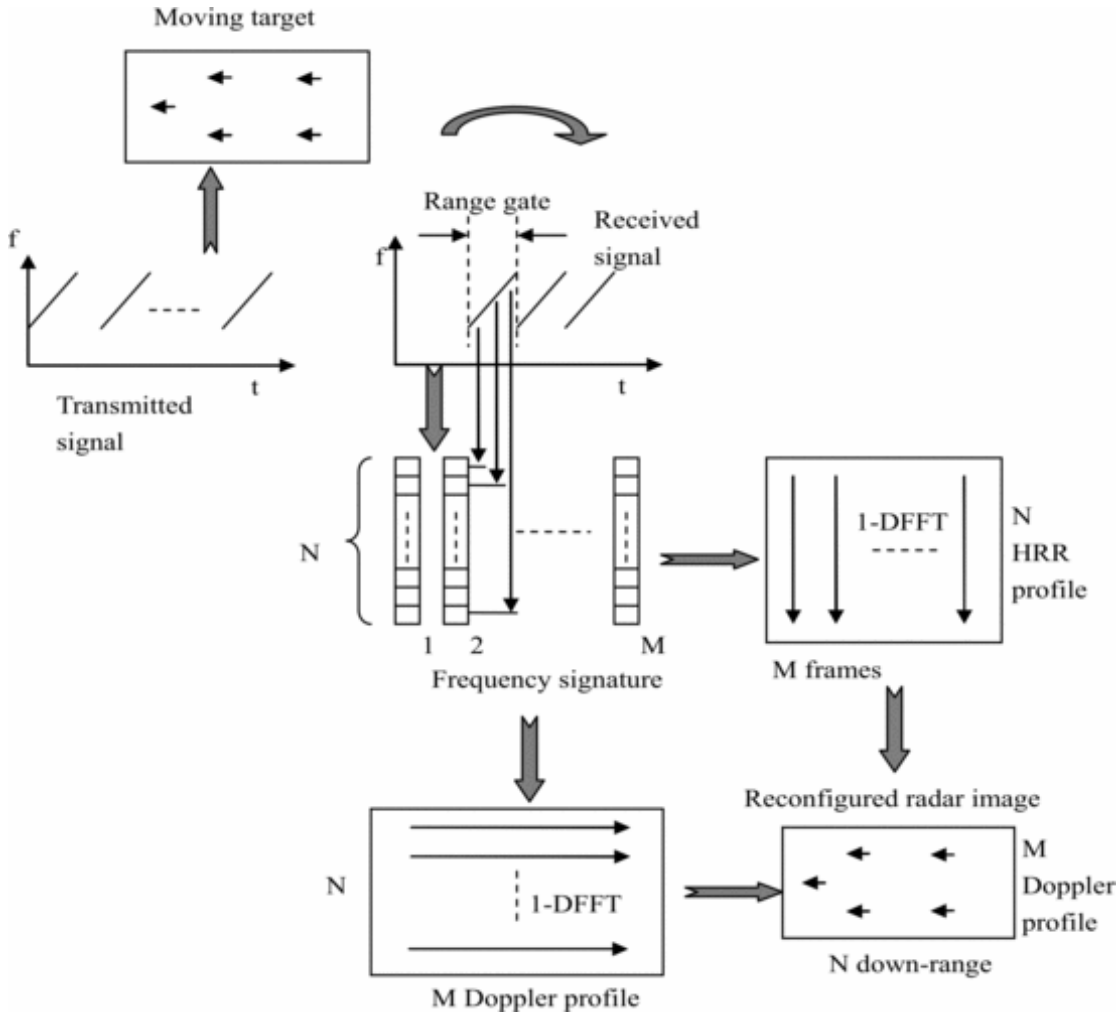

Figure 4.21: Illustration of the procedure taken in the ISAR imaging simulations indicating how the received signal is processed into N high range resolution profiles and M Doppler profiles to form an image.

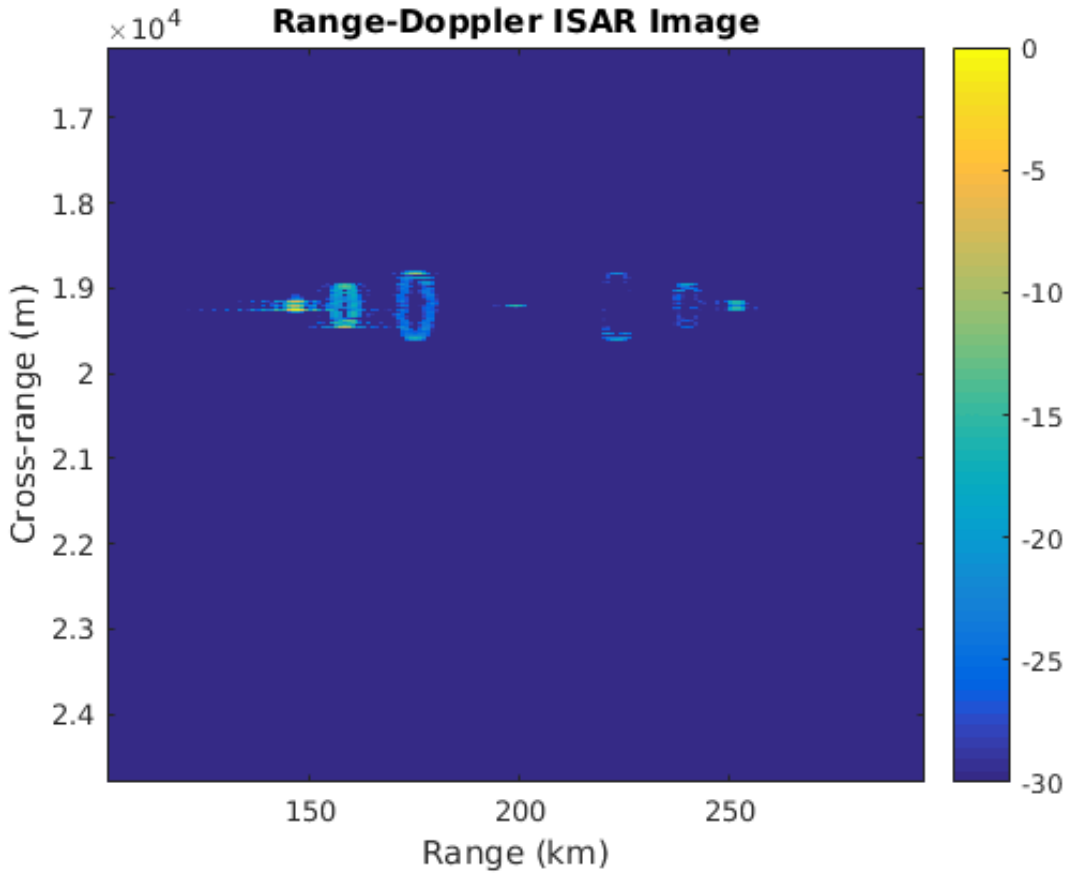

Figure 4.22: ISAR image for 5 representative debris objects showing range and cross-range.

a

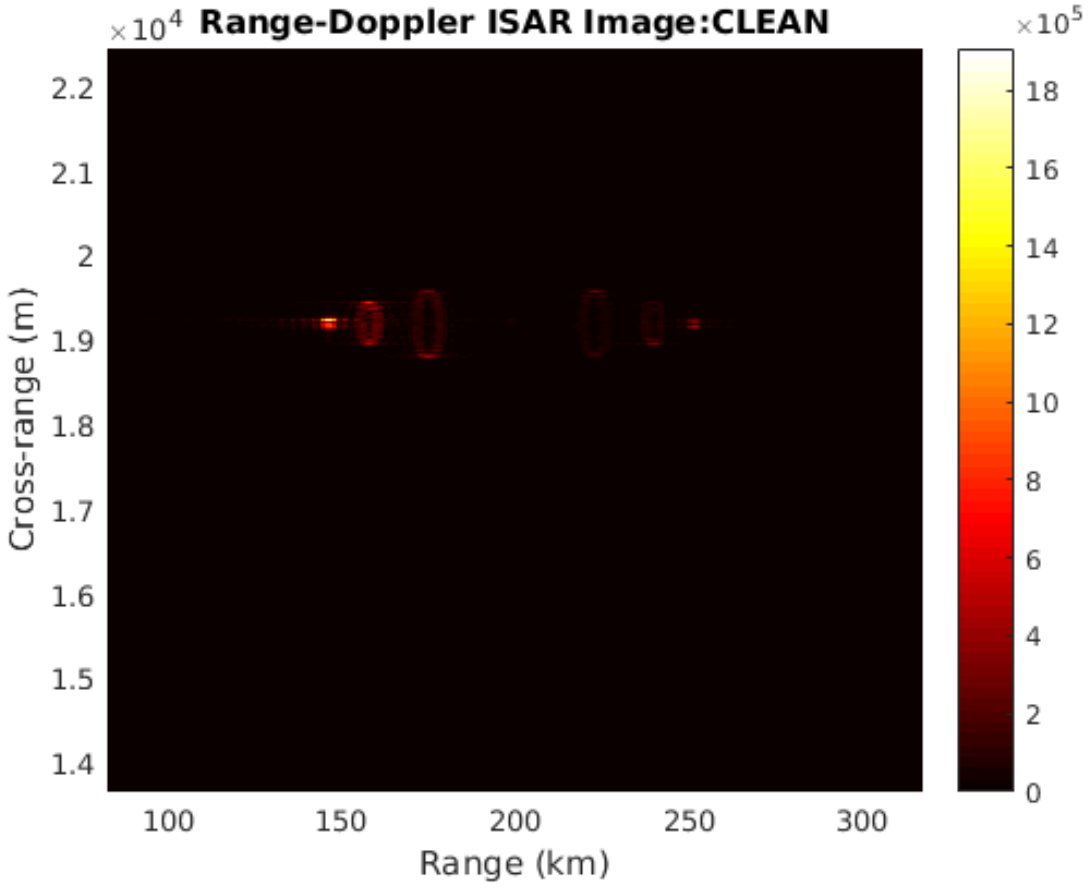

Figure 4.23: ISAR image for 5 representative debris objects showing range and cross-range after applying the CLEAN algorithm.

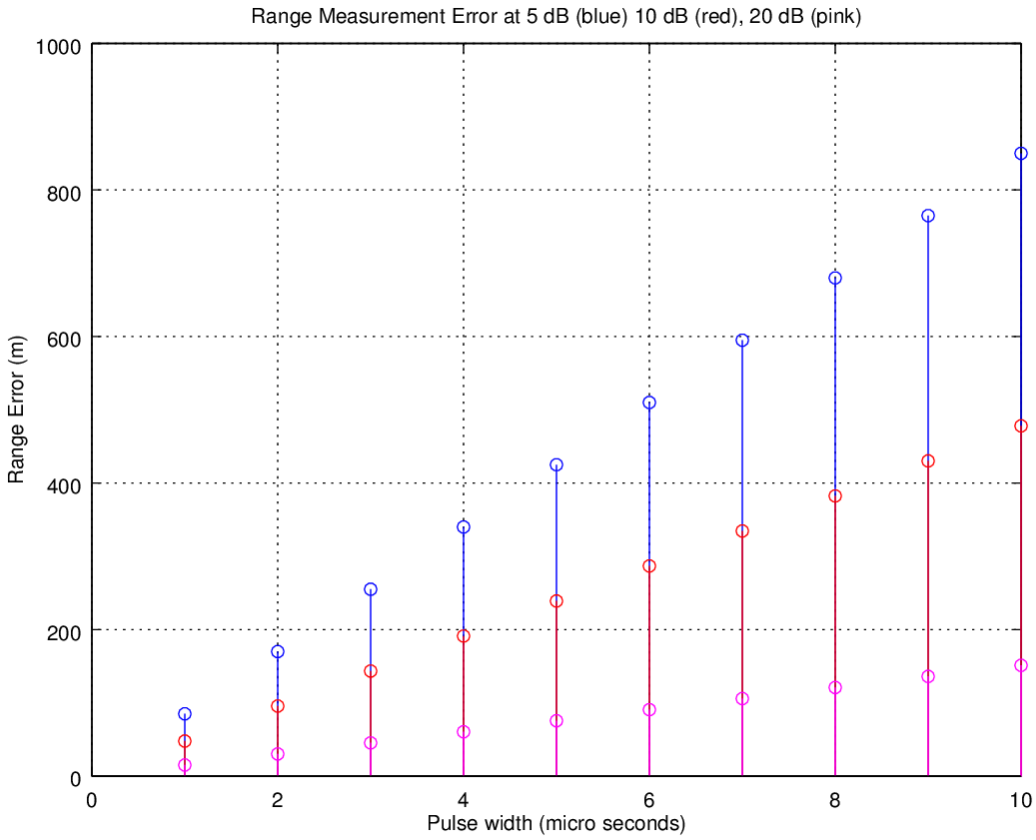

Figure 4.24: Range measurement errors in metres as a function of pulse width in μs for SNR of 5 dB, 10 dB and 20 dB. This result shows that even though the range measurement error decreases with increasing SNR, it also increases with increasing pulse width.

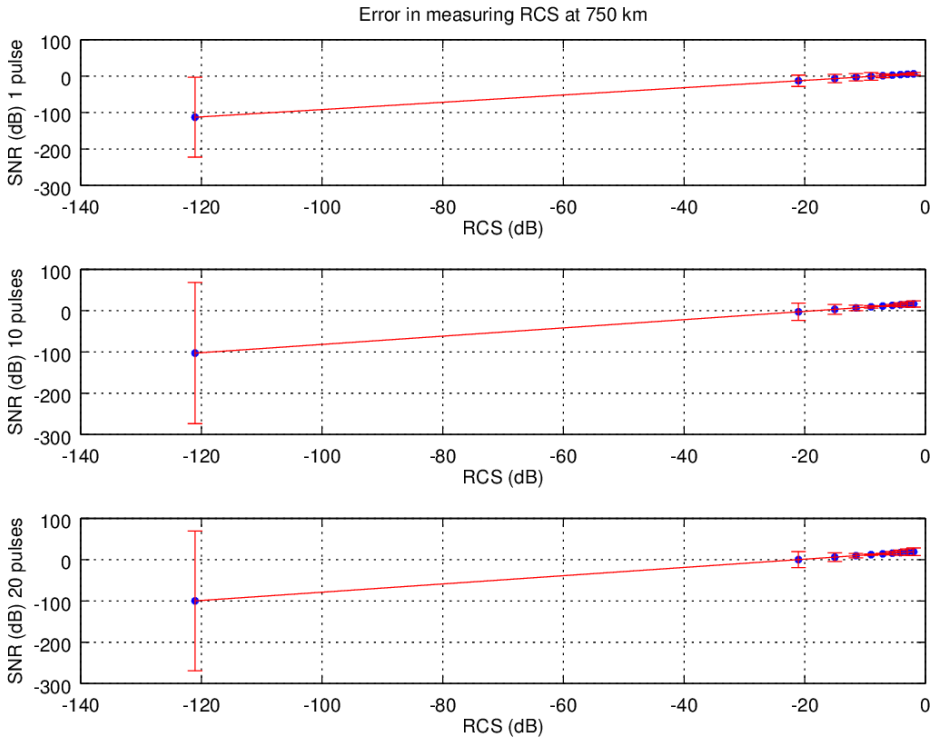

Figure 4.25: Error is measuring small debris radar cross section at 750 km for 1, 10 and 20 pulses.

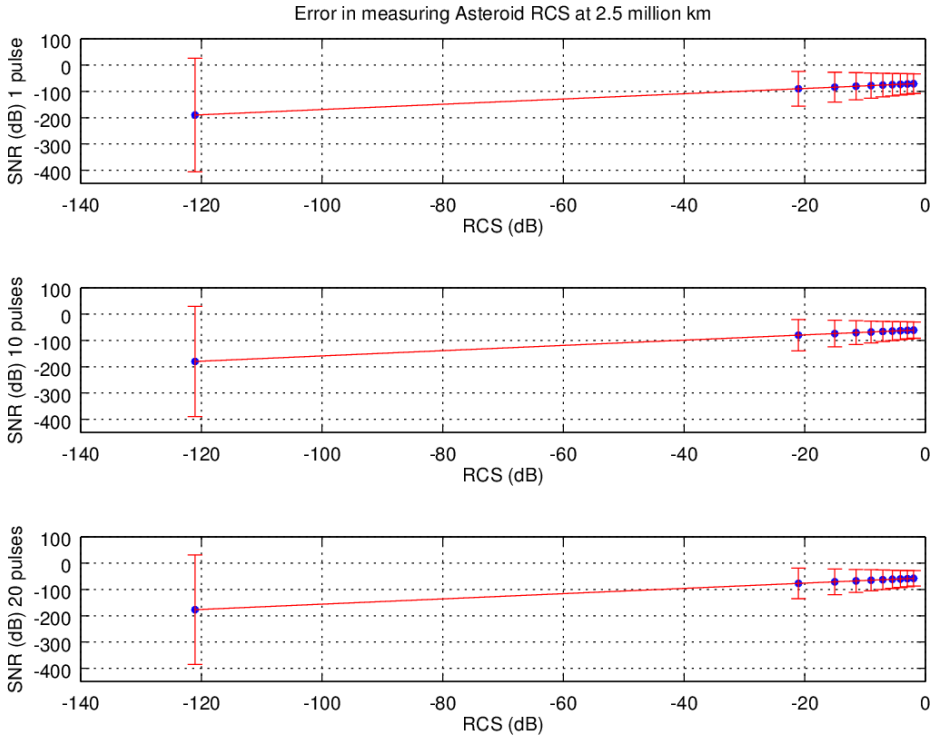

Figure 4.26: Error is measuring asteroid radar cross section at 2.5 million km for 1, 10 and 20 pulses.

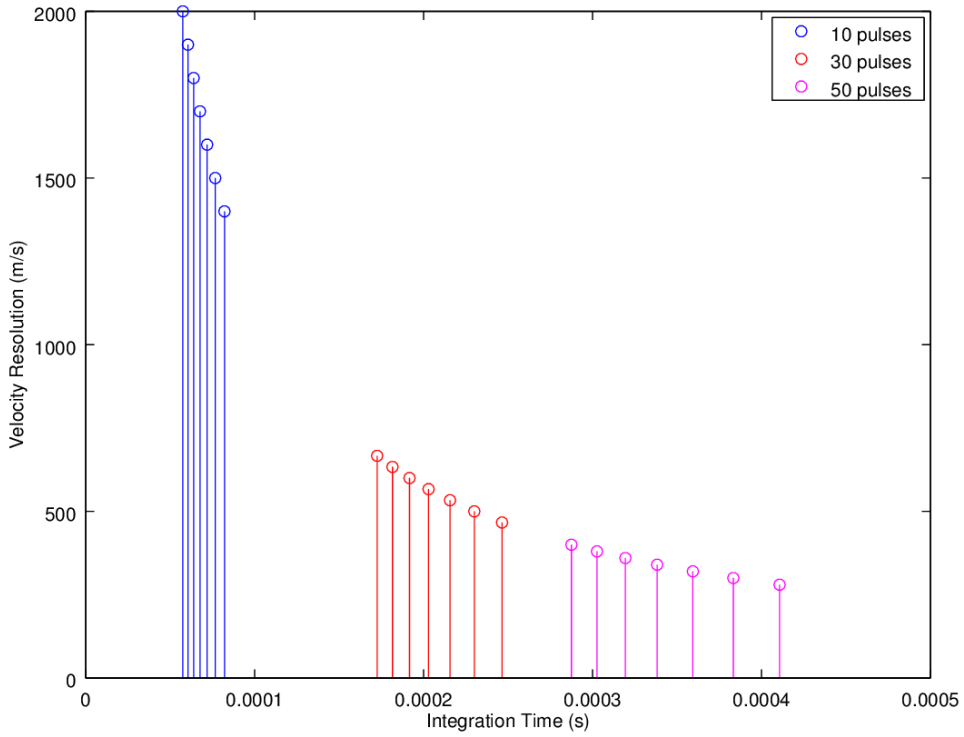

Figure 4.27: Target radial velocity resolution vs integration time for 10, 30 and 50 pulses.

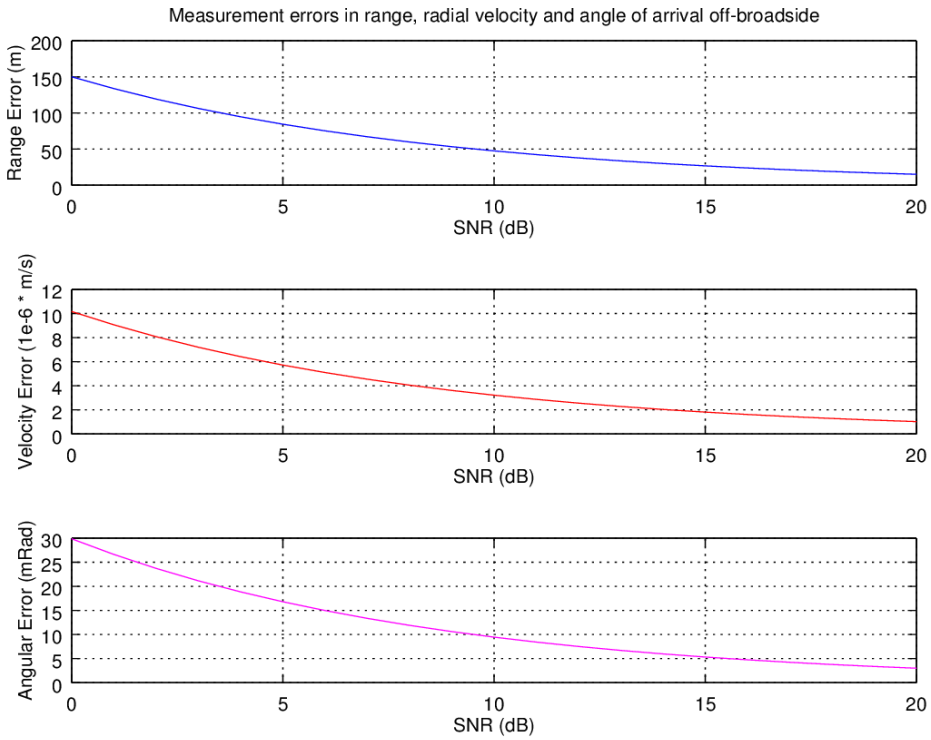

Figure 4.28: Range, Velocity and Angular measurement errors as a function of SNR. All the measurement error are seen to reduce with increasing SNR. The range measurement error is from 10 to 150 m, the velocity error is from 1 to 10 μm/s, the angular error is from 3 to 30 mili Radians.

Chapter 5: Concluding remarks

This chapter is a discussion on how the objectives set for this research have been accomplished. Points of emphasis are the suitability of the proposed radar specifications towards its ability to obtain useable data from near Earth objects, the choice of the most efficient signal processing technique and the accuracy with which data obtained would have. General concluding remarks are made and future work is proposed. The preliminary results obtained for a radar that uses KAT-7 radio telescope receivers are given in Appendix.

5.1 Summary of Findings

This research explained the need for an addition of a very sensitive radar in the current struggle to attain a "clean" and "safe" space environment and proposed the use of the MeerKAT radio telescope receivers in a radar system. This proposal was motivated by the problem of small space debris and PHA as illustrated in the literature review, and existing radars that have applied this similar technology to successfully detect, track and image objects in space. Further, there is need for instruments in the Southern hemisphere dedicated or contributing to NEO observations.

5.1.1 Review of Research Question 1

Based on available technology, parameters for a high power a nd cost effective transmitter were proposed and its suitability to the MeerKAT receivers discussed. A 10 kW transmitter was used in the proof of concept but calculations and simulations showed that the transmit power was low due to the low target RCS and large range values. Therefore the transmit power was increased to 2 MW using high power gallium-nitride (GaN) high electron mobility transistors (HEMT) so a to improve the matched filter SNR above 13 dB, the chosen lower threshold in this work. This threshold was chosen to exceed the minimum 10 dB for available instruments. In addition to high power, this transmitter has a high duty cycle (up to 20%) which is necessary in transmitting phase codes.

A region for the proposed location for the transmitter within the receiver line of sight was chosen while considering the radio frequency interference (RFI) levels for the SKA site as defined by the International Telecommunication Union (ITU). Due to the site suitability and existing infrastructure, we proposed the installation of a high power amplifier on a 10 m parabolic antenna at the Denel Overberg test range in Cape Town, South Africa.

5.1.2 Review of Research Question 2

Target parameters were obtained by deriving orbital elements from two line elements and then performing coordinate conversions from ECEF to the local ENU. Then the target location, diameter, range, relative velocity, acceleration, orbital period and inclination was obtained at a particular epoch. Before these parameters were used in theoretical analysis and simulations, a detailed description of the MeerKAT receiver was given.

A detailed description of the MeerKAT radio telescope receiver sub-systems gave insight into the relevant subsystems from the L-band receiver to digitiser, sampler, channeliser, correlator, beamformer and finally to data storage. A brief overview of the MIMO and SIMO techniques and used in radar were given,

clearly stating the different types, their benefits and drawbacks. It was clearly stated that the SIMO technique is of interest to this analysis because of its suitability, simplicity and less computational requirements compared to other MIMO subsets. The bistatic, multistatic and SIMO radar configurations were chosen to be evaluated in terms of detection, tracking and imaging as elaborated.

Basing on the MeerKAT digital back end and data rates, it was proposed that raw data be obtained directly after the digitiser and then down-sampled, or channelised data at lower data rates to be recorded. Even though both options for obtaining raw and pre-processed data are available, the only limitation is availability of storage space for the "heavy" raw data. Data size depends on the number of targets and receivers used and whether data is time or frequency domain. Raw time domain from a single 1712Msps, 10-bit, dual polarisation receiver, plus header is about 35Gbps or from a single channelised beamformer at 856MHz complex 8-bit, dual polarisation, plus header of about 29Gbps.

From theory, it was found that the maximum coherent SNR for the MeerKAT bistatic radar was higher that the non-coherent integration by 7 dB for the maximum number of pulses for geometries at maximum and minimum elevation angles. Therefore, in simulations, only coherent integration was considered and the simulation duration was limited to the CIT limitation (2.02 ms) for non-accelerating targets.

Using range shifting, range migration was compensated for in the FERS simulation of the chosen representative small debris and asteroids. From geometry, accelerating targets had the largest CIT leading to better Doppler resolution compared to non-accelerating targets 5.1. Comparison of theory with simulations showed minor deviations (only after 4 significant figures) in bistatic delay and aliased normalised Doppler frequency.

Deviation of theory from simulations as a result of simplifying assumptions in the simulator and rounding off in the signal processing algorithm, was seen. The results from theory and simulations matched up to 4 significant figures. This error was tested and confirmed by simulating different radars and target environments. It was considered minor since most of the values are recorder up

Table 5.1: Number of range bins before and after application of the range migration compensation algorithm, for the representative orbital debris and PHA.

	Fengyun 1C	Iridium 33	Cosmos 2251	2015 BN50g	2010 NY65	1998 SL36
$f_(Dn)$	-0.1108	-0.1072	-0.11200	0.3280	-0.4760	-0.2240
Bins before	2.5	2.7	2.6	69.4	45.4	52.9
Bins after	0	0	0	27.8	18.2	21.2
$f_s = 10$ MHz				13.9	9.1	10.6
$f_s = 5$ MHz				5	1.5	2

to 4 significant figures.

For asteroids, the quasi-monostatic set up, using phase codes, was not sufficient to detect objects with a positive SNR. More receivers needed to be used in order to obtain meaningful NEO detections. The range walk was worse for asteroids due to their high speed, and both the range shifting and Keystone transform were unable to completely remove the range migration. One of the solutions to this problem is severely under-sampling the asteroid data so as to increase the range bin size significantly.

It was only suitable to use the bistatic configuration for the MeerKAT radar using a high power transmitter and at maximum receiver azimuth and elevation angles. Coherent processing for accelerating targets gave the largest dwell time and hence the most coherent integration gain.

Coherent integration for non-accelerating targets and non-coherent integration did not give sufficient SNR increase for a probability of detection of at least 88 % and probability of false alarm of 1e-6 (see Table 5.2). It was necessary to increase the SNR further by using more than one receiver. However, the purpose of proof of concept was achieved by showing the suitability of the transmitter site and the radar geometry for small debris and PHAs monitoring.

5.1.3 Review of Research Question 3

According to simulations, the multistatic radar configuration was found to be the most effective compared to the bistatic and SIMO configurations due to its

Table 5.2: Matched filter SNR for Fengyun 1-C debris (R=885 km, v=7.41 km/s) for CPI of 2.02 ms for non accelerating debris and CPI of 121.2 ms for accelerating debris.

Configuration	SNR (dB)	SNR(CPI=2.01 ms)	SNR(CPI=121.2 ms)
Bistatic	-9.4	4.8	12.4
Multistatic	7.6	20.0	28.9
SIMO	7.6	20.0	28.9
Beamforming		22.6	31.0

suitability to the MeerKAT receivers, low computational requirements and lower data storage capacity. The SIMO configuration requires a matched filter at each receiver, whereas the centralised multistatic configuration gives the option of centrally processing data. However, the SIMO radar that uses multiple beams gave SNR higher than the multistatic radar by 2 dB due to beamforming.

The MeerKAT antennas were then divided into inner, middle and outer circular sub-arrays and evaluated together and separately. The three concentric circular sub-arrays which were used to implement multi-beam debris tracking with increased track time and a 3D coverage. A debris track was generated and in put into the radar simulator, post processing of the ideal data showed that the track was best reproduced using the inner sub-array compared to the middle and outer sub-arrays. The reason for this is the large number of antennas in the inner array (44) compared to 10 antennas in the middle and outer sub-arrays.

Debris imaging was simulated using inverse synthetic radar (ISAR) and LFM waveforms and making use of the high down range and cross range resolution that can be attained from stretch processing and DFT. The CLEAN deconvolution algorithm was implemented to improve the image resolution. The small debris were modelled as a larger debris cluster/cloud of diameter 1 m with 5 evenly distributed 10 cm from the origin.

5.2 Concluding Remarks

Based on the findings discussed above, and the range, velocity and angular radar measurement error analysis, and how these errors propagate to orbital period and inclination prediction and comparison of the MeerKAT radar performance to existing dedicated contributing space situational awareness assets such as TIRA, Haystack, HAX and FPS-85, the following conclusions were made:

The most cost effective and suitable transmitter for the MeerKAT 3D radar is a 10 m parabolic antenna to be installed at the Denel Overberg test range in Cape Town with the a Gallium Nitride HEMT amplifier to produce a peak power of 2 MW, capable of transmitting linear frequency modulated waveforms and phase codes in form of pulses, at varying pulse repetition frequencies and the waveforms transmitted should have the option of being orthogonal.

The bistatic configuration was only used as a proof of concept since the SNR obtained from it was too low (less than 13 dB) for sufficient detection or tracking for 152 pulses and 2.02 ms integration time. The nearest to optimal radar configuration and signal processing is the multistatic radar due to its suitability to the receive antennas digital back end, simplicity in the transmit waveform, increased dwell time, low computational requirements in signal processing and low data rates for storage. The SIMO radar requires orthogonal or quasi-orthogonal transmit waveforms and this increases the signal processing requirements on receive. The decentralised SIMO signal processing requires a matched filter on each receiver compared to the centralised multistatic configuration.

The use of the MeerKAT antennas in a radar will depend on available receivers at the time of the observation and data collecting, this requires flexibility in terms of which antennas can be used in the radar receiver. The multistatic configuration offers flexibility in choosing receivers and performing digital beamforming where necessary. The multistatic radar gives the option of post-proccessing data in a centralised or decentralised manner depending on the data size and suitability for a particular observation, whereas the SIMO radar only allows a decentralised

mode.

Finally, this work illustrated through simulations and theoretical analyses, the bistatic, multistatic and SIMO radar configurations for the MeerKAT 3D radar. By investigating parameters such as: SNR, detection probability, false alarm rate, transmit power, transmit waveform, range/Doppler resolution and track time, the hypothesis that such a radar system, once implemented will provide data that can be used to detect, track, image and classify NEOs and in the long run become a vital contributor to a constantly updated database, was clearly shown.

5.2.1 Future Work

Proposed future work includes: actual installation of the transmitter in the MeerKAT radio telescope receivers' field of view, addition of more transmitters in the Southern hemisphere, implementing a radar that uses the SKA antenna receivers, upon its completion, and adjusting the radar digital back end to include capabilities beyond the near Earth orbit, such as assisting in Mars expeditions.

Once the radar is constructed, preliminary tests will be done with a large orbiting object, such as the International Space Station, and results will be used to calibrate and verify the system's performance. Then a theoretical analysis of the visibility for debris and asteroids that will be predicted to pass within the radar's field of view will be done as preparation for an experiment. Once a time window has been identified, then observations will be scheduled and done, first for cataloged and then uncatalogued objects. It would be more advantageous if these observations were done in collaboration with other radars around the world so as to create a "time stamped" data set of the same object.

Appendix: An analysis using the KAT-7 receivers.

This Appendix gives an analysis of small space debris detection using the proposed 15 m transmit antenna located at Denel Overberg Test Range (33.9980273^{o}S 18.4570313^{o}E) in Cape Town, South Africa, and the KAT-7 radio telescope antenna receivers. The Karoo Array Telescope (KAT)-7 constitutes seven, 12 m, prime focus parabolic dish antennas. KAT-7 is located at 30.721^{o}S 21.411^{o}E, has antenna separations between the seven elements that range from 26 m to 185 m (as shown in Figure 5.1) and operates in the frequency range of 1200 MHz to 1950 MHz.

Table 5.3 shows the simulation parameters for the range and Doppler modes. Two object parameters were estimated to represent the lower and upper bounds of the debris sizes, average relative velocity and altitude, as shown in Table 5.4. Two different values of pulse repetition frequency (PRF) were used for each of the target simulations, a low PRF to obtain the required unambiguous range and a high PRF to avoid Doppler ambiguity. The number of integrated pulses is 5 for the range mode and 60 for the Doppler mode.

5.3 KAT-7 bistatic radar simulated results

The bandpass signal is transmitted in form of a chirp and the echo received and stored for range-Doppler processing. Free space propagation is assumed

Figure 5.1: KAT-7 radio telescope antennas in the Karoo region in Northern Cape, South Africa [57].

and antenna steering and multi-path effects have not been taken into account. The debris RCS is considered non-fluctuating and it is modelled as spherical. Hamming windowing was used to reduce the peak sidelobes. Figures 5.2 and 5.3 show the normalised amplitude (colour bar), bistatic range and Doppler outputs from the simulated data. Figure 5.4 shows the variation of SNR with detection range for the KAT-7 analysis.

5.4 Summary of the KAT-7 radar analysis

The simulated results show that objects with RCS in the range of 1.5 dBsm to 10.5 dBsm and altitude of 300 km and 800 km can be detected using a bistatic radar system that uses a 15 m transmitter in Cape Town and the KAT-7 receivers. Low PRF values are chosen for the range mode so as to maintain

Table 5.3: Simulated radar system parameters.

Parameter	**Value**
P_m	2 MW
f_0	1.2 GHz
λ	0.25 m
B	256 MHz
G_m	23 dBi
G_n	21 dBi
T_n	35 K
N	7
Waveform	Chirp
Range mode	
τ	200 μs
Target 1 PRF	180 Hz
Target 2 PRF	500 Hz
Doppler mode	
τ	5 μs
Target 1 PRF	10 kHz
Target 2 PRF	18 kHz

.

Table 5.4: Target parameters used in the simulation.

Parameter	**Target 1**	**Target 2**
σ	1.5 dBsm	10.5 dBsm
V_{rel}	1 km/s	2 km/s
R	300 km	800 km

a duty cycle of $\leq$10 %. The high PRF values chosen to be greater than the estimated bistatic Doppler frequency for each of the targets were chosen to avoid Doppler ambiguities due to high target speed.

Assuming a 60 % probability that each scan would detect a target, the overall probability of detection of the 1X7 bistatic radar system is 0.9984 and the probability of false alarm would be decreased by a factor of 7 (the number of

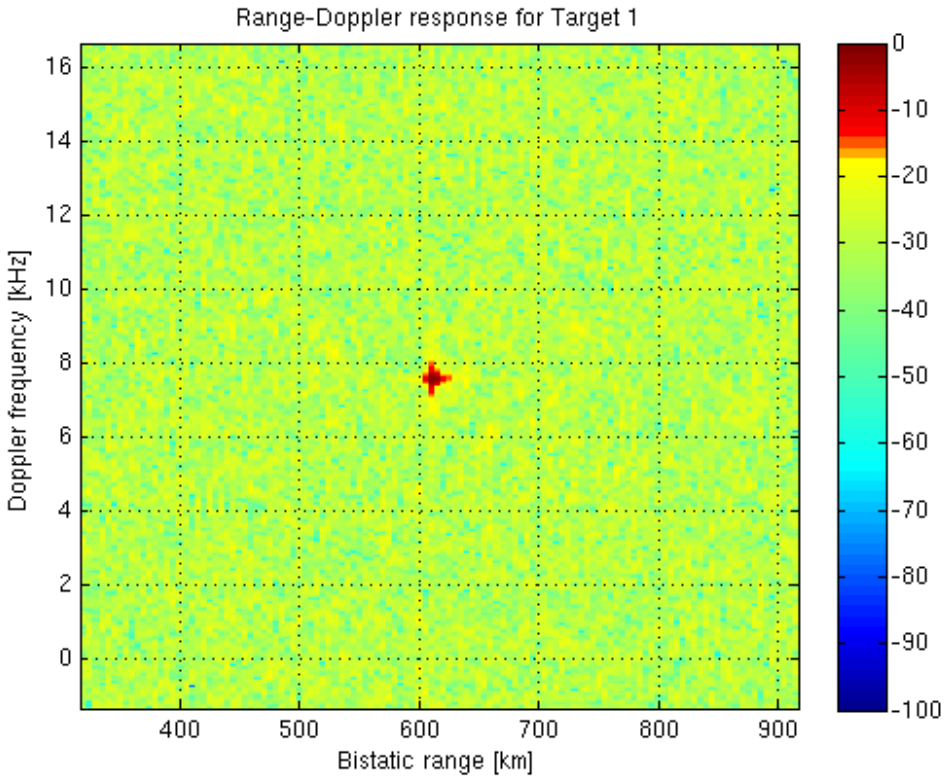

Figure 5.2: Simulated range-Doppler output with normalised amplitude for Target 1, Doppler frequency = 7.8 kHz, Bistatic range = 610 km, SNR $\approx$ 26 dB

receivers).

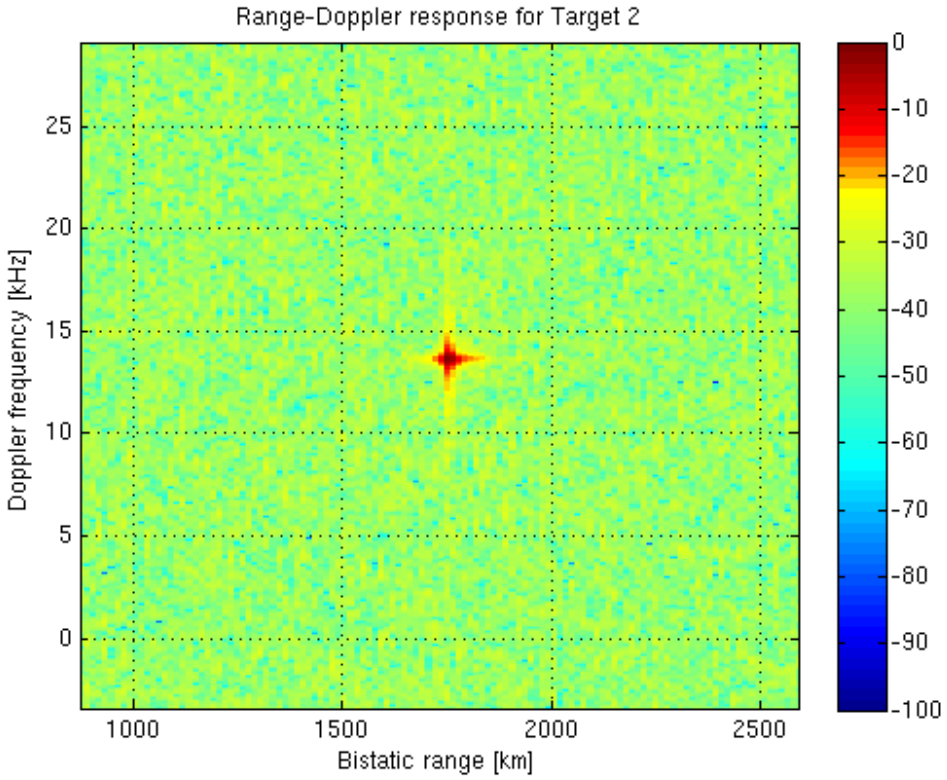

Figure 5.3: Simulated range-Doppler output with normalised amplitude for Target 2, Doppler frequency = 14.8 kHz, Bistatic range = 1675 km, SNR ≈ 35 dB

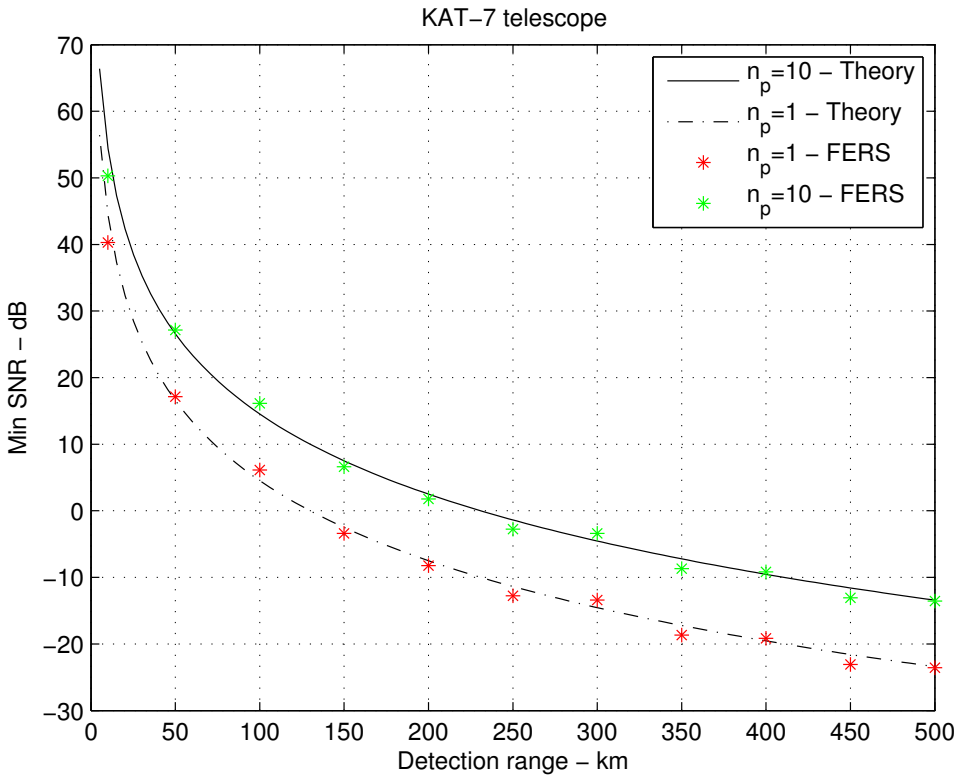

Figure 5.4: Comparison of simulated and theoretical SNR for 1 pulse and 10 pulses up to a maximum detection range of 500 km.

Bibliography

[1] D. Mehrholz, L. Leushacke, W. Flury, R. J. H. Klinkrad, and M. Landgraf, "Detecting, tracking and imaging space debris," *ESA bulletin 109*, Feb 2002. xii, 3, 28, 30, 31

[2] ESA, "European space agency, space situational awareness." `http://www.esa.int/Our_Activities/Operations/Space_Situational_Awareness`, Accessed: Jan, 2016. 1, 3

[3] GAF, "German arm forces, space situational awareness." `http://afcea.de/fileadmin/downloads/Mittags-foren/12.03.2010/Borst.pdf`, Accessed: Jan, 2016. 1

[4] SSA, "Space foundation, space situational awareness." `https://www.spacefoundation.org/programs/public-policy-and-government-affairs/introduction-space-activities/space-situational`, Accessed: Jan, 2016. 1

[5] J. Kennewell and B.-N. Vo, "An overview of space situational awareness," in *Information Fusion (FUSION), 2013 16th International Conference on*, pp. 1029–1036, July 2013. 1, 2

[6] I. Ritchie, "Eos space systems: Remote control southern hemisphere ssa observatory," 2013. 2

[7] O. Kalden and C. Bodemann, "Building space situational awareness capability," in *Recent Advances in Space Technologies (RAST), 2011 5th International Conference on*, pp. 650–654, June 2011. 2

[8] F. Daum, "Radar handbook, 3rd edition (m.i. skolnik, ed; 2008) [book review]," *IEEE Aerospace and Electronic Systems Magazine*, vol. 23, pp. 41–41, May 2008. 2, 16, 36, 39

[9] J. Ender, L. Leushacke, A. Brenner, and H. Wilden, "Radar techniques for space situational awareness," in *Radar Symposium (IRS), 2011 Proceedings International*, pp. 21–26, Sept 2011. 2, 35

[10] D. Vigilante, F. Feudo, S. Immediata, R. Petrucci, V. Simeone, A. Lanzillotti, and F. Mosconi, "On the use of long-range radars for space situational awareness: An experimental test," in *Radar Conference (RadarCon), 2015 IEEE*, pp. 1744–1749, May 2015. 2, 59

[11] L. A. M. Benner, "Goldstone radar observations planning: 2011 uw158, 1994 aw1, and 1999 jd6." `http://echo.jpl.nasa.govasteroids2011UW158/2011UW158_planning.html`. Accessed: 2015/05/30. 2

[12] M. Skolnik, "Fifty years of radar," *Proceedings of the IEEE*, vol. 73, pp. 182–197, Feb 1985. 2

[13] N. Levanon and E. Mozeson, eds., *Radar Signals*. John Wiley & Sons, 2004. 2

[14] U. Office, "United states government accountability office, development and oversight challenges in delivering improved space situational awareness capabilities," *Space Acquisitions*, August 2010. 3

[15] B. B. C. B. N. Paul Rincon, "Standing watch over a crowded space." `http://news.bbc.co.uk/2/hi/science/nature/7916582.stm`, Accessed: Jan, 2017. 4

[16] P. H. Krisko, "NASA's New Orbital Debris Engineering Model, ORDEM 2010," in *Making Safety Matter*, vol. 680 of *ESA Special Publication*, p. 50, Sept. 2010. 3

[17] S. Eugine and B. Michelle, "National aeronautics and space administration (NASA) orbital debris quarterly news, johnson space center (jsc)," Jan 2014. 3

[18] H. Klinkrad, "Esa's database and information system characterising objects in space," *Advances in Space Research*, vol. 11, pp. 43–52, 1991. 4

[19] U. Nations, "Technical report on space debris," Tech. Rep. 92-1-100813-1, United Nations Committee on the Peaceful uses of Outer Space, United Nations, New York, 1999, 1999. 4, 24

[20] C. R. Englert, J. T. Bays, K. D. Marr, C. M. Brown, A. C. Nicholas, and T. T. Finne, "Optical orbital debris spotter," *Acta Astronautica*, vol. 104, no. 1, pp. 99 – 105, 2014. 4

[21] D. J. Kessler and B. G. Cour-Palais, "Collision frequency of artificial satellites: The creation of a debris belt," *J. Geophys. Res.*, vol. 83, no. A6, pp. 2637 – 2646, 1978. 4, 59

[22] S. Eugine and B. Michelle, "National aeronautics and space administration (NASA) orbital debris quarterly news, johnson space center (jsc)," April 2015. 5

[23] S. Flegel, J. Gelhaus, and M. e. a. Mckel, "Maintenance of the esa master model: Final report," *European Space Agency*, June 2011. 5

[24] N. Aeronautics and S. A. N. O. D. Q. News, "Increase in iss debris avoidance maneuvers," April 2012. 6

[25] S. Eugene, "Nasa johnson space center ,the orbital debris program office, orbital debris modeling." `http://orbitaldebris.jsc.nasa.gov/model/modeling.html`, October 2012. 7, 8

[26] K. A. van der Hucht, "International astronomical union, near earth asteroids (neas): A chronology of milestones." `http://www.iau.org/public/themes/neo/nea/`, Oct 2013. Accessed: 2015/05/24. 7

[27] A. Chamberlin, "Nasa:near earth object program." http://neo.jpl.nasa.gov/stats/. Accessed: 2015/05/24. 7

[28] S. J. Ostro, "The role of groundbased radar in near-earth object hazard identification and mitigation. in hazards due to comets and asteroids (t. gehrels and m. s. matthews, eds.)," *Univ. of Arizona Press*, pp. 259–282, 1994. 8

[29] GAF, "Planetary science institute." https://www.psi.edu/epo/explorecraters/virtualtours.htm, Accessed: Jan, 2017. 8, 9

[30] D. J. Roddy and T. M. Hare, "Barringer meteorite crater, arizona (meteor crater)," *Astrogeology, U.S. Geological Survey, Flagstaff, AZ*, 1998. 8

[31] B. Line, "Asteroid impacts: 10 biggest known hits. national geographic news." http://news.nationalgeographic.com/news/2013/13/130214-biggest-asteroid-impacts-meteorites-space-2012da14/, Feb, 2013. 8

[32] T. E. O. S. (EOS), "Space surveilance." http://www.eos-aus.com/space/what-we-offer/space-surveillance, Accessed: Jan, 2016. 9

[33] C. L. . Stokely, J. L. Foster, E. G. J. Stansbery, J. R. Benbrook, and Q. Juarez, "Haystack and hax radar measurement of the orbital debris environment," Tech. Rep. JSC-62815, NASA Orbital debris Program Office, Nov 2006. 24, 26, 28, 29

[34] S. P. Naidu, L. A. M. Benner, M. Brozovic, J. D. Giorgini, J. S. Jao, M. W. Busch, P. A. Taylor, J. E. Richardson, E. G. Rivera-Valentin, L. A. Ford, F. D. Ghigo, and A. Kobelski, "Radar observations of near-Earth asteroid (436724) 2011 UW158 using the Arecibo, Goldstone, and Green Bank Telescopes," in *AAS/Division for Planetary Sciences Meeting Abstracts*, vol. 47 of *AAS/Division for Planetary Sciences Meeting Abstracts*, p. 204.08, Nov. 2015. 25

[35] S. Eugene, "Nasa johnson space center ,the orbital debris program office , orbital debris radar measurements." `http://orbitaldebris.jsc.nasa.gov/measure/radar.html`, August 2009. 26

[36] H. Klinkrad, ed., *Space Debris, models and risk analysis*. Springer, Praxis publishing, Chichester, UK, 2006. 29

[37] J. Wang, W. Jian, W. Zhen-Sen, and L. Yong-Jun, "Observation debris rcs with the tristatic radar," in *Antennas, Propagation EM Theory (ISAPE), 2012 10th International Symposium on*, pp. 853–856, Oct 2012. 29, 116

[38] M. J., "Eiscat space debris measurements at the svalbard radar in 2007." `http://www.sgo.fi/~jussi/spade/ipy/`, Accessed: Jan, 2017. 29

[39] M. Landgraf, R. Jehn, and W. Flury, "Comparison of EISCAT radar data on space debris with model predictions by the master model of ESA," *Advances in Space Research*, vol. 34, pp. 872–877, Jan. 2004. 30, 31, 32, 33

[40] F. Laghezza, F. Berizzi, A. Capria, E. Dalle Mese, G. Pupillo, S. Montebugnoli, E. Salerno, and M. Di Martino, "Italian bistatic radar system for surveillance of space debris in low earth orbit," in *Radar Conference, 2010 IEEE*, pp. 220–224, 2010. 32, 34

[41] A. Morselli, P. D. Lizia, G. Bianchi, C. Bortolotti, S. Montebugnoli, G. Naldi, F. Perini, G. Pupillo, M. Roma, M. Schiaffino, A. Mattana, E. Salerno, A. Magro, K. Z. Adami, R. Armellin, A. L. Sergiusti, W. Villadei, F. Dolce, M. Reali, and J. Paoli, "A new high sensitivity radar sensor for space debris detection and accurate orbit determination," in *Metrology for Aerospace (MetroAeroSpace), 2015 IEEE*, pp. 562–567, June 2015. 33

[42] H. Klinkrad and R. Jehn, "The space-debris environment of the earth," *ESA Journal*, vol. 16, pp. 1–11, 1992. 34

[43] T. Weil and M. Skolnik, eds., *Transmitters: Radar Hand Book Chapter 7*. McGraw-Hill, New York, 1970. 35

[44] R. S. Symons, ed., *Modern Microwaves Tubes For Radar*. Tri-Service VED Workshop, Arlington, VA, August 2001. 35

[45] P. D. Brown, J. A. Casey, J. M. Mulvaney, T. A. Hawkey, M. A. Kempkes, and M. P. J. Gaudreau, "Improvements in radar transmitter performance and reliability using high-voltage solid-state modulators and power supplies," in *Radar Conference, 2002. Proceedings of the IEEE*, pp. 113–120, 2002. 35

[46] M. Gaudreau, J. Casey, P. Brown, T. Hawkey, J. Mulvaney, and M. Kempkes, "High performance, solid-state high voltage radar modulators," in *2005 IEEE Pulsed Power Conference*, pp. 839–842, June 2005. 35

[47] G. A. S., ed., *Klystrons, Traveling Wave Tubes, Magnetrons, Cross-Field Amplifiers, and Gyrotrons*. Artech House, 1970. 36

[48] G. Caryotakis, "The klystron: A microwave source of surprising range and endurance," *American Physics Society: Division of Plasma Physics Conference, Pittsburg, PA. Stanford, CA: Stanford SLAC*, 1997. 36

[49] K. Tomiyasu, "Spurious outputs from high power microwave tubes and their control," in *PGMTT National Symposium Digest*, vol. 61, pp. 31–32, May 1961. 36

[50] A. Staprans, "High-power microwave tubes," in *Electron Devices Meeting, 1976 International*, vol. 22, pp. 245–248, 1976. 37

[51] "Communications and Power Industries." `http://www.cpii.com`, 2016. Accessed: 2016/09/05. 36

[52] "Communications and Power Industries, USA." `http://h6systems.com/)`, 2016. Accessed: 2016/09/05. 36

[53] "Radtech Engineering, USA." `http://www.radar-sales.com/PDFs/Radtec%20Company`, 2016. Accessed: 2016/09/05. 36

[54] "Reutech radar systems, South Africa." http://www.rrs.co.za/, 2016. Accessed: 2016/09/05. 36

[55] D. R. M. O'Donnell, "IEEE Aerospace and Electronic Systems Society, and IEEE New Hampshire Section." http://aess.cs.unh.edu/radar, 2016. Accessed: 2016/09/04. 38

[56] J. R. Manley, *A Scalable Packetised Radio Astronomy Imager*. PhD thesis, University of Cape Town, 2014. 40, 42, 45, 48

[57] "MeerKAT radio telescope gallery." http://www.ska.ac.za/gallery/meerkat/, 2016. Accessed: 2016/09/05. 41, 139

[58] K. e. Francois, "The meerkat digital back end," tech. rep., SKA, MeerKAT, 2014. 42, 44

[59] "CASPER:Streaming Protocol for Exchanging Astronomical Data (SPEAD) protocol." https://casper.berkeley.edu/wiki/SPEAD, 2016. Accessed: 2016/09/05. 44

[60] J. Li and P. Stoica, eds., *Radar Signals*. Wiley, New York, NY USA, 2009. 49, 50

[61] A. Hassanien and S. A. Vorobyov, "Phased-mimo radar: A tradeoff between phased-array and mimo radars," *IEEE Transactions on Signal Processing*, vol. 58, pp. 3137–3151, June 2010. 49

[62] J. Li and P. Stoica, "Mimo radar with colocated antennas," *IEEE Signal Processing Magazine*, vol. 24, pp. 106–114, Sept 2007. 49, 50

[63] V. S. Chernyak, "On the concept of mimo radar," in *2010 IEEE Radar Conference*, pp. 327–332, May 2010. 49

[64] D. W. Bliss and K. W. Forsythe, "Multiple-input multiple-output (mimo) radar and imaging: degrees of freedom and resolution," in *Signals, Systems and Computers, 2004. Conference Record of the Thirty-Seventh Asilomar Conference on*, vol. 1, pp. 54–59 Vol.1, Nov 2003. 49, 50

[65] K. W. Forsythe and D. W. Bliss, "Waveform correlation and optimization issues for mimo radar," in *Conference Record of the Thirty-Ninth Asilomar Conference onSignals, Systems and Computers, 2005.*, pp. 1306–1310, October 2005. 49

[66] A. A. Gorji, R. Tharmarasa, and T. Kirubarajan, "Widely-separated mimo vs. multistatic radar for target localization," in *2012 IEEE International Conference on Acoustics, Speech and Signal Processing (ICASSP)*, pp. 2461–2464, March 2012. 49

[67] V. Chernyak, *Fundamentals of Multisite Radar Systems: Multistatic Radars and Multistatic Radar Systems*. Taylor & Francis, 1998. 49, 91

[68] B. Friedlander, "On the relationship between mimo and simo radars," *IEEE Transactions on Signal Processing*, vol. 57, pp. 394–398, Jan 2009. 49, 51

[69] A. Haimovich, R. Blum, and L. Cimini, "Mimo radar with widely separated antennas," *Signal Processing Magazine, IEEE*, vol. 25, no. 1, pp. 116–129, 2008. 49

[70] A. Khabbazibasmenj, A. Hassanien, and S. A. Vorobyov, "Transmit beamspace design for direction finding in colocated mimo radar with arbitrary receive array," in *2011 IEEE International Conference on Acoustics, Speech and Signal Processing (ICASSP)*, pp. 2784–2787, May 2011. 49

[71] E. Fishler, A. Haimovich, R. Blum, R. Cimini, D. Chizhik, and R. Valenzuela, "Performance of mimo radar systems: advantages of angular diversity," in *Signals, Systems and Computers, 2004. Conference Record of the Thirty-Eighth Asilomar Conference on*, vol. 1, pp. 305–309, Nov 2004. 49, 50

[72] M. Y. Cao, S. A. Vorobyov, and X. Mao, "Elevation and azimuth estimation in arbitrary planar mono-static mimo radar via tensor decomposition," in *2016 IEEE Statistical Signal Processing Workshop (SSP)*, pp. 1–5, June 2016. 49

[73] D. J. Rabideau and P. Parker, "Ubiquitous mimo multifunction digital array radar," in *Signals, Systems and Computers, 2004. Conference Record of the Thirty-Seventh Asilomar Conference on*, vol. 1, pp. 1057–1064, Nov 2003. 49, 50

[74] T. Cheng, W. Liao, and Z. He, "Mimo radar dwell scheduling based on novel pulse interleaving technique," *Journal of Systems Engineering and Electronics*, vol. 24, pp. 234–241, April 2013. 50

[75] C. Y. Chen and P. P. Vaidyanathan, "A subspace method for mimo radar space-time adaptive processing," in *2007 IEEE International Conference on Acoustics, Speech and Signal Processing - ICASSP '07*, vol. 2, pp. II–925–II–928, April 2007. 50

[76] E. Fishler, A. Haimovich, R. Blum, D. Chizhik, L. Cimini, and R. Valenzuela, "Mimo radar: an idea whose time has come," in *Radar Conference, 2004. Proceedings of the IEEE*, pp. 71–78, April 2004. 50

[77] C. Duofang, C. Baixiao, and Q. Guodong, "Angle estimation using esprit in mimo radar," *Electronics Letters*, vol. 44, pp. 770–771, June 2008. 50

[78] I. Bekkerman and J. Tabrikian, "Target detection and localization using mimo radars and sonars," *IEEE Transactions on Signal Processing*, vol. 54, pp. 3873–3883, Oct 2006. 50

[79] F. Daum and J. Huang, "Mimo radar: Snake oil or good idea?," *IEEE Aerospace and Electronic Systems Magazine*, vol. 24, pp. 8–12, May 2009. 50

[80] E. Brookner, "Mimo radar demystified and where it makes sense to use," in *2014 International Radar Conference*, pp. 1–6, Oct 2014. 51

[81] E. Brookner, "Mimo radars and their conventional equivalents; an update," in *IET International Radar Conference 2015*, pp. 1–8, Oct 2015. 51

[82] E. Brookner, "Mimo radars and their conventional equivalents," in *2015 IEEE Radar Conference (RadarCon)*, pp. 0918–0924, May 2015. 51

[83] H. Commin and A. Manikas, "Virtual simo radar modelling in arrayed mimo radar," in *Sensor Signal Processing for Defence (SSPD 2012)*, pp. 1–6, Sept 2012. 51, 108

[84] M. Malanowski and K. Kulpa, "Analysis of integration gain in passive radar," in *Radar, 2008 International Conference on*, pp. 323–328, Sept 2008. 54

[85] "Google Maps Online." `https://www.mapcustomizer.com/`. Accessed: 2016/10/09. 54

[86] ITU, "International telecommunication union, ITU-R Handb ook on Radio Astronomy," tech. rep., ITU-R Radiocommunications Bureau, Geneva, Switzerland, 2003. 55

[87] J. J. Egli, "Radio propagation above 40 mc over irregular terrain," vol. 45, pp. 1383–1391, October 1957. 55

[88] H. Kayal, "A nano satellite constellation for detection of objects in earth orbit," in *Recent Advances in Space Technologies, 2009. RAST '09. 4th International Conference on*, pp. 95–99, June 2009. 59

[89] J. J. Sudano, "A transformation of unit vectors to simplify derivations between earth-centered and local north-east-and-up on an ellipsoid earth," in *Aerospace and Electronics Conference, 1995. NAECON 1995., Proceedings of the IEEE 1995 National*, vol. 2, pp. 745–747 vol.2, May 1995. 61

[90] M. Jackson, "The geometry of bistatic radar systems," *Communications, Radar and Signal Processing, IEE Proceedings F*, vol. 133, no. 7, pp. 604–612, 1986. 63, 64

[91] L. Liu and He, "A practical method for range migration compensation in chirp radar," *Progress In Electromagnetics Research*, vol. 7, pp. 15–28, 2009. 70

[92] M. A. Richards, ed., *Fundamentals of Radar Signal Processing, second edition*. McGraw-Hill, 2014. 73

[93] M. A. Richards, "The keystone transformation for correcting range migration in range-doppler processing," 2014. 73

[94] M. Brooker, *The design and implementation of a simulator for multistatic radar systems*. PhD thesis, University of Cape Town, 2008. 79

[95] K. Milne, "Principles and concepts of multistatic surveillance radars," in *Radar-77*, pp. 46–52, 1977. 91

[96] Y. Paichard and M. Inggs, "Multistatic passive coherent location radar systems," in *Radar Conference, 2009. EuRAD 2009. European*, pp. 45–48, Sept 2009. 92

[97] F. Gumiero, C. Nucciarone, V. Anastasio, P. Lombardo, and F. Colone, "Multistatic passive radar geometry optimization for target 3D positioning accuracy," in *Radar Conference (EuRAD), 2010 European*, pp. 467–470, 2010. 92

[98] V. Anastasio, F. Colone, and P. Lombardo, "A procedure for effective receiver positioning in multistatic passive radar," in *Radar Conference, 2009. EuRAD 2009. European*, pp. 493–496, 2009. 93

[99] L. Constancias, M. Cattenoz, P. Brouard, and A. Brun, "Coherent collocated mimo radar demonstration for air defence applications," in *Radar Conference (RADAR), 2013 IEEE*, pp. 1–6, April 2013. 104

[100] X.-R. Li, Z. Zhang, W.-X. Mao, X.-M. Wang, and J. Lu, "A derivation of colocated mimo radar equation," in *Computational Problem-Solving (ICCP), 2011 International Conference on*, pp. 674–677, Oct 2011. 105

[101] C. W. Ning Tai and N. Yuan, "A design of coherent moving target simulator for inverse synthetic aperture radar," *Electromagnetic Research Symposium (PIERS), Shanghai, China*, pp. 2221–2225, August 2016. 111

[102] Hongya, "Isar imaging with lfm waveforms," in *Synthetic Aperture Radar, 2007. APSAR 2007. 1st Asian and Pacific Conference on*, pp. 729–734, Nov 2007. 112, 117

[103] G. W. Mengdao Xing, Qi Wang and Z. Bao, "A matched-filter-bank-based 3-d imaging algorithm for rapidly spinning targets," *IEEE Transactions on Geoscience and Remote Sensing*, vol. 47, pp. 2106–2113, July 2009. 116

[104] T. L. Foreman, "Application of the clean detector to low signal to noise ratio targets," tech. rep. 117

[105] K. Kulpa, "The clean type algorithms for radar signal processing," *MRRS-2008 Symposium Proceedings. Kiev, Ukraine*, vol. 6, pp. 152–157, September 2008. 118

[106] K. Kulpa, "Adaptive clean algorithm for high resolution inverse synthetic aperture radar (isar) imaging for vehicular application," *9th International Radar Symposium India, (IRSI - 13)*, pp. 1–5, December 2013. 118